Cold atom production via photodissociation of small molecules

William G Doherty
Jesus College
University of Oxford

A thesis submitted for the degree of
Doctor of Philosophy
Trinity Term, 2012

Acknowledgements

Over the course of my DPhil, there have been many people who have had a great influence on the course of my course, and as such, there are plenty of people deserving of thanks.

First and foremost, I would like to thank Professor Tim Softley for allowing me to spend nearly 5 years in his lab, both as a Master's student, and a postgraduate. I have had a fantastic time, and have certainly learnt an enormous amount under his supervision. He has always taken the care to make his research group feel like an extended family, and I shall very much miss working there.

I would also like to thank Dr Eckart Wrede and Dr David Carty from the University of Durham for giving me the opportunity to conduct part of my research in their laboratories. The experience I gained working alongside them has been a major factor in this work being completed.

I am also grateful for all the help and support offered to me through the years by all of the members of the Softley Group. Special mention much go to Dr Martin Bell and Dr Chris Rennick, neither of whom this work would have been possible without. Martin provided me with a sense of purpose during the early years of my DPhil, as well as being a noble adversary for pun based games. Chris has to be credited with giving me the confidence to fearlessly dive headfirst into the magnetic trapping experiments, in addition to being an amusing lab companion.

Finally, I would like to thank my friends for supporting me during my time in Oxford, as well as my family, who have propelled me to this point. Most of all, I would like to thank Kat, who has been my source of strength throughout.

Cold atom production via the photodissociation of small molecules

William G. Doherty, Jesus College

A thesis submitted in partial fulfilment of the requirements
for the degree of Doctor of Philosophy of the University of Oxford

Trinity Term, 2012

Abstract

This thesis describes the development of a relatively novel technique for the generation and subsequent trapping of cold species. Molecules in a pulsed supersonic expansion are photolysed, such that the centre-of-mass velocity vector of one of the fragments is equal in magnitude but opposed in orientation to the lab-frame velocity of the precursor molecule. This technique, known as 'Photostop', leaves a fraction of the fragments with a narrow velocity distribution, centered around zero velocity in the lab-frame. They can be shown to have zero velocity by changing the time between photodissociation and ionisation; fragments with a high kinetic energy will leave the ionisation volume prior to interrogation. The underlying velocity distribution is uncovered by using the velocity-map imaging technique, and the temperature of the fragments can be determined.

The method was originally optimised for the molecular case. Cold NO has been produced from the dissociation of NO_2 molecules, and a single rotational state has been shown to remain in the ionisation volume 10 μs after dissociation, implying a sample temperature of 1.17 K. Using the optimised experimental conditions derived from the velocity cancellation of NO, the atomic case is demonstrated for the dissociation of Br_2 to give zero-velocity Br fragments. The Br atoms are seen for delay times in excess of 100 μs, showing the greater applicability of the method to the atomic case. The temperature of the residual atoms is shown to be in the milliKelvin regime, as determined through detailed Monte Carlo simulation of the motion of the stopped atoms. The possibility of trapping the ultracold Br atoms in a magnetic field is explored, and a quadrupolar trap created between two permanent bar magnets is demonstrated to confine the atoms spatially, within the ion extraction optics, for delays in excess of 1 ms.

The Photostop technique is intended to be a stepping stone on the way to widening the number of chemical species available for study in the ultracold regime. The possibility of improvements to the experiment is considered, in order to increase the efficiency of the experiment such that the number density becomes high enough to be viable as a source of atoms for use in cold chemical reactive studies. The possibility of extending the method so as to be used as a tunable velocity source of atoms is also discussed.

Contents

1 Introduction **1**
- 1.1 Cold matter . . . 2
- 1.2 Cold chemistry . . . 3
- 1.3 Current methods of cold matter creation . . . 5
  - 1.3.1 Atomic cooling . . . 7
  - 1.3.2 Molecular cooling . . . 11
- 1.4 Trapping cold species . . . 17
- 1.5 Thesis outline . . . 19

2 Photostop theory **26**
- 2.1 Photodissociation . . . 27
- 2.2 The Photostop technique . . . 28
  - 2.2.1 The molecular beam . . . 29
  - 2.2.2 Energy distribution of fragments . . . 33
  - 2.2.3 Angular distribution of fragments . . . 36
- 2.3 Verification of the Photostop method with NO . . . 37
- 2.4 The Photostop experiment . . . 39
  - 2.4.1 Dissociation of NO_2 . . . 39
  - 2.4.2 Photofragment ion imaging . . . 41
  - 2.4.3 NO_2 Experiment . . . 47
  - 2.4.4 Velocity-map image calibration . . . 49
  - 2.4.5 Characterisation of the molecular beam . . . 50
  - 2.4.6 Finding the zero-velocity point . . . 53
  - 2.4.7 Finding the point of velocity cancellation . . . 55
  - 2.4.8 Understanding the action spectra . . . 57
  - 2.4.9 Understanding the rotational distribution . . . 58
- 2.5 Experimental results . . . 61
  - 2.5.1 NO signal . . . 61
  - 2.5.2 Results . . . 63
- 2.6 Identifying species suitable for velocity cancellation . . . 65
- 2.7 Outlook . . . 66

3 Production of cold bromine atoms **71**
- 3.1 Molecular Br_2 . . . 72
  - 3.1.1 Alternative channels . . . 74
  - 3.1.2 Isotope abundance . . . 75
- 3.2 Experimental set-up . . . 76

3.2.1 Determination of the dissociation wavelength . . . 77
3.2.2 Bromine calibration . . . 78
3.2.3 Optimization of the zero-velocity signal . . . 81
3.3 Results . . . 87
3.3.1 Analysis of the images . . . 90
3.3.2 Theoretical analysis of the data . . . 91
3.3.3 Density . . . 96
3.4 Experimental issues . . . 97
3.5 Appraisal of the atomic and molecular cases . . . 97
3.6 Confirmation of the results and optimisation . . . 98
3.6.1 Optimisation . . . 99
3.6.2 Results . . . 105
3.7 Conclusions . . . 109

4 Design of the magnetic trap 112
4.1 Introduction . . . 112
4.1.1 Bromine magnetic moment . . . 112
4.2 Trap design . . . 114
4.2.1 Trapping geometries . . . 114
4.3 Extraction optics . . . 119
4.3.1 Ion detection from within the trap . . . 127
4.3.2 Trap losses . . . 128
4.4 Prospects . . . 132

5 Magnetic trapping of bromine atoms 136
5.1 Magnetic trap implementation . . . 136
5.2 Ion detection . . . 140
5.2.1 Time-of-flight detection . . . 141
5.3 Experimental results for Br atom trapping . . . 144
5.3.1 Decay profiles . . . 153
5.3.2 Molecular beam collisions . . . 160
5.4 Trapping prospects . . . 163

6 Conclusions 165
6.1 Further work . . . 166
6.1.1 The extension of the Photostop method . . . 166
6.1.2 Mechanical chopper . . . 166
6.1.3 New trap design . . . 167
6.1.4 Prealignment of the molecules . . . 168
6.1.5 Magnetic guide . . . 168
6.1.6 Collision theory . . . 171
6.2 Outlook . . . 171

A Matlab code for Photostop simulations 173

Chapter 1

Introduction

The coldest natural temperature ever recorded on Earth was 184 K at the Vostok Station in Antarctica in 1983. Although this seems incredibly cold, the mean velocity of molecules in the air at this temperature is still 476 ms^{-1} ($v_{mean} = \sqrt{\frac{8k_BT}{\pi m}}$, calculated for N_2). For the coldest natural temperatures, we have to search the cosmos. The cosmic microwave background radiation fills the known universe, meaning that the temperature of deep space is 2.73 K [1]. Only in the laboratory can the subKelvin regime be reached, and it is this temperature regime that we, as scientists, wish to probe.

The field of cold chemistry is relatively new and vibrant. The techniques used in the creation of cold species are highly specialised, and are often only applicable to a few species of limited chemical interest. However, the novel properties of cold matter could feasibly throw light upon a great many chemical and physical processes, such as the effects of quantum mechanical processes, e.g. tunnelling, on the rates of chemical reactions. This thesis aims to explore the prospects for developing novel techniques for cold atom generation.

1.1 Cold matter

The field of cold matter is still youthful, and the full range of applications of cold species is unclear. Trapping ultracold gases in optical lattices may be of great use in the simulation of various problems in many-body physics [2], or may even lead to advances in quantum information processing [3]. The atomic clock [4], through measuring precisely the electronic transition frequency of various species, has allowed the second to be defined to an accuracy of within one part in 10^{10}, a precision that has been only become possible through cooling of atoms down to the ultracold regime to allow for longer probing times and reduced collision rates.

What is clear is that performing experiments at temperatures close to absolute zero could cast a lot of light upon interesting new areas of physics and chemistry. Ultracold species have been used to create a new phase of matter: the Bose-Einstein Condensate (BEC) [5]. When weakly-interacting bosons are reduced to a low enough temperature near absolute-zero, and are contained in some form of external potential, a high percentage of the bosons will exist in the ground quantum state, and if the de Broglie wavelength, which is inversely proportional to T ($\lambda = h/p$) is greater than the spacing between the bosons, then Bose-Einstein condensation can occur. Despite being postulated by Bose and Einstein in the 1920's, it was not until the 1990's that the BEC was experimentally realised [6, 7], which has led to a much increased interest in the field of ultracold atoms and molecules, and the chemistry that occurs at such low temperatures. Translational cooling of atoms and molecules provides several benefits to the fields of physics and chemistry. For instance, the spectroscopic resolution can be increased by several orders of magnitude, as the effects of Doppler broadening are decreased [8], and the reduction in velocities mean that, the species being probed remains in the measurement apparatus for longer, thus reducing transit-time broadening. In the quest to measure tiny constants, such as the electric dipole moment of the electron, improved resolution is critical [9].

1.2 Cold chemistry

By cooling atoms and molecules, we can expect to see the enhancement of quantum phenomena which are invisible at higher temperatures. At sufficiently low temperatures, i.e. in the sub-Kelvin regime, the de Broglie wavelength can become comparable with, or greater than, the atomic radius, and we could imagine that collisions between ultracold species would occur in a very non-classical manner. Indeed, for collisions at low kinetic energy, the partners will appear to act as quasi-bound species, and the dynamics can provide us with valuable insight into the long range potential surfaces [10]. If we consider collision dynamics from a classical point of view, the angular momentum for the reactive process can be written as:

$$|l| = \mu v_{rel} b, \tag{1.1}$$

where μ is the reduced mass of the colliding particles, v is their relative velocity and b is the separation at closest approach [11]. This angular momentum is proportional to the relative velocity, and thus, at sub-Kelvin temperatures, the angular momentum will be limited to the lowest few quantum states. The investigation of low temperature collisions opens up the possibility of controlling the outcome of an experiment: external magnetic and electric fields are able to greatly perturb the dynamics of a collision event [12].

Reactive collisions are of great interest, especially at low temperatures. The reaction between $HBr + K$ has been observed with slow beams [13], which demonstrates that the chemistry can occur with cold species and produce cold products. Reactions with low activation barriers are intriguing from a quantum perspective [14]; low reactant energies mean that tunnelling through a barrier may become a dominant process in the reaction itself. Near-barrierless reactions will generally occur between species which are electronically excited or are otherwise highly reactive, such as in a radical recombination reaction [15] or reactions involving ionic species [16–19].

Insertion reactions have been witnessed with dimers of the alkali metals [20].

To gain some measure of control over species at the atomic and subatomic levels, we need to operate with forces appropriate to the scale. The famous Stern-Gerlach experiment [21] showed that an inhomogeneous magnetic field will perturb the motion of silver atoms, splitting the trajectories into two components, one deflected up, and one down. The magnetic field imparts a torque on the magnetic dipole of the silver atom, as if it were a classically spinning paticle precessing in the field. The fact that there were two components, rather than a continuous spectrum, gave the world the first insight into the existence of the spin angular momentum quantum number. The experiment led to the important discovery of the spin of the electron, which would be an essential part of Dirac's formulation of relativistic quantum mechanics [22].

It was noted in some of the earliest experiments within the framework of quantum theory, that lines in atomic emission spectra could be split under the influence of external magnetic and electric fields. Emission from the Lyman-α transition in hydrogen was noted to split under the presence of a magnetic field, as shown in figure 1.1. Upon application of a field, some energy levels are raised, and some are lowered. This phenomenon gives rise to the concept of high- and low-field seeking states of an atom; i.e. that an atom's potential energy can increase on moving toward or away from a region of high-field. High-field seekers will gravitate towards regions of high-field and vice-versa. It is from such concepts that the idea of controlling the motion of an atom by application of electromagnetic fields arises [23, 24].

Controlling an atom's motion is not the only prospective use of electromagnetic fields. The relative shifting of an unbound pair of atoms and the bound state of a molecule can bring novel bound states into existence [25]. Such novel bound states have been used as a route to the creation of ultracold molecules from ultracold atomic samples (see section 1.3.2).

In general, there have been two real barriers to the observation of cold chemistry:

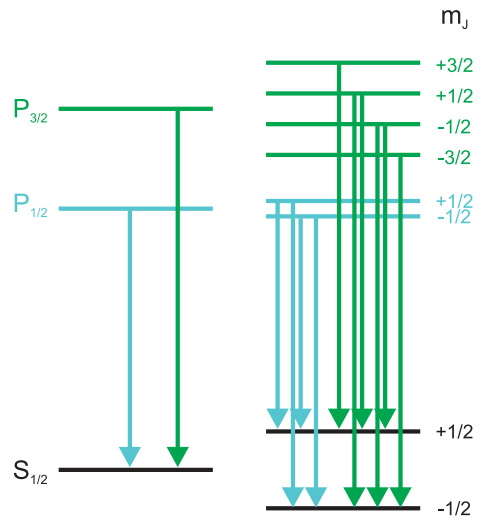

Figure 1.1: The effect of a magnetic field upon the first few energy levels of the hydrogen atom. The Zeeman splitting of the states leads to new transitions appearing in the emission spectrum, as seen on the right hand side. Note that the spin-orbit splitting of the P state occurs even in the absence of the magnetic field.

the limited range of species which are available to the experimentalist, thus limiting the number of possible experiments of interest, and the low number densities of the reactant species created from methods to generate the cold species initially. There has therefore been a large amount of investigation into novel methods of generating different and dense samples of cold atoms and molecules.

1.3 Current methods of cold matter creation

The major barrier to the investigation of cold matter is the creation and subsequent confinement of such species in sufficient densities, so as to be able to use them in an experimentally interesting manner. The experimentalist must somehow reduce the temperature of a sample down from ambient to ultracold temperatures, which requires the disposal of the undesirable energy. This section will discuss the possible methods of energy removal which are available at present.

There are various routes to the creation of cold atoms or molecules (see figure 1.2), and these can be described in terms of broad conceptions.

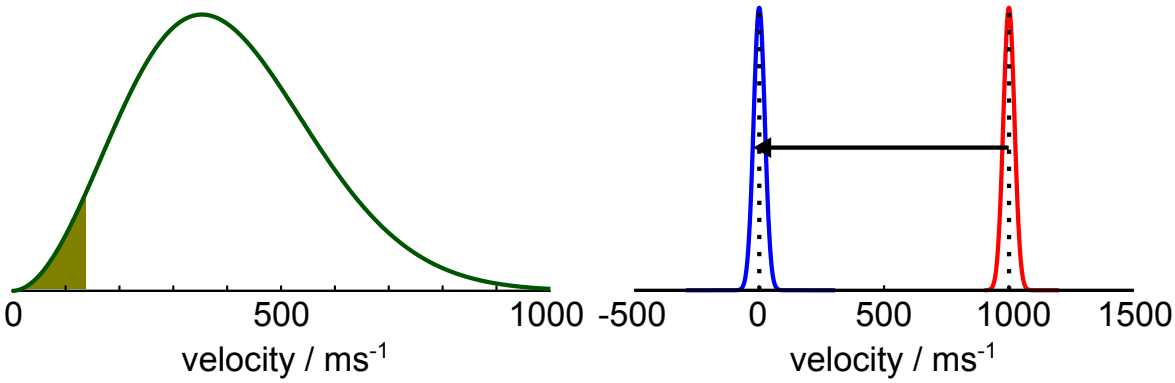

Figure 1.2: A diagram showing the two general routes to form cold atoms or molecules. The low velocity portion of the Maxwell-Boltzmann velocity distribution can be selected (left, highlighted region), or the velocity distribution can be pre-cooled, red, and then re-centered around zero, blue (right).

Velocity selection

The Maxwell-Boltzmann distribution describes the statistical distribution of velocities for a thermal sample. At ambient temperatures, the distribution spans a wide range of velocities. There is a small fraction of this distribution which has a kinetic energy of almost zero, as seen in the left-hand panel of figure 1.2. Some methods of generating kinetically cool samples attempt to extract this subset of the distribution, leaving a slow-moving (and therefore cold) sample. The quadrupole velocity-selector (see section 1.3.2) is an example of such an approach.

Notably, such techniques only affect the translational temperature of the species; there is no way to cool a sample internally using such a method. However, a major advantage for chemical reaction studies, is that the molecules are typically produced with a continuous flux, unlike most of the other techniques, which operate under pulsed conditions. As a result, this makes chemical reactions at low temperatures more easily studied, since there is a higher probability of collisions occurring [26].

Direct cooling

The alternative to velocity selection is to forcefully reduce the temperature of a thermal sample. This requires an input from an external factor to remove the unwanted energy. This is conceptually a much less passive process than mere velocity

selection.

The external factor can take many forms; the critical point is that the energy is removed from the species of interest. The factors can be as diverse as interactions with an electric or magnetic field [27], the application of a restorative force from a light source [28], or even collisions with an already cold species [29].

Notably, the different mechanisms work with differing degrees of success for different species. The success of the cooling is dependent upon the properties of the species that is cooled.

It should be mentioned here that I have broadly described this category as cooling, based on the mechanism of creating cold matter. However, real cooling requires an increase in the phase-space density. This is a combined measure of the temperature and density of the sample. For a species with a de Broglie wavelength ($\Lambda = \sqrt{\frac{2\pi\hbar^2}{mk_{BT}}}$), the phase-space density can be written as:

$$D = n\Lambda^3, \tag{1.2}$$

where n is the number density [30]. For a 'true' cooling process, such as buffer-gas cooling [29], the phase-space density increases over the course of the experiment. For an experiment which is more of a 'slowing' process, such as atomic deceleration [31], the cooling tends to come at the expense of the number density, leading to a relatively constant phase-space density.

1.3.1 Atomic cooling

Unsurprisingly, the easiest place to begin when trying to generate a cold gaseous sample is with the simplest species. Atomic species were the first to be reduced to cold and ultracold temperatures, since they are a lot more straightforward to cool.

Doppler cooling

In modern experiments with alkali atoms, the method of Doppler Cooling [32] has become predominant, whereby the atomic species absorbs and subsequently emits photons from laser radiation; typically 6 lasers are used, 2 counter-propagating along each of the major cartesian axes, to produce an overall slowing effect. Atoms moving towards a red-detuned laser beam will preferentially absorb photons from that direction, as they are Doppler-shifted into resonance, leading to a slowing through momentum conservation. The isotropic emission of photons will mean that, on average, an atom will gain a restorative momentum kick opposing its motion. This region is generally in the centre of a pair of coils in an anti-Helmholtz configuration to produce a magnetic field providing a potential barrier to low energy atoms from escaping – known as a magneto-optical trap (MOT) [28]. This technique can be extended to create ultracold plasmas [33], Rydberg gases [34], and has even been demonstrated in a weightless environment [35], with the aim of investigating the effect of microgravity upon ultracold gases.

The necessity for photon emission means that for successful cooling cycles, the atom must have an excited state with a short lifetime, in order to be able to rapidly undergo enough absorption-emission cycles to cool. Additionally, the species in question must have a closed cycle of absorption and emission, or the atoms will be lost to an inaccessible state. This requirement can be somewhat circumvented by the inclusion of additional lasers tuned to the transitions to states in the cooling cycle [18], which could be achieved by using a broadband laser cooling system [36].

An extension of laser cooling has also been demonstrated; cavity-assisted Doppler cooling [37, 38]. The atoms are laser cooled inside a high-finesse optical cavity. Certain radiative modes of the atom are enhanced inside the cavity, and as a result the atoms can preferentially scatter photons into a cavity mode. It is the recoil from the collision with the photon in this case, rather than the momentum imparted to an emitted photon, which is the mechanism of slowing in this experiment.

There are many atomic systems for which the cooling cycle has yet to be achieved successfully. For instance, in the case of the halogen atoms, there is potentially such a cooling cycle, but the photon energies required are in the vacuum ultra-violet spectral region, which is difficult to generate at sufficient intensities and with sufficient spectroscopic resolution, with photons required at 63436, 74226 and 104731 cm^{-1} for F, Cl and Br respectively.

Buffer gas cooling

The most intuitive technique for cooling is buffer-gas cooling [29], which uses elastic collisions with cold (around 4 K) helium atoms to disperse the energy of the sample. Helium is a possible buffer gas in this experiment as it still maintains a high enough vapour pressure at such temperatures, so as to be able to collide and remove the excess energy of the sample to be cooled. The residual atoms can then be trapped and evaporatively cooled to remove the most energetic, so as to reduce the sample temperature further. Evaporative cooling operates by reducing the magnitude of the potential in which the ultracold species is confined, allowing the most energetic of the atoms to escape from the trap. This needs to be performed slowly so as to allow the gas to re-equilibrate once the energetic atoms have escaped, thus lowering the mean energy. This has the effect of lowering the number of ultracold atoms, but vastly lowering the temperature [39] and increasing the phase-space density.

Confinement of the species to be cooled is critical if ultracold temperatures are to be pushed lower, as well as being necessary to attempt to separate the cold species from the buffer gas. For one thing, adsorption onto the walls of the experimental chamber would be a serious issue if magnetic fields were not used to contain the atoms. This technique has even been utilised to create a BEC of metastable He atoms [40]. Ordinarily, the collisions with the cryogenic buffer gas are the method of energy dispersion, but Bose-Einstein condensation has been achieved for hydrogen atoms using the special case of surface-contact [41], whereby contact with the walls

of the experiment removes energetic atoms, without the hydrogen atoms sticking to the chamber walls.

The buffer-gas technique is plausibly a widely applicable method; the only requirement is that the species being cooled survives enough collisions with the helium so as to reach the lowest temperatures.

Atomic deceleration

By using a supersonic expansion of atoms [42], the energy of a thermal atoms can be channelled into forward momentum (this will be further discussed in section 2.2.1. In the moving frame, the velocity distributions equate to temperatures of less than 10 K. As such, there are several techniques available to attempt to decelerate such an atomic beam.

When an atom is placed in a magnetic field, the quantum states of the different spin-orbit projections will split. Some states will be attracted to a high magnetic field (high-field seeking states) and others repelled (low-field seeking states). By firing an atomic beam up a magnetic potential gradient, the atoms will be slowed. If this field is switched off, the atoms will have lost the kinetic energy which had been transferred into potential energy. If this can be repeatedly performed, through the application of pulsed magnetic fields, the atoms can be slowed down to to near zero-velocity [31, 43]. This has been demonstrated for H atoms [44], Ne^* [45] and alkali metal atoms.

Velocity cancellation

As mentioned previously, the atomic beam generates a unidirectional pulse of atoms with a very narrow velocity distribution, but a large forward momentum in the lab-frame. It has been demonstrated that this momentum can be cancelled in the lab-frame by a clever use of a moving nozzle as the source of the beam (depicted in figure 1.3).

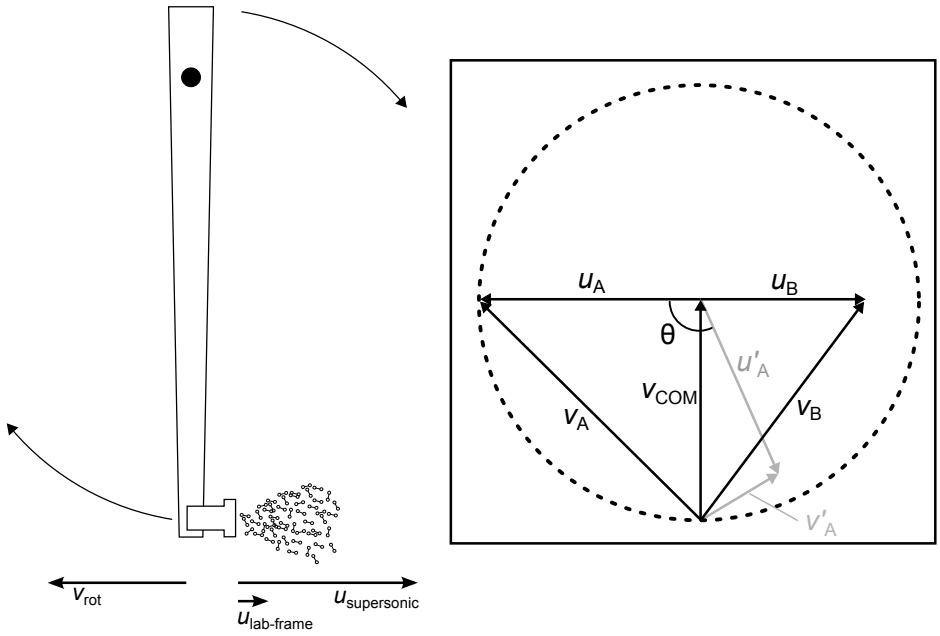

Figure 1.3: Schematics of current techniques available which use velocity cancellation. Left: a supersonic nozzle attached to a rotating armature to counteract the velocity of the molecules being emitted. The lab-frame velocity will be equal to the supersonic ejection speed, minus the rotational velocity of the arm. Right: kinematic velocity cancellation via inelastic collisions. The Newton Sphere highlights the relevant vectors in velocity cancellation. If the centre-of-mass frame recoil velocity of collision partner A is directly opposed to the lab-frame centre-of-mass velocity of the colliding pair, then A will have zero lab-frame final velocity.

A nozzle mounted on a rotating armature [46, 47] can be used to cancel the forward velocity component of a molecular beam. This is a similar technique to that developed by Narevicius and co-workers [48], whereby a beam of helium atoms is reflected off of a silicon surface which is attached to a rotating arm.

1.3.2 Molecular cooling

Molecules are much more difficult to reduce to cold and ultracold temperatures than atoms. One obstacle to the creation of cold molecules has been the difficulty of removing the internal energy arising from the rotational and vibrational modes. But more generally, the non-applicability of laser cooling, because of the lack of closed absorption/emission cycles, has been crucial.

Atomic knitting

Since we have seen that it is possible to cool atoms, it would seem prudent to attempt to bind the atomic species together to make cold molecules. There are various mechanisms by which this can be achieved.

The so-called Feshbach resonance [25], occurs when a bound level of an excited state potential is magnetically tuned into resonance with the energy of the unbound atoms. Usually, the excited state potential will correlate to an excited hyperfine state of one of the colliding atoms. When the atoms then collide, they can form a highly vibrationally excited molecule on the excited potential. Feshbach resonances are thus used to create an ultracold molecule, and have been shown to be able to be cooled far enough to achieve Bose-Einstein Condensation [49].

To achieve this end, the molecule must be internally cooled, for instance by using STImulated Raman Adiabatic Passage (STIRAP) [50, 51], a process by which two near-simultaneous Raman transitions bring about coherence of non-degenerate quantum states, specifically the bound Feshbach state, and the ground state of the molecule. The two states will be brought into coherence by Raman excitation to an intermediate excited state. By careful manipulation of the amplitudes of the two Raman lasers, the molecule will exist in a coherent superposition of initial and final states, and can be transferred into the ground state with very high efficiency.

Cold atoms can also be combined into cold molecules using a technique known as photoassociation [52] (see figure 1.4). It is possible to use a laser pulse to excite two atoms on a ground state potential surface to a high vibrational level of an excited, bound potential. Since photoassociation creates molecules in very high vibrational states, there is a large separation between the atoms when the molecule is formed. This makes photoassociation spectroscopy an interesting proposition [53] from the perspective of investigating high vibrational states. It is also possible to use STIRAP to bring the molecules down to the ground state [54].

The major obstacle with such techniques are that the basic requirement is for

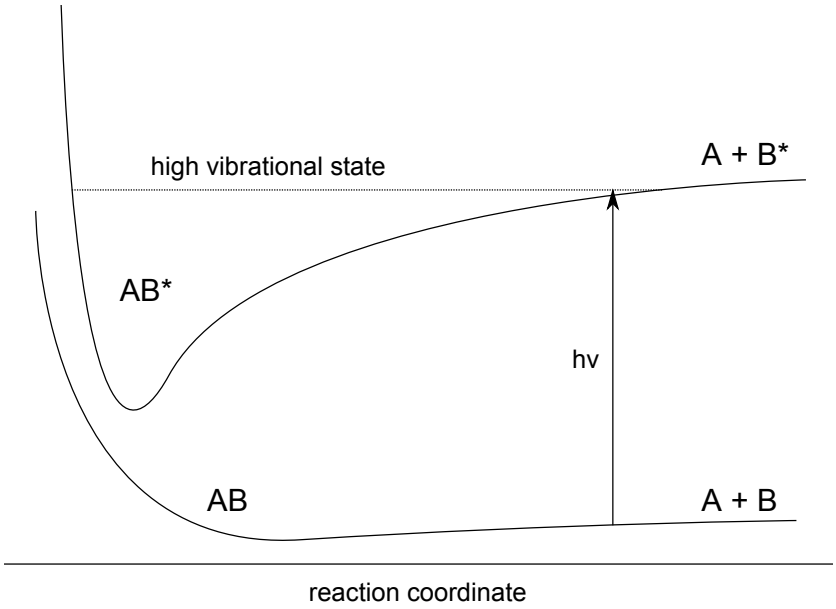

Figure 1.4: One technique for the knitting of ultracold atoms into ultracold molecules. Photoassociation promotes a pair of atoms into a highly vibrationally state of an excited bound state.

appropriate ultracold atomic precursors, and can therefore only currently be applied to the alkali metal cases [55].

Velocity selection

The most direct technique for producing translationally cold molecules from a thermal sample is to separate out the molecules which already have a very small velocity, by capturing the low velocity component of the Maxwell-Boltzmann velocity distribution. For a polar molecule, this can be done by allowing the molecules to fly through a quadrupole electrostatic guide with a right-angled bend [26]. Molecules entering the guide will experience a Stark shift which provides the centripetal force to push them around the bend. This force is only sufficient to guide the slowest around the curve, and fast molecules will fly straight past the electrodes. This is a straightforward velocity selection, and cannot be regarded as true cooling, even though it produces a sample of translationally cold molecules. This technique has been successfully applied to cold chemical reactions in the case of ion-molecule reactions [18].

Atomic analogues

It is not only the internal energy, but also the underlying energy level structure that causes problems when trying to cool molecules. For instance, molecules are difficult to laser cool [30] since the complex rotational, vibrational and electronic structure generally prevents the cycle of absorption and emission from closing; there are many pathways for the photon energy in the system to be dissipated.

The techniques descibed in section 1.3.1 are all applicable to molecular cases, but are all more complex than for the atomic equivalents. Doppler cooling has been recently achieved for the molecular case [56], as has buffer gas cooling [57].

The supersonic molecular beam

A major advantage of the supersonic molecular beam is that the internal degrees of freedom are cooled as a side-effect. Rotational, vibrational and relative kinetic energy are cooled in the molecular beam [42]. The beam is formed from a supersonic gas expansion, whereby the internal energy of the gas is converted into unidirectional kinetic energy. This leaves a fast beam of molecules which are cold in the moving frame. The molecular beam has found wide ranging usage within the realm of spectroscopy, since internal cooling reduces the spectral congestion and the low velocity perpendicular to the molecular beam gives narrower spectroscopic transitions [58]. Molecular beams have also been pivotal in the study of chemical reaction dynamics; indeed, the Nobel prize for chemistry in 1986 was awarded to Herschbach, Polanyi and Lee for the development of the field [59]. Crossed beam experiments (figure 1.5) are particularly indebted to the development of supersonic molecular beams, since the collision-free environment of the beam offers a terrific arena in which to study peturbations to the motion and quantum states of the molecules. This collisionless behaviour also makes the molecular beam a useful tool in the study of highly reactive species, which can be prepared without the worry of adverse reactions before the sample can be interrogated.

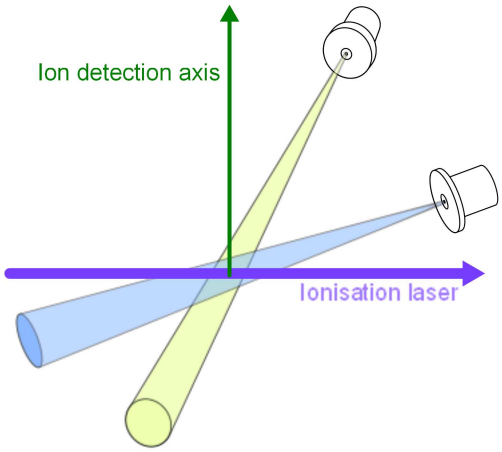

Figure 1.5: Schematic of a typical crossed molecular beam experiment. Two molecular beams will cross at right angles to one another, and the products of the collision can be interrogated.

The counter side to using molecular beam techniques for cold chemistry is that the molecular beam, whilst having an internal temperature of the order of 1 K, has a lab-frame velocity of several hundreds of metres per second (see equation 2.4). An ultracold sample can be prepared by eliminating this velocity component.

Numerous techniques have been developed to apply this apprach to cooling; energy from only one degree of freedom needs to be removed, the unidirectional kinetic energy, which means it can be done in one experimental step. The way in which this energy is removed varies by technique, and is highly dependent upon the internal properties of the molecule.

Molecular electromagnetic deceleration

Section 1.3.1 showed that magnetic fields can be used to bring a sample of atoms down to near-zero velocity, and the electric field analogue of Zeeman deceleration, Stark deceleration, is a useful method in the creation of cold, polar molecules. [27]. The switching sequence of the electric fields is such that a group of molecules passed down the Stark Decelerator with the correct velocities and relative positions, will be reduced to near-zero velocity.

The fact that only certain rovibrational states will be decelerated, makes this

technique highly desirable for molecular cooling. The issues here are that, in order for these techniques to work, the species in question must possess either a permanent electric dipole moment, which makes the method only applicable to certain species; e.g. metastable CO [60] or OH [61].

The Zeeman decelerator has also been applied to the molecular case, for oxygen molecules [62]. The problem with using the Zeeman method for molecular deceleration, is that the molecule in question must be paramagnetic, and such molecules are few and far between.

Optical Stark deceleration

Another method of creating an electric field capable of decelerating polar species is to use pulses of light. Counterpropagating pulsed lasers can generate a moving optical lattice, which has been shown to be able to bring a sample of benzene molecules to a halt in the laboratory [63]. The molecules are trapped in the wells of the optical lattice moving at half the velocity of the molecular beam, which is then switched off after a half-oscillation causing a deceleration of some of the benzene sample. This technique could feasibly be quite general, since it depends upon the electric dipole induced by the laser field (and hence the polarisability) rather than on an intrinsic molecular dipole. This implies that it could be applied to a great many neutral molecules which could not otherwise be decelerated.

Kinematic cooling

Chandler and co-workers have used the inelastic collision dynamics of the NO + Ar reaction [64, 65] to bring a beam of NO to a halt (figure 1.3). Through a carefully executed collision between the NO molecules and the Ar atoms, the recoil vector of the NO molecule and the centre-of-mass velocity of the collision partners can be made to cancel one another out. The directional requirements mean that only a very small fraction of the atoms are able to have their velocities cancelled. Additionally,

in order to have effective vector cancellation, the NO molecule must end up in a highly excited rotational state, since the energetics of the collision produces ground state NO with too large a velocity vector.

This thesis aims to explore using the dynamics of photodissociation as the mechanism of velocity cancellation, in a direct analogue of the inelastic collision scheme above. Increasing the number of chemically significant species is the only way to make cold reactions a viable research area. In addition, widening the scope of accessible species at ultracold temperatures will be of great use in exploring the temperature dependence of various physical phenomena for a greater range of cases.

1.4 Trapping cold species

In order to successfully study chemistry at low temperatures, the particles themselves must be confined spatially so as to interact with another species. Spatial confinement is important in the sense that it is easier to attempt reactive studies upon a stationary target, but more significantly, the confinement prevents the reduction in number density that accompanies the expansion of a cloud of a cold species. In order to see interesting chemistry, it will be essential to create and contain as dense a sample as possible.

Fortunately, cold atoms have a very small amount of kinetic energy, and therefore forces to contain them do not have to be large. Trapping is necessary in order to reach the lowest temperatures – temperatures as low as 100 picoKelvin have been created in the laboratory [66] – and was part of the success of the first MOT [67]. Modern experiments use magnetic coils in an anti-Helmholtz configuration to simultaneously confine two cold atomic gases and attempt to create a bound species using a Feshbach resonance [68]. However, even in the cases where species are at milliKelvin temperatures, confinement is desirable.

The Paul trap [69] is the tool of choice in the field of quadrupole mass spectrometry, and can be used to trap ultracold ions. The trap uses constant DC, and

oscillating radio-frequency electric fields to dynamically trap ions spatially. Alkali earth ions can be loaded into the trap [70], which can form an ordered structure, known as a Coulomb crystal. Other species can be loaded into the trap, and are sympathetically cooled. This leads to a good basis for beginning ultracold reactive ion-molecule studies [71], and has recently been extended to rotational cooling of the molecular species [72]. However, confinement of neutral species is much more challenging.

Optical lattices are commonly used, when attempting to access the lowest temperatures, and are the likeliest current candidates for use in the field of quantum information processing [73]. The lattice is created through the interference of multiple counterpropagating laser beams, creating a stationary wave field within which the atoms experience a Stark shift. The force exerted upon the atoms is enough to confine them to the potentials within the lattice sites; however, since the potential wells in the optical lattices are very shallow, this only can only work for the very coldest of atomic species. Such lattice-confined species have been shown to undergo quantum phase transtions [74], such as from superfluidity to Mott insulation.

There has been much interest in trapping the output of a Stark decelerator. As previously mentioned, the advantage of the decelerator is that ultracold molecules will emerge in a single rovibrational Stark state, creating a pure sample for subsequent studies. Both electrostatic [75] and magnetic [76] traps have been implemented, achieving densities of the order of 10^6 cm^{-3}. This has been shown to be a high enough density to perform collisional studies on such molecules [77], and could be seen as a benchmark density to be achieved for future cold atom or molecule trapping experiments.

A novel technique for the storage of polar molecules using electric fields has been to extend the concept of the synchrotron from charged particles to neutral species [78]. A storage ring made of high voltage electrodes can keep the molecules on stable trajectories which have been recorded to travel over distances of the order of

a mile [79], and multiple molecular packets can be simultaneously loaded, plausibly making it a highly useful arena in which to study low temperature collisions.

Other possibilities include the microwave trap, whereby forces that are derived from the gradient of the microwave radiation field resonant with an atomic transition confine the atomic species in space [80]. This type of trap utilises the AC Stark shift that is associated with transitions from rotational structure in certain polar molecular species as the source of the restorative force. The major advantage here is that there is next to no spontaneous radiation emitted by the atoms, and that they can be trapped in their ground states. The molecular microwave trap is capable of trapping ground state polar molecules in deep wells [81].

There is also the possibility of combining different types of trap. A ring trap has been demonstrated by combining magnetic trapping with a standing optical potential [82]. In addition, the MOT has been combined with a thin wire electrostatic trap (TWIST) to produce a combined electric and magnetic trapping environment for ultracold molecules [83]. This allows for independent trapping of the products of photoassociation from the MOT. In short, there are many opportunities for trapping, both straightforward and complex, with which to confine ultracold species.

1.5 Thesis outline

This thesis concerns itself with the development of the Photostop technique as described by Trottier *et al.* [84], and the applicability of the method to ultracold chemistry in general. Chapter 2 outlines the theory underpinning the method – how the photolysis of small molecules can lead to velocity cancellation in the lab frame – in addition to some brief experimental results to verify the previous work as applied to the NO molecule.

Chapter 3 details the improved prospects for velocity cancellation when applied to the atomic fragment case. The chapter details the experiments performed in collaboration with Wrede and Carty at the University of Durham, to dissociate bromine

molecules into zero-velocity atoms, using the velocity-map imaging technique to elucidate temperatures for the atomic samples generated, as well as some estimates of the number density achievable. It also deals with the simulation of the experimental data, attempting to replicate fully the ballistic expansion of the atomic cloud, and how that relates to the detectable signal witnessed.

In chapter 4, details are given about the attempted construction of a magnetic trap for the bromine atoms, with designs and expected trappable densities envisioned.

Chapter 5 expands upon the previous chapter, and describes the implementation of the chosen trapping scheme. It details how a standard ion imaging set-up in Oxford was converted into the Photostop rig as implemented in Durham, and describes how the detection method was converted into a time-of-flight scheme. The insertion of the magnetic trap into the ion optics is shown, and results for trapping of zero velocity bromine is presented, and compared to the case for which no magnets are present.

The final chapter discusses the successes and shortcomings of the method as a whole, as well as the implications of the trap as implemented. It also touches upon the future of Photostop, and the likely avenues of exploration for future studies.

Bibliography

[1] D. J. Fixsen, The Astrophysical Journal **707**, 916 (2009).

[2] I. Bloch, J. Dalibard, and W. Zwerger, Rev. Mod. Phys. **80**, 885 (2008).

[3] D. L. Moehring, P. Maunz, S. Olmschenk, K. C. Younge, D. N. Matsukevich, L. M. Duan, and C. Monroe, Nature **449**, 68 (2007).

[4] G. K. Campbell and W. D. Phillips, Phil. Trans. Royal Soc. A: MPES **369**, 4078 (2011).

[5] S. N. Bose, Z. für Phys. **26**, 178 (1924).

[6] M. H. Anderson, J. R. Ensher, M. R. Matthews, C. E. Wieman, and E. A. Cornell, Science **269**, 198 (1995).

[7] J. R. Anglin and W. Ketterle, Nature **416**, 211 (2002).

[8] P. W. Atkins, *Physical Chemistry* (OUP, 2010), ninth ed.

[9] J. J. Hudson, D. M. Kara, I. J. Smallman, S. B. E., M. R. Tarbutt, and E. A. Hinds, Nature **473**, 493 (2011).

[10] N. Balakrishnan, J. Chem. Phys. **121**, 5563 (2004).

[11] R. D. Levine, *Molecular Reaction Dynamics* (CUP, 2005).

[12] R. V. Krems, Phys. Chem. Chem. Phys. **10**, 4079 (2008).

[13] N.-N. Liu and H. Loesch, The Journal of Physical Chemistry A **114**, 3247 (2010).

[14] N. Balakrishnan and A. Dalgarno, Chem. Phys. Lett. **341**, 652 (2001).

[15] C. Taatjes and S. Klippenstein, J. Phys. Chem. A **105**, 8567 (2001).

[16] S. R. Mackenzie and T. P. Softley, J. Chem. Phys. **101**, 10609 (1994).

[17] R. D. Guettler, G. C. Jones, L. A. Posey, and R. N. Zare, Science **266**, 259 (1994).

[18] S. Willitsch, M. T. Bell, A. D. Gingell, and T. P. Softley, Phys. Chem. Chem. Phys. **10**, 7200 (2008).

[19] I. R. Sims and I. W. M. Smith, Chem. Phys. Lett. **151**, 481 (1988).

[20] P. Soldán, M. T. Cvitas, J. M. Hutson, P. Honvault, and J.-M. Launay, Phys. Rev. Lett. **89**, 153201 (2002).

[21] W. Gerlach and O. Stern, Z. Phys. A **9**, 353 (1922).

[22] P. A. M. Dirac, *The principles of quantum mechanics* (Clarendon Press, 1981), 4th ed.

[23] L. P. Parazzoli, N. J. Fitch, P. S. Żuchowski, J. M. Hutson, and H. J. Lewandowski, Phys. Rev. Lett. **106**, 193201 (2011).

[24] S. Händel, T. P. Wiles, A. L. Marchant, S. A. Hopkins, C. S. Adams, and S. L. Cornish, Phys. Rev. A **83**, 053633 (2011).

[25] H. Feshbach, Annals Phys. **5**, 357 (1958).

[26] T. Junglen, T. Rieger, S. A. Rangwala, P. W. H. Pinkse, and G. Rempe, Eur. Phys. J. D **31**, 365 (2004).

[27] M. Kirste, B. G. Sartakov, M. Schnell, and G. Meijer, Phys. Rev. A **79**, 051401 (2009).

[28] E. L. Raab, M. Prentiss, A. Cable, S. Chu, and D. E. Pritchard, Phys. Rev. Lett. **59**, 2631 (1987).

[29] J. Kim, B. Friedrich, D. P. Katz, D. Patterson, J. D. Weinstein, R. DeCarvalho, and J. M. Doyle, Phys. Rev. Lett. **78**, 3665 (1997).

[30] M. T. Bell and T. P. Softley, Mol. Phys. **107**, 99 (2009).

[31] N. Vanhaecke, U. Meier, M. Andrist, B. H. Meier, and F. Merkt, Phys. Rev. A. **75**, 031402 (2007).

[32] C. J. Foot, *Atomic Physics* (OUP, 2004).

[33] J. P. Morrison, C. J. Rennick, and E. R. Grant, Phys. Rev. A **79**, 062706 (2009).

[34] T. Pohl, H. R. Sadeghpour, and P. Schmelcher, Phys. Rep. - Rev. Sec. Phys. Lett. **484**, 181 (2009).

[35] T. Könemann, W. Brinkmann, E. Göklü, C. Lämmerzahl, H. Dittus, T. van Zoest, E. Rasel, W. Ertmer, W. Lewoczko-Adamczyk, M. Schiemangk, et al., Appl. Phys. B **89**, 431 (2007).

[36] J. T. Bahns, W. C. Stwalley, and P. L. Gould, J. Chem. Phys. **104**, 9689 (1996).

[37] D. Meschede, W. Jhe, and E. A. Hinds, Phys. Rev. A **41**, 1587 (1990).

[38] H. W. Chan, A. T. Black, and V. Vuletić, Phys. Rev. Lett. **90**, 063003 (2003).

[39] Z.-Y. Ma, A. M. Thomas, C. J. Foot, and S. L. Cornish, J. Phys. B **36**, 3533 (2003).

[40] S. C. Doret, C. B. Kennedy, W. Ketterle, and J. M. Doyle, Phys. Rev. Lett. **103**, 103005 (2009).

[41] D. G. Fried, T. C. Killian, L. Willman, D. Landhuis, S. C. Moss, D. Kleppner, and T. J. Greytak, Phys. Rev. Lett. **81**, 3811 (1998).

[42] G. Scoles, *Atomic and Molecular Beam Methods* (OUP, New York, 1988).

[43] E. Narevicius, A. Libson, C. G. Parthey, I. Chavez, J. Narevicius, U. Even, and M. G. Raizen, Phys. Rev. A. **77**, 051401 (2008).

[44] S. D. Hogan, A. W. Wiederkehr, H. Schmutz, and F. Merkt, Phys. Rev. Lett. **101**, 143001 (2008).

[45] A. W. Wiederkehr, M. Motsch, S. D. Hogan, M. Andrist, H. Schmutz, B. Lambillotte, J. A. Agner, and F. Merkt, J. Chem. Phys. **135**, 214202 (2011).

[46] M. Gupta and D. Herschbach, J. Phys. Chem. A **103**, 10670 (1999).

[47] M. Strebel, F. Stienkemeier, and M. Mudrich, Phys. Rev. A **81**, 033409 (2010).

[48] E. Narevicius, A. Libson, M. F. Riedel, C. G. Parthey, I. Chavez, U. Even, and M. G. Raizen, Phys. Rev. Lett. **98**, 103201 (2007).

[49] M. Junker, D. Dries, C. Welford, J. Hitchcock, Y. P. Chen, and R. G. Hulet, Phys. Rev. Lett. **101**, 060406 (2008).

[50] E. Kuznetsova, M. Gacesa, P. Pellegrini, S. F. Yelin, and R. Côté, New J. Phys. **11**, 055028 (2009).

[51] K. Winkler, F. Lang, G. Thalhammer, P. v. d. Straten, R. Grimm, and J. H. Denschlag, Phys. Rev. Lett. **98**, 043201 (2007).

[52] M. Viteau, A. Chotia, M. Allegrini, N. Bouloufa, O. Dulieu, D. Comparat, and P. Pillet, Phys. Rev. A **79**, 021402 (2009).

[53] P. D. Lett, P. S. Julienne, and W. D. Phillips, Annual Rev. Phys. Chem. **46**, 423 (1995).

[54] K.-K. Ni, S. Ospelkaus, M. H. G. de Miranda, A. Pe'er, B. Neyenhuis, J. J. Zirbel, S. Kotochigova, P. S. Julienne, D. S. Jin, and J. Ye, Science **322**, 231 (2008).

[55] C. A. R. Markus Greiner and D. S. Jin, Nature **426**, 537 (2003).

[56] E. S. Schuman, J. F. Barry, and D. DeMille, Nature **467**, 820 (2010).

[57] J. D. Weinstein, R. deCarvalho, T. Guillet, B. Friedrich, and J. M. Doyle, Nature **395**, 148 (1998).

[58] R. E. Smalley, B. L. Ramakrishna, D. H. Levy, and L. Wharton, J. Chem. Phys. **61**, 4363 (1974).

[59] Y. T. Lee, J. D. McDonald, P. R. Lebreton, and D. R. Herschbach, J. Chem. Phys. **49**, 2447 (1968).

[60] J. H. Blokland, J. Riedel, S. Putzke, B. G. Sartakov, G. C. Groenenboom, and G. Meijer, J. Chem. Phys. **135**, 114201 (2011).

[61] B. C. Sawyer, B. K. Stuhl, D. Wang, M. Yeo, and J. Ye, Phys. Rev. Lett. **101**, 203203 (2008).

[62] E. Narevicius, A. Libson, C. G. Parthey, I. Chavez, J. Narevicius, U. Even, and M. G. Raizen, Phys. Rev. A **77**, 051401 (2008).

[63] A. I. Bishop, L. Wang, and P. F. Barker, New J. Phys. **12**, 073028 (2010).

[64] M. S. Elioff, J. J. Valentini, and D. W. Chandler, Science **302**, 1940 (2003).

[65] J. J. Kay, J. Kłos, M. H. Alexander, K. E. Strecker, and D. W. Chandler, Phys. Rev. A **82**, 032709 (2010).

[66] J. Tuoriniemi and T. Knuuttila, Physica B **280**, 474 (2000).

[67] A. L. Migdall, J. V. Prodan, W. D. Phillips, T. H. Bergeman, and H. J. Metcalf, Phys. Rev. Lett. **54**, 2596 (1985).

[68] H. Cho, D. McCarron, D. L. Jenkin, M. P. Köppinger, and S. L. Cornish, Eur. Phys. J. D **65**, 125 (2011).

[69] R. E. March, J. Mass Spectr. **32**, 351 (1997).

[70] K. Mølhave and M. Drewsen, Phys. Rev. A **62**, 011401 (2000).

[71] S. Willitsch, M. T. Bell, A. D. Gingell, S. R. Procter, and T. P. Softley, Phys. Rev. Lett. **100**, 043203 (2008).

[72] P. F. Staanum, K. Højbjerrel, P. S. Skyt, A. K. Hansen, and M. Drewsen, Nature Phys. **6**, 271 (2010).

[73] G. K. Brennen, C. M. Caves, P. S. Jessen, and I. H. Deutsch, Phys. Rev. Lett. **82**, 1060 (1999).

[74] M. Greiner, O. Mandel, T. Esslinger, T. W. Hänsch, and I. Bloch, Nature **415**, 39 (2002).

[75] J. J. Gilijamse, S. Hoekstra, N. Vanhaecke, S. van de Meerakker, and G. Meijer, Eur. Phys. J. D **57**, 33 (2010).

[76] J. Riedel, S. Hoekstra, W. Jäger, J. Gilijamse, S. van de Meerakker, and G. Meijer, Eur. Phys. J. D **65**, 161 (2011).

[77] B. C. Sawyer, B. K. Stuhl, D. Wang, M. Yeo, and J. Ye, Phys. Rev. Lett. **101**, 203203 (2008).

[78] C. E. Heiner, D. Carty, G. Meijer, and H. L. Bethlem, Nature Phys. **3**, 115 (2007).

[79] P. C. Zieger, S. Y. T. van de Meerakker, C. E. Heiner, H. L. Bethlem, A. J. A. van Roij, and G. Meijer, Phys. Rev. Lett. **105**, 173001 (2010).

[80] C. C. Agosta, I. F. Silvera, H. T. C. Stoof, and B. J. Verhaar, Phys. Rev. Lett. **62**, 2361 (1989).

[81] D. DeMille, D. R. Glenn, and J. Petricka, Eur. Phys. J. D **31**, 375 (2004).

[82] O. Morizot, Y. Colombe, V. Lorent, H. Perrin, and B. M. Garraway, Phys. Rev. A **74**, 023617 (2006).

[83] J. Kleinert, C. Haimberger, P. J. Zabawa, and N. P. Bigelow, Rev. Sci. Instr. **78**, 113108 (2007).

[84] A. Trottier, E. Wrede, and D. Carty, Mol. Phys. **105**, 725 (2010).

Chapter 2

Photostop theory

A major stumbling block in the area of ultracold science has been the difficulty of generating a wide range of cold species, and storing them long enough for interrogation. In general, highly specialised equipment is required, such as in the case of the Stark decelerator [1], or many coincidental lasers must be simultaneously overlapped, as in the case of the MOT [2]. Thus, it would be highly desirable to create a more generally applicable method to bring atoms and molecules to a halt. The Photostop experiment seeks to use the recoil velocity of a photofragment created during a photolysis process to cancel the velocity of the precursor species, in an analagous way to that which has been demonstrated by Chandler and co-workers with elastic collisions between NO and Ar [3], as described in section 1.3.

A sensible question to ask at this stage, when looking to create a sample of cold atoms or molecules for use in a chemical reaction, would be why choose the Photostop technique? As described in chapter 1, there are already many techniques available to manufacture either cold atoms or molecules. If our main goal is to study chemical reactions, rather than just cool down the species, then surely more advanced laser cooling techniques should be used. However, such methods can be very difficult to construct and operate. So what are the benefits of this technique?

First and foremost, the Photostop method is experimentally and conceptually more straightforward than many of the more mainstream techniques. From an ex-

perimental perspective, the set-up is very much the same as you would find in any standard ion imaging laboratory, and requires only two coincidental laser beams. It could be argued then, that the Photostop method offers an easily accessible arena in which to perform spectroscopy on ultracold samples; it should offer longer interrogation durations, and thus more precise measurements than traditional molecular beam spectroscopy. All of this means that for many groups, it may be a readily accessible way to interrogate an ultracold sample.

The ability to generalise the technique to other species is the other main advantage of Photostop; since any molecule can be photolysed, there is a reasonable probability than any number of fragments could be cooled to ultracold temperatures, greatly extending the scope of low-temperature chemistry. It is therefore possible that, in investigating the viability of the technique, we find a rival to the established methods of cold atom and molecule generation, which would be a highly exciting prospect, scientifically. The main drawback of the technique lies in finding an accessible state of the precursor molecule near to the dissociation threshold, as discussed in section 2.2.2.

2.1 Photodissociation

Photodissociation is one of the most basic of all chemical processes. Photolysis plays an essential role in interstellar chemistry, being the major process by which molecules are broken down [4], and, closer to home, is one of the most important processes in the atmosphere of planet Earth [5]. In the troposphere, two of the most significant reactions are:

$$O_3 + h\nu -> O_2 + O(^1D), \tag{2.1}$$

and

$$O(^1D) + H_2O \longrightarrow 2\,OH. \tag{2.2}$$

Radicals are amongst the most critical components of atmospheric chemistry; for instance, the hydroxyl radical is central to many decontamination processes [6]. Oxygen radicals themselves are critical in the formation of the protective ozone layer, however, photodissociation has also been shown to cause the damaging reverse reaction [7]. Photolysis has therefore been extensively studied, and the dissociation schemes of many molecules, large and small, have been catalogued in great detail.

Many methods have been used to elucidate data from photolysis experiments. The rates of gas phase decomposition have long been monitored using absorption techniques, which can be analysed using the Beer-Lambert law [8]. More modern experiments attempt to detect the fragments in a more detailed manner, measuring the kinetic energy released [9] by way of time-of-flight (TOF) measurements [10]. The most recent techniques available are able to reconstruct the full velocity and angular distributions of the fragments [11], and current techniques are being developed to allow full velocity, angular and temporal distributions to be determined simultaneously [12, 13]. Such techniques could all be useful in determining whether a given photolysis process will be able to give us zero-velocity fragments.

It is important to note that in a photolysis process, there is a requirement for a bound to unbound electronic transition in the wavelength of interest, so as to dissociate the molecule rather than creating an excited bound state. Previous investigation [14] has shown that certain simple molecules (NO, CO and NH_3) may not have the correct energetics for facile velocity cancellation using photodissociation, and therefore inviable as proof-of-principle precursor molecules.

2.2 The Photostop technique

The concept of velocity cancellation using photodissociation as the mechanism to produce cold NO molecules was first postulated by Matthews and co-workers [15] in 2007. The method was first proven by Zhao and co-workers [16], though the molecules were only witnessed to stay in the detection region for a few hundred

nanoseconds. The first methodical probing of Photostop was demonstrated by Trottier and co-workers [17] in 2010. The Photostop technique attempts to use photodissociation as a mechanism of bringing the narrow velocity distribution (and therefore kinetically cold) from molecular beam speeds to being centered around zero-velocity in the lab-frame.

In a photodissociation process, the difference between the photon energy and bond energy goes into the recoil kinetic energy of the fragments in the centre-of-mass (COM) frame and also the internal energy of the fragments. The lab-frame velocity of the fragment is then the vector sum of this recoil velocity with the original parent molecule's LF velocity. Controlling the photolysis energy and angle of fragmentation, the LF velocity of one of the radical fragments can be varied arbitrarily, and reduced to zero under the right conditions. This is best illustrated through the use of a Newton Diagram (see Figure 2.1). The Photostop technique attempts to maximise the proportion of fragments which are produced with zero lab-frame velocity.

There are two main factors that need to be considered: the spatial and energy distributions of the fragments. The ring in the Newton diagram represents the Newton sphere, the radius of which in velocity space is proportional to the square root of the kinetic energy release of the dissociation process. If the radius of this sphere is the same magnitude as the molecular beam velocity then, at a recoil angle of -180° when compared with the molecular beam direction, the velocities will cancel. This recoil angle is measured relative to the electric vector, ϵ, of the dissociation laser.

2.2.1 The molecular beam

The method by which a room-temperature sample of gas is converted into a unidirectional beam with a narrow velocity distribution is via supersonic expansion of the gas through a nozzle. Pulsing at 10 Hz limits the gas load, and therefore the

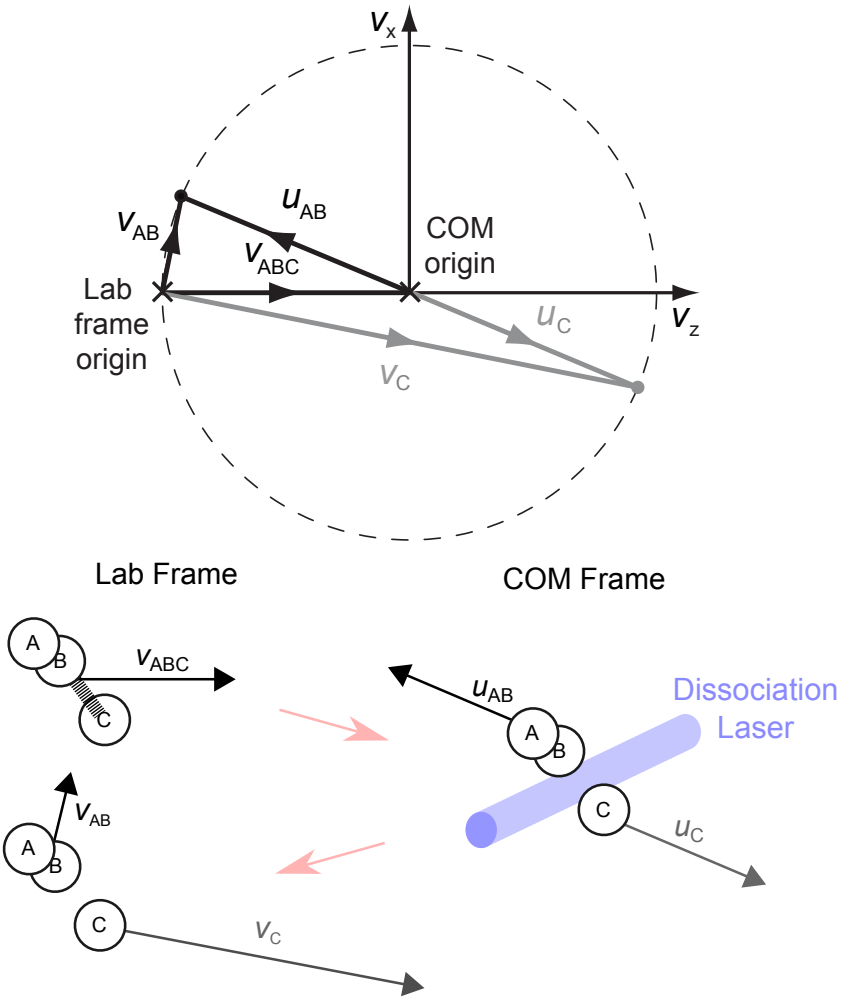

Figure 2.1: Newton diagram detailing the relevant vectors for dissociation of a triatomic molecule, ABC. In the diagram, v is used for lab-frame velocities and u for COM-frame velocities. If u_{AB} is equal and opposite to v_{ABC}, then v_{AB} will be zero. The motions of the atoms in the relevant reference frames are shown underneath the Newton Diagram.

background pressure in the vacuum system, in addition to the requirements on the pumping system. This achieves a beam of molecules which can reach a translational temperature of down to 1 K in the COM frame; the use of a higher backing pressure may give rise to a lower temperature but this may lead to cluster formation in the beam [18]. The mechanism by which the molecular beam is created is well-documented, but highly complex [19, 20]. The energy equation is given by,

$$h + \frac{v^2}{2} = h_0, \tag{2.3}$$

where h is the system enthalpy, v is the velocity, and h_0 is the enthalpy at the stagnation source, i.e. the nozzle, and is a constant. The pressure gradient between the source and the vacuum provides the flow work; as the gas expands out of the nozzle, the enthalpy decreases, leading to an increase in velocity along the axis of ejection.

It is not just the acceleration of the molecules along one axis that is of interest. The kinetic energy of the molecules is high, but this energy has to have come from somewhere. The rotational and vibrational energies of the molecules have essentially been channelled into kinetic energy in the supersonic expansion, and as such, the beam is internally cold. Using a Boltzmann style distribution of states to calculate a temperature, it is common to find molecular beams temperatures of 1-10 K. However, the redistribution of energy is not comparably efficient; specifically, vibrational energy redistribution is not as efficient as for kinetic or rotational energy redistribution [21]. As such, it is common to find that a molecular beam source will contain a significant minority of $v = 1$ states.

Combined with a skimmer, which removes molecules with higher perpendicular velocities, the molecular beam provides a well-collimated set of molecules in a collision-free environment, with very well defined trajectories, and cooled internal

degrees of freedom. The terminal velocities can be described by equation 2.4:

$$v_\infty = \sqrt{\frac{2R}{W}\left(\frac{\gamma}{\gamma - 1}\right)T_0}, \tag{2.4}$$

where v_∞ is the terminal velocity of the molecular beam, R is the molar gas constant, W is the molecular weight, and $\gamma = C_p/C_V$, the ratio of the heat capacity at constant pressure to that at constant volume. In addition, for a mixture of two gases, the weightings of the two gases in the mixture are taken into account:

$$v_\infty = \sqrt{\frac{2R}{\sum_i \chi_i W_i}\left(\sum_i \chi_i \frac{\gamma_i}{\gamma_{i-1}}\right)T_0}. \tag{2.5}$$

where χ_i refers to the mole fraction of species i. The target species can be seeded in a rare gas to gain some control of the terminal velocity, since the final velocity will be dependent upon the weighted molecular masses, as shown in equation 2.5. Using an excess of the rare gas, the final velocity will be closer to that of a pure beam of the carrier gas. The main carrier gases used in the velocity cancellation studies are argon, krypton and xenon, and their respective terminal velocities are approximately 560, 385 and 310 ms^{-1}. If we assume a molecular beam temperature of 5 K, then this creates a Gaussian velocity distribution centered at the terminal velocity, with a full-width half-maximum (FWHM) spread of around 10 % of the total velocity of the beam. 5 K is a reasonable temperature to assume from previous molecular beam studies.

The internal temperature of the gas can be verified spectroscopically. In the case of NO_2, a rotational spectrum of the residual NO in the molecular beam can be recorded, which can then be simulated. The spectrum has been simulated using the PGOPHER software [22] and the relative amplitudes of the rotational lines at T = 5 K most closely match the experimental data. The comparison is shown in figure 2.2.

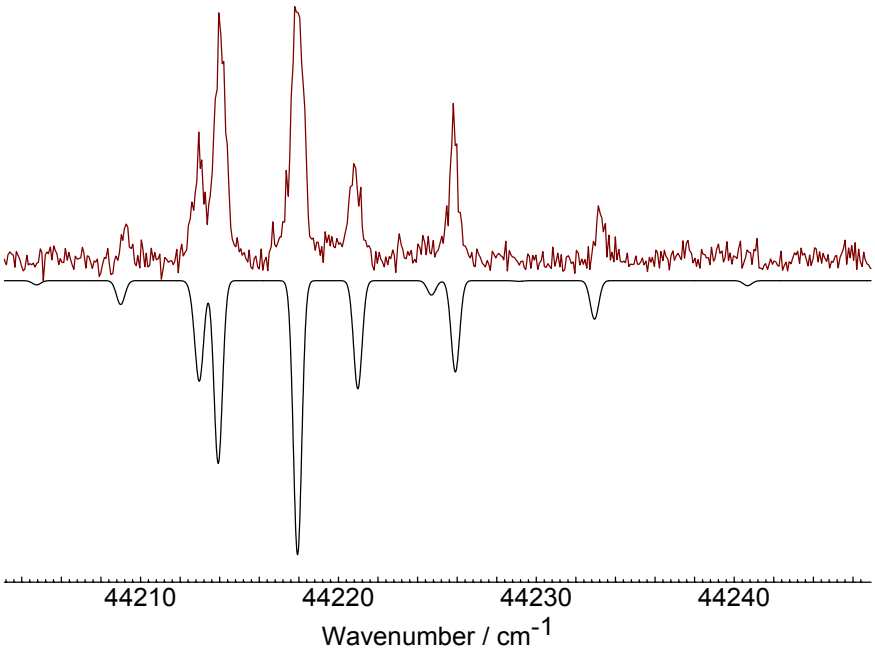

Figure 2.2: Rotational spectrum of NO, taken within the molecular beam. The temperature of the beam is simulated from PGOPHER to be around 5 K. The spectrum is in red, and the lower graph is the PGOPHER simulation.

2.2.2 Energy distribution of fragments

Newton's First Law of Thermodynamics states that the internal energy of a closed system is equal to the heat put in minus the work performed by the system onto its surroundings. In other words: the energy of the system must be conserved. When molecules dissociate, energy must be conserved in accordance with the First Law. The system here is the molecule, and the energy input comes from a laser photon. The total energy after dissociation must be equal to the inital energy of the molecule, plus the photon energy. Therefore, it is straightforward to establish the recoil energetics of the photodissociation process. For instance, in the dissociation of a triatomic molecule, ABC, in the laboratory frame:

$$h\nu + E_{\text{kin}}^{\text{ABC}} + E_{\text{int}}^{\text{ABC}} - D_0 = E_{\text{available}}^{\text{AB+C}}, \tag{2.6}$$

where $h\nu$ is the energy of the dissociation photon, $E_{\text{kin}}^{\text{ABC}}$ and $E_{\text{int}}^{\text{ABC}}$ are the kinetic and internal energies respectively of the precursor molecule, D_0 is the zero-point

dissociation energy of the process, and $E^{\mathrm{AB+C}}_{\mathrm{available}}$ is the total energy available to the departing fragments. $E^{\mathrm{AB+C}}_{\mathrm{available}}$ can be described as such:

$$E^{\mathrm{AB+C}}_{\mathrm{available}} = E^{\mathrm{AB}}_{\mathrm{kin}} + E^{\mathrm{C}}_{\mathrm{kin}} + E^{\mathrm{AB}}_{\mathrm{int}} + E^{\mathrm{C}}_{\mathrm{int}}. \tag{2.7}$$

Equation 2.6 simplifies when we consider the equation in the COM frame. In this frame of reference, the kinetic energy of the parent molecule is zero, hence:

$$h\nu + E^{\mathrm{ABC}}_{\mathrm{int}} - D_0 = E^{\mathrm{AB+C}}_{\mathrm{kin}}(COM) + E^{\mathrm{AB}}_{\mathrm{int}} + E^{\mathrm{C}}_{\mathrm{int}}, \tag{2.8}$$

where

$$E_{\mathrm{kinAB+C}}(COM) = E^{\mathrm{AB}}_{\mathrm{kin}}(COM) + E^{\mathrm{C}}_{\mathrm{kin}}(COM). \tag{2.9}$$

The COM kinetic energy available to each fragment is related to the ratios of the masses of each species; a lighter fragment will take the majority of the kinetic energy available in the system (Equation 2.10).

$$E^{\mathrm{C}}_{\mathrm{kin}}(COM) = \frac{m_{\mathrm{AB}}}{m_{\mathrm{C}} + m_{\mathrm{AB}}} E^{\mathrm{AB+C}}_{\mathrm{kin}}(COM). \tag{2.10}$$

The velocity spread of the final sample will be dependent on the partitioning of energy between the number of possible dissociation pathways available. For instance, if there are many rotational quantum states available to a fragment, then there will be many different ways to partition the kinetic energy, reducing the possibility of producing fragments at an exact recoil speed:

$$v_{\mathrm{C}} = \sqrt{\frac{2m_{\mathrm{AB}}}{m_{\mathrm{C}}(m_{\mathrm{C}} + m_{\mathrm{AB}})} E_{\mathrm{available}}(COM)} \tag{2.11}$$

It is worth noting that E^{ABC}_{int} is normally very low in a molecular beam precursor, as detailed in section 2.2.1, and therefore contributes little to the overall energy distribution.

It is all well and good at this stage declaring that dissociation of a molecule with a photon at a given energy can bring about velocity cancellation, but there are other factors to consider. The linewidth of the dissociation laser means that there will be a (narrow) distribution of input energies, $h\nu$, leading to a distribution of energies available to the fragments. In addition, there is a spread of velocities of the parent molecules in the supersonic expansion, despite the low translational temperatures [19]. As a result, not all precursor molecules will have a velocity vector which is capable of being cancelled. Both of these factors will diminish the probability that any given fragment will be formed with zero-velocity after the dissociation event.

It is plain to see from equation 2.11 that the recoil velocity is proportional to the square root of the available kinetic energy, and thus highly dependent upon the energy provided by the dissociation photon. This illustrates the point that the higher above the dissociation threshold at which photolysis occurs, the greater the recoil velocity. Since we are attempting to match the recoil velocity to the molecular beam velocity, a higher recoil velocity necessitates a higher beam velocity. As a higher molecular beam velocity is broadly associated with a greater velocity spread, it is preferable to use as low a molecular beam velocity as possible, and by extension, it is desirable to dissociate as close to the dissociation threshold as possible.

It is clear from the energetic requirements that dissociation near to threshold is at least useful, maybe even a necessity. Hence, it required that there is a dissociative potential energy surface near to the threshold, to which the precursor molecule can be excited to bring about fragmentation. This requirement is likely to be a major barrier to finding species which can be used as the parent molecule for the experiment.

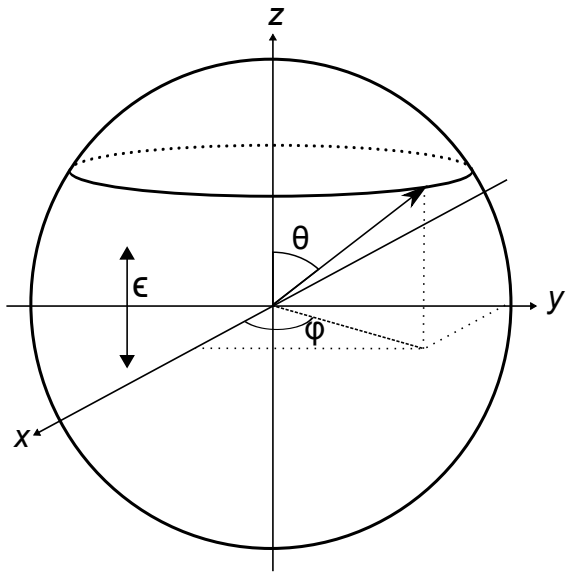

Figure 2.3: Schematic of the co-ordinate system, where z is the axis of the molecular beam, and also the axis of the laser polarisation, ϵ.

2.2.3 Angular distribution of fragments

The description of the interaction between light and matter can be conveniently described with standard perturbation theory, linking the transition dipole moment $\mu_{fi} = \langle f|\mu|i\rangle$ to the probability of photon absorption. The photon absorption probability is at a maximum when its E-field vector, ϵ, is parallel to μ_{fi} [23]. For the case of simple diatomic molecules, μ_{fi} is generally either parallel to, or perpendicular to the molecular axis, and as such, dissociation is most likely to be along one of these axes.

In the photodissociation process, the angular distribution of fragments is determined by the route of dissociation. The electronically excited state through which the dissociative pathway proceeds will determine the recoil angle of the fragments relative to ϵ of the dissociation laser, defined in figure 2.3. The fragment recoil velocity must be not only be equal in magnitude, but opposite in direction, in order for it to cancel with the molecular beam velocity vector.

For one-photon dissociation, the angular distribution of a dissociation can be reduced to a dependence upon one variable, β, the angular anisotropy parameter,

when expressed in terms of Legendre polynomials [24].

$$I(\theta) = \frac{\sigma}{4\pi}(1 + \beta P_2(\cos(\theta))). \tag{2.12}$$

In this equation, σ is the photodissociation cross-section, θ is the angle between the electric vector of the dissociation laser, ϵ, and the velocity vector of the departing fragment (see figure 2.3), and $P_2(\cos(\theta))$ is the second Legendre Polynomial:

$$P(x) = \frac{1}{2}(3x^2 - 1). \tag{2.13}$$

To calculate the probability of a specific fragmentation angle θ, it is necessary to integrate equation 2.12 over θ.

The classical limits of this parameter are $\beta = +2$, where the fragmentation primarily occurs parallel to the axis of ϵ, and $\beta = -1$, the perpendicular limit. If dissociation were to occur isotropically, then there would be a very small number of fragments recoiling back along the molecular beam axis. To achieve maximum velocity cancellation, we require that the recoil of the fragments occur along the axis of the molecular beam. Thus, ϵ can be aligned along the said axis, and a dissociative pathway with a β value near the parallel limit is ideal.

β is a difficult variable to calculate from first principles, as it is a function of the energy available upon dissociation, and which product channels are active. It is therefore affected by the mixing of the electronically excited states. Hence, when selecting a precursor species, it is best to work with a system which has been heavily studied, and for which the β parameter has been experimentally verified.

2.3 Verification of the Photostop method with NO

NO is a very chemically significant molecule that has been widely studied, owing to its status as one of the simplest radical molecules, and also by virtue of its strong

resonances in its REMPI spectrum, making it easily detectable [25]. Whilst it is rarely used commercially, it is a very important molecule biologically [26–28]. NO is also present in the atmosphere; it has been implicated in the destruction of the ozone layer [29].

Given the significance of NO, it is therefore an attractive candidate for study at ultracold temperatures: its well documented REMPI spectrum will make it a good test subject for testing the improvement in resolution of spectroscopic lines at the lowest temperatures, and as a radical species, it may well have some near-barrierless reactive pathways which were highlighted in chapter 1 as being likely scenarios in which quantum reactive behaviour may be observed. However, the major advantage of choosing NO is that it is experimentally feasible to create at low temperatures, and detect in small quantities, due to the aforementioned strong REMPI spectrum.

Previous studies into the anisotropy of the photodissociation of NO_2 [15, 30] have shown that the β parameter fluctuates wildly directly at threshold, but it emerges that around 300 cm^{-1} over the dissociation limit this levels off to around $\beta = +1.5$, a dissociation largely parallel to the laser polarisation. Combined with the fact that NO_2 absorbs strongly near threshold, it should be possible to stop either NO molecules or O atoms. Past attempts to implement the method for cold molecule formation have used NO_2 dissociation to create zero-velocity NO molecules [16, 17]. Other ideas have been to try and velocity cancel SO molecules from a Stark decelerated beam of SO_2 [31], since the SO_2 can be dissociated almost directly at the dissociation threshold – though deceleration of SO_2 is not straightforward in itself [32]. The following work in this thesis was performed in collaboration with Wrede and Carty at the University of Durham, who had an apparatus set up with the correct geometry for these experiments.

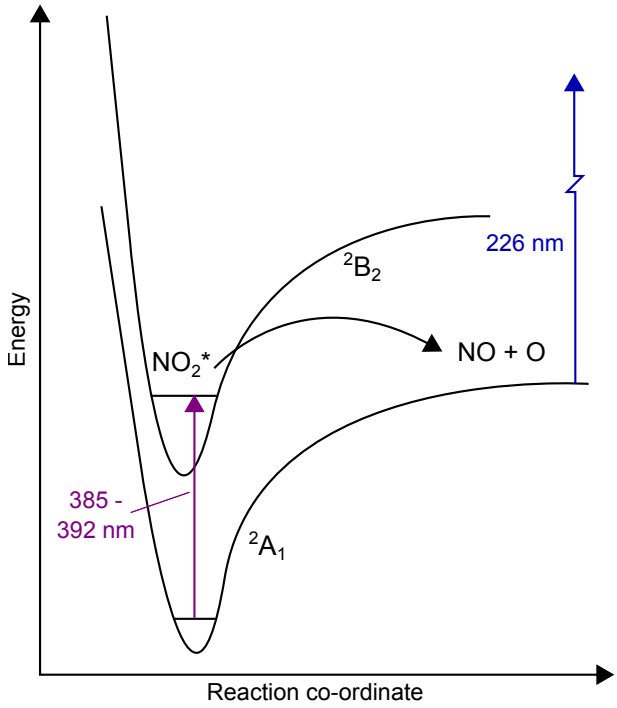

Figure 2.4: Energy level diagram for the dissociation of NO_2 molecule. The dissociation photon excites the molecule from the $^2A_1$ ground state to the $^2B_2$, where it predissociates into NO + O. The NO is then probed using a (1 + 1) REMPI process.

2.4 The Photostop experiment

2.4.1 Dissociation of NO_2

The dissociation of NO_2 has been widely studied, since both statistical and state-specific features have been witnessed in the photolysis of the NO_2 molecule. The dissociation pathway utilised in the experiment is shown in figure 2.4.

The dissociation threshold is $D_0 = 25128.56$ cm^{-1} [33], and the near-threshold dissociation has been extensively investigated in its own right [15, 30, 34]. Most significantly, the studies show a great deal of variation of the β parameter close to threshold [35]. The mechanics of the dissociation process are shown in figure 2.5. If we assume that dissociation is infinitely fast over the timescale of the rotation of the molecule then [36],

$$\beta_{lim} = 2P_2(\cos(\chi)) \tag{2.14}$$

where χ is the angle between the laser polarisation vector and the vector $\mathbf{R}$ where

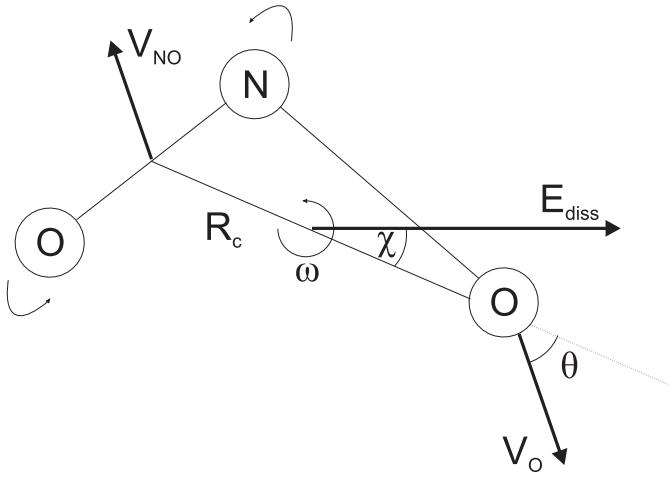

Figure 2.5: Dissociation dynamics of the NO_2 molecule.

R is the initial distance between the departing O atom and the COM of the NO fragment. The available energy affects the β parameter, which depends upon the transverse recoil angle $\varphi(\mathrm{E_{avl}})$ [36].

$$\beta_{\mathrm{limit}}(E_{\mathrm{avl}}) = P_2(\cos(\chi + \varphi(E_{\mathrm{avl}}))) + P_2(\cos(\chi - \varphi(E_{\mathrm{avl}}))), \tag{2.15}$$

where the transverse recoil angle is the angle between $\mathbf{R}$ and the oxygen velocity vector. E_{avl} is the excess energy over the threshold for production of a given rotational quantum state. To determine $\varphi(\mathrm{E}_{avl})$, we can use the classical expression [36],

$$\sin^2\varphi(E_{\mathrm{avl}}) = \frac{\mu_{\mathrm{NO}} r^2 E_{\mathrm{rot}}}{\mu_{\mathrm{NO_2}} \mathbf{R}^2 E_{\mathrm{avl}}}, \tag{2.16}$$

where r is the NO internuclear distance. However, near the dissociation threshold, the dissociation can be slow compared to the rotational period. This modifies β to become an average quantity [37].

$$< \beta > (E_{\mathrm{avl}}) \approx \beta_{\mathrm{limit}}(E_{\mathrm{avl}}) \frac{P_2(\cos\alpha) + (\omega < \tau >)^2 - 3\omega < \tau > \sin\alpha\cos\alpha}{1 + 5(\omega < \tau >)^2}, \tag{2.17}$$

where $\omega < \tau >$ is the angular velocity of rotation of the parent molecule, multiplied

by its average lifetime, and α is a tipping angle [37]:

$$\alpha = \arctan\left(\frac{v_t}{u}\right), \tag{2.18}$$

where u is the COM recoil velocity of NO and v_t is the tangential velocity of the separating fragments. All of this leads to complex dissociation dynamics.

2.4.2 Photofragment ion imaging

One of the most powerful modern techniques for the study of molecular reaction dynamics has involved the ionisation of the products of a photodissociation process. In 1987, Chandler and Houston developed the method of photofragment ion imaging [38]; the photofragments were ionised in the electric field gradient created by a repelling plate held at a fixed potential and two grounded plates, which then accelerate the ions towards a position sensitive imaging detector. The great advantage of the ion imaging technique is that, through the 2-dimensional crushing of the ions onto the detector, we can witness the angular distribution of the fragments as they are ejected, as well as their relative velocities. The direct imaging of the ions represented a major step forwards in the field of molecular reaction dynamics, as the internal energies of the parent molecule and fragments all play a part in determining the kinetic energy of the resultant fragments.

REMPI

Resonance Enhanced Multi-Photon Ionization, or REMPI, is the tool of choice for ionisation in photofragment ion imaging. It also allows for ionization and detection of species which are unsuitable for detection by laser induced fluorescence (LIF). LIF excites a transition within the species, and monitors the fluorescence as it relaxes back to the ground state. This gives a spectrum, as emitted photons correspond to relaxation back to particular rotational states. As LIF is an emissive technique, rather than an absorption method, it makes it a very easy way of measuring signal,

since you only need an optical detection system, such as a camera.

A major advantage of the REMPI scheme is the ability to measure the velocities of the ions as they collide with the detector, by using a position sensitive detection scheme. This is a critical advantage for a scheme involving velocity cancellation, where we are attempting to extract the velocity distribution from the stopped species. It is possible to measure the velocity distribution of the stopped atoms using LIF; the Doppler width of the transitions can be measured in order to determine the velocity distributions in some cases [39].

One of the negative points of REMPI is that it is necessarily a destructive technique; the formation and subsequent detection of ions removes the particles from the detection volume. In the case of LIF, the particles are not lost in the process of detection, and thus for future experiments where retention of the sample is critical, may be of interest.

The main benefit of REMPI for early experiments where detection efficiency is paramount, is that the detection of ions occurs with near unit efficiency. For the case of LIF, photons can be emitted in all directions, not necessarily towards the detector. Since the initial experiment will be attempting to detect very low number densities, REMPI was chosen as the detection technique.

Importantly, the REMPI spectrum of NO is well characterised; indeed, some of the earliest REMPI studies were performed on jet-cooled NO [25]. For the following experiment, (1 + 1) REMPI of NO via the ($A\ ^2\Sigma^+$) state was performed in the region of 226 nm [40] (see figure 2.6).

In the experiment, the dissociation and probe lasers are assumed to have a Gaussian intensity profile [20]. In such a description, the laser beam is 'bounded' by the distance at which the intensity drops to $1/e^2$ (approximately 0.135 of the peak) of that on-axis. This boundary, the beam waist, w, is described in equation 2.19,

$$w^2(x) = w_0^2 \left[1 + \left(\frac{\lambda x}{\pi w_0^2} \right)^2 \right], \tag{2.19}$$

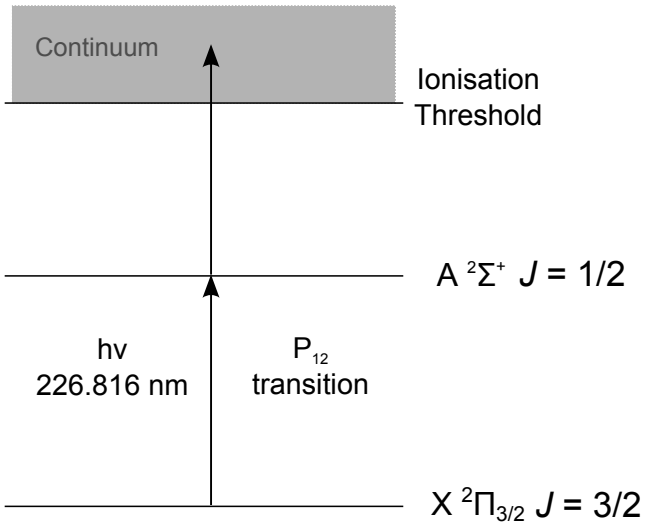

Figure 2.6: Energy level diagram for the (1 + 1) REMPI process used in the experiment.

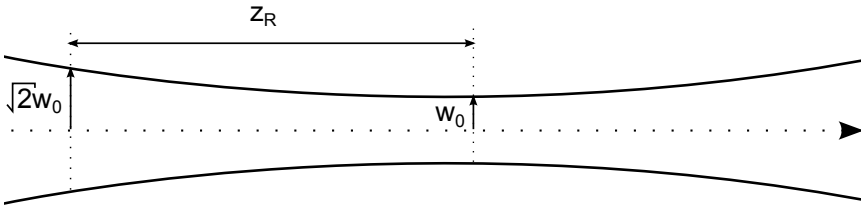

Figure 2.7: Depiction of the focus of a laser beam, showing the definition of the Rayleigh length, x_R.

where w_0 is the waist size at the focal point, λ is the wavelength and x is the displacement from the focus along the laser axis. The collimated region of the beam is defined as the area for which the laser spot is less than $\sqrt{2}\ w_0$ (see figure 2.7). The distance over which this occurs is known as the Rayleigh range, $\pm x_R$, defined in equation 2.20,

$$x_R = \frac{\pi w_0^2}{\lambda}. \tag{2.20}$$

The spot size at the focus of the beam is dependent upon the focal length, of the lens used in the experiment, as seen in equation 2.21:

$$w_0 = \frac{f\lambda}{\pi w_s}, \tag{2.21}$$

where f is the focal length of the lens, and w_s is the spot size at the lens.

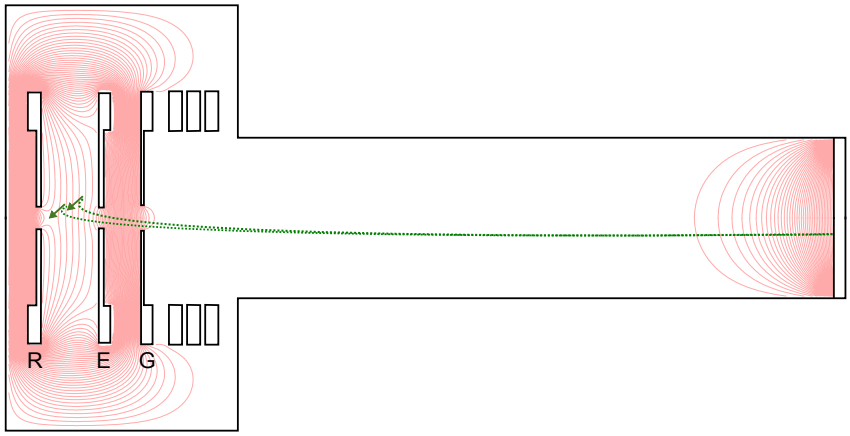

Figure 2.8: Schematic of an Eppink-Parker velocity-map imaging set-up, as used in our experiment, with electric field lines creating velocity-mapping shown. If ions are created with identical velocities (represented by the arrows) but at different points within the electric field, they will still be focussed to the same point on the detector.

Velocity-map imaging

The determination of photofragment velocities is the crucial part of the velocity cancellation experiment for analysis of the temperature distribution of the molecules. Velocity-map imaging was refined in 1997 by Eppink and Parker [11] as an extension of photofragment ion imaging. They discovered that removing the grid from the extractor and ground plates in a standard Wiley-McLaren [41] style ion imaging apparatus, ions created with the same velocity but at different positions would be mapped onto the same point on the detector. This is illustrated in figure 2.8.

The image appears as a 2D compression of the full 3D velocity distribution in which the Newton sphere of velocity vectors is reduced to rings (see figure 2.9). However, the compression of the 3D sphere can complicate matters; extraction of the full 3D velocity distribution from the 2D image is necessary. This can be achieved, by means of mathematical techniques, such as the inverted Abel transformation, as described by equation 2.22, or polar onion peeling methods [42], although these methods assume that the image has a cylindrical axis of symmetry in the plane of the detector.

$$f(r) = -\frac{1}{\pi}\int_r^\infty \frac{dF(y)}{dy}\frac{dy}{\sqrt{y^2 - r^2}}, \tag{2.22}$$

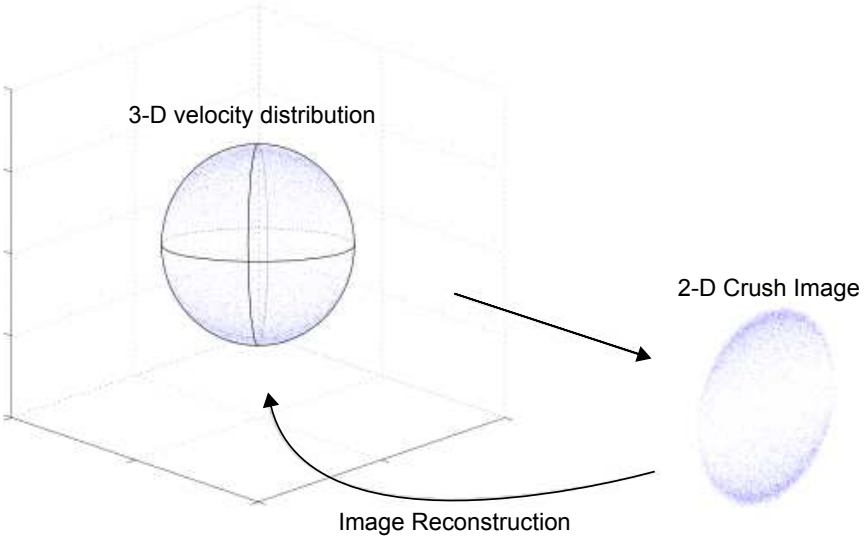

Figure 2.9: Illustration of the full 3D velocity distribution and the 2D crush that is seen on the detector. A mathematical reconstruction technique can be used to regenerate the form of the 3D distribution.

where r is the radial position from the centre of cylindrical symmetry, y is the axial displacement and $F(y)$ is the 2D function with respect to y. For experiments where there is no such axial symmetry, such as those involving aligned fragments [43], more complicated forward convolution techniques or Fourier moment analysis [44] must be applied. The need for any mathematical manipulation can be eliminated by collecting data using slice imaging techniques [45], wherein the several slices through the velocity sphere can be directly imaged using narrow time gating techniques at the detector.

Abel inversion is used to determine an accurate value for the radii of the velocity-map rings, which then calibrates the velocity in any image (see section 2.4.4).

Detection

In order to take advantage of the velocity-map imaging, we need a detection scheme which allows us to visualise the final positions of the ions when they hit our detector. For this we use a matched pair of imaging-quality microchannel plates (MCPs: 40 mm diameter, Kore Ltd.), which amplify the small current of the ions hitting the

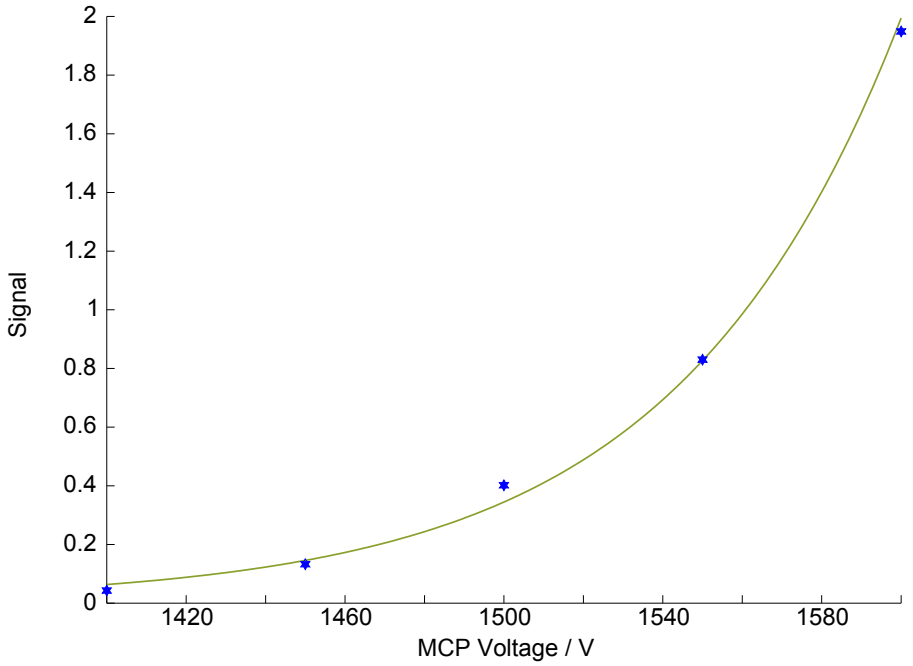

Figure 2.10: Plot of the measured signal level versus MCP voltage (blue stars). The data has been fitted to an exponential growth curve (ochre).

surface of the front plate, by causing a cascade of electrons to shower off towards the rear plate, which in turn creates another electron cascade which flys towards a phosphorescent screen. The electron impact upon the screen causes it to phosphoresce, the light from which can be picked up by a CCD camera.

Since the signal amplification by the MCPs is dependent upon this electron cascade, it follows that the voltage applied to them directly affects the visible signal. Figure 2.10 shows the measured dependence of the detected signal on the voltage applied to the front plate. In this instance, the rear plate is grounded. The fit to the data is an exponential fit – signal $\propto e^{(bV)}$, where V is the applied voltage, and b is a variable determined to be 1.68×10^{-2} V^{-1}. With this factor calculated, it is possible to compare high signal levels, recorded at low MCP voltage, with low level signals that need to be taken at high MCP voltage.

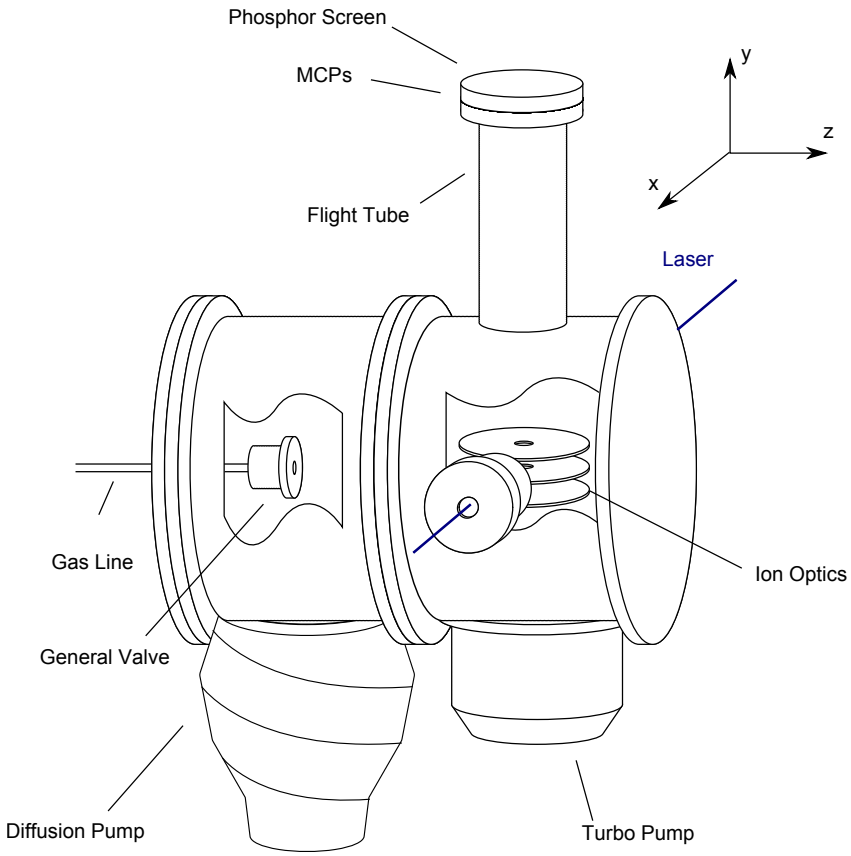

Figure 2.11: Schematic view of the experimental chambers.

2.4.3 NO_2 Experiment

The apparatus used to run the experiment is described below. A schematic of the experimental chamber is shown in figure 2.11, and a more detailed schematic of the ion-optic set-up is shown in figure 2.12. A molecular beam is created through a pulsed (10 Hz repetition rate) supersonic expansion of the gas mixture through a 0.5 mm nozzle, in a source chamber pumped by a diffusion pump to 10^{-7} mbar. The molecular beam passes through a 1 mm diameter skimmer into the main chamber, pumped to 10^{-7} mbar by a rotary-backed turbopump, before being intersected at right-angles by two focused laser beams counter-propagating along the x-axis, generated using tunable dye lasers (Sirah), 121 mm from the nozzle. The gas mixture is created by mixing 1 bar of NO_2 in 5 bar of Xe. Seeding the NO_2 in the heavier Xe reduces the molecular beam velocity, allowing us to dissociate closer to threshold for the photolysis experiment.

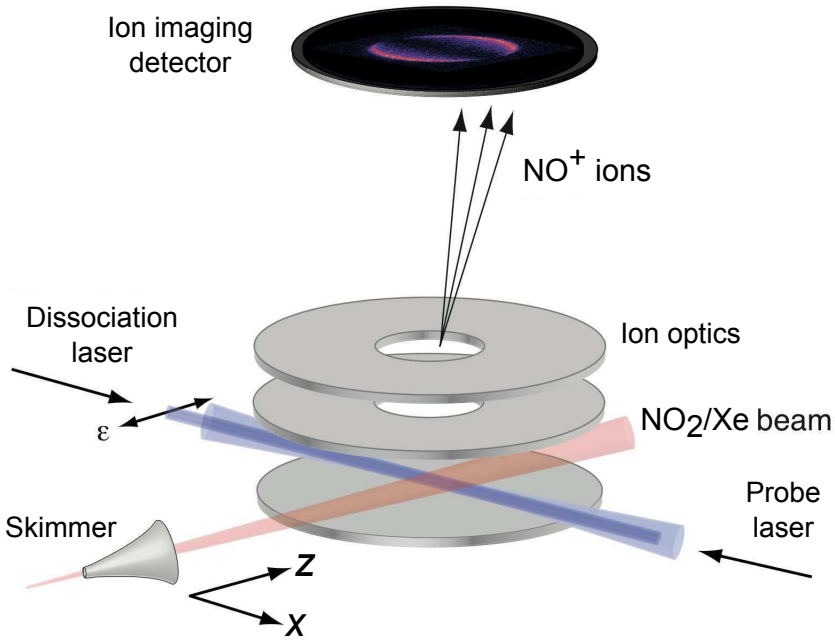

Figure 2.12: Schematic view of the experimental ion optics.

The first laser dissociates the NO_2 molecules in the region 385–392 nm (Nd:YAG 3rd-harmonic pumped dye laser, 1 mJ/pulse) and the second ionises the NO molecules via a (1 + 1) REMPI process on the NO $A\ ^2\Sigma^+\ J\ =\ 1/2 \longleftarrow\ ^2\Pi_{3/2}\ J\ =\ 3/2, P_{12}$ rotational line [40] at 226.816 nm (Nd:YAG 3rd-harmonic pumped dye laser, frequency doubled, 0.15 mJ/pulse). Both lasers are linearly polarised, with the electric vectors, ϵ lying parallel to the molecular beam axis, z. The ions are then velocity-mapped onto an MCP and phosphor screen imaging detector, and the subsequent image is captured by a CCD camera (see Figure 2.12). Note that we are attempting to detect NO molecules in the excited spin-orbit state, X $^2\Pi_{3/2}\ J\ =\ 3/2$ state.

The timing sequence for the experiment has been outlined in figure 2.13. The time referred to as 'delay' throughout the thesis refers to the time between the Q-switch of the dissociation laser and the Q-switch of the probe, i.e. the time between dissociation and ionisation. The sequence of pulses is important; the pulse which triggers the nozzle firing (B) must be set relative to the Q-switch delay of the dissociation laser (C), unlike the other timings which are set relative to the Q-switch of the probe laser (F). This means that the relative delay between gas firing and

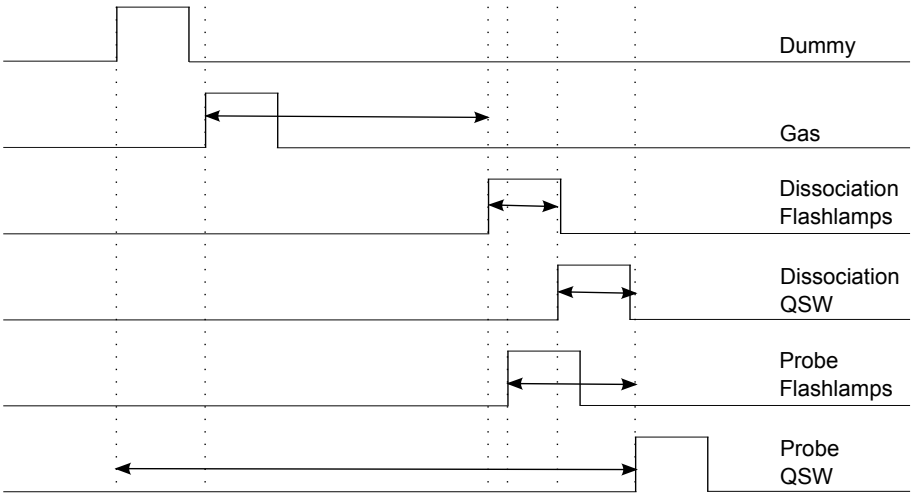

Figure 2.13: Timing sequence for the experiment. The channel letters are used for clarity.

dissociation laser firing remains constant, even whilst the dissociation to ionisation delay increases. The dummy channel (A) is installed so as to be able to program negative timings – for instance, firing the probe laser prior to the dissociation laser.

The delay between the two lasers can cause problems with the signal level, making it acutely sensitive to misalignment, as shown in figure 2.14. The signal should be optimised on the velocity-map image, at a relatively short delay time, e.g. 10-20 μs, so as to ensure we are imaging the zero-velocity ions, and not an artifact of misalignment. To check for such misalignment, it is necessary to maximise signal level, then confirm that the signal decays correctly over the first few microseconds. The signal can be seen to increase in some instances after zero delay if the probe is in the path of the faster moving molecules.

2.4.4 Velocity-map image calibration

Looking back to equation 2.8, we see that the kinetic energy of the fragments depends upon the energy supplied to the system. Notably, in the experiment, we are detecting a single rotational quantum state of NO, the internal energy of the molecule, E_{int}(NO), is fixed. It is this single rotational state that is seen in the velocity-map images. Faster fragments will create larger rings in velocity space,

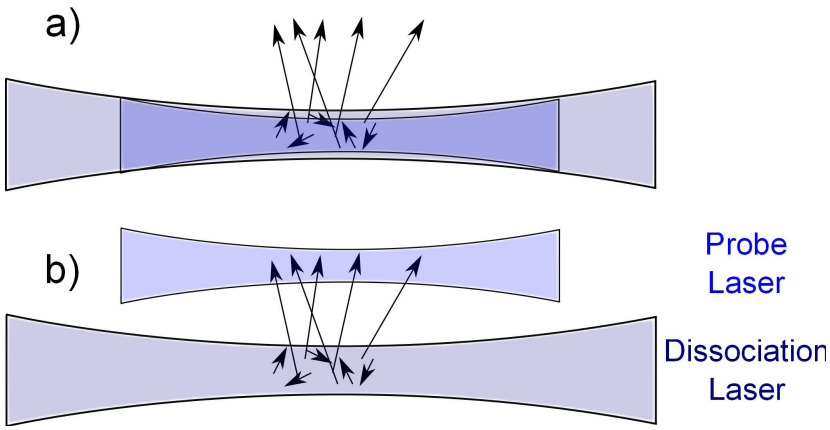

Figure 2.14: The possible effects of laser misalignment upon signal level. The diagrams show what happens if signal optimisation occurs at a short time delay. In a), the two lasers overlap spatially, and during alignment at a short delay, the zero-velocity atoms are ionised. In b), the lasers can be spatially misaligned, yet the signal will appear to be at the same level, should the delay be such that the faster atoms have moved into the probe beam.

Ref	$h\nu$ / cm^{-1}	TKER / cm^{-1}	KE NO / cm^{-1}	v NO / ms^{-1}	pixel radius	ms^{-1} / pixel
a	25411.98	165.51	57.58	214.29	32.55	6.584
b	25456.23	209.64	72.93	241.16	36.66	6.578
c	25546.51	298.54	103.86	287.79	43.88	6.558
d	25608.23	359.70	125.13	315.90	48.20	6.554
e	25664.44	416.61	144.93	339.97	51.82	6.561
f	25731.49	482.18	167.74	365.75	55.83	6.551
g	25828.93	582.27	202.56	401.92	61.19	6.568
h	25940.14	692.83	241.02	438.42	66.79	6.564
i	26107.43	860.51	299.36	488.60	74.42	6.566

Table 2.1: Velocity-space calibration for the NO molecule.

shown in figure 2.15.

Calibration of the velocity-map gives the pixel–to–velocity ratio. Here, one pixel on the velocity-map is equivalent to approximately 6.56 ms^{-1} for an NO^+ ion. This is calculated in table 2.1.

2.4.5 Characterisation of the molecular beam

In the experiment, the molecular beam is travelling perpendicularly to the axis of detection. As a result, velocity-map imaging of the molecular beam itself is possible along both the z- and x-axes (as seen in figure 2.12), from which we will be

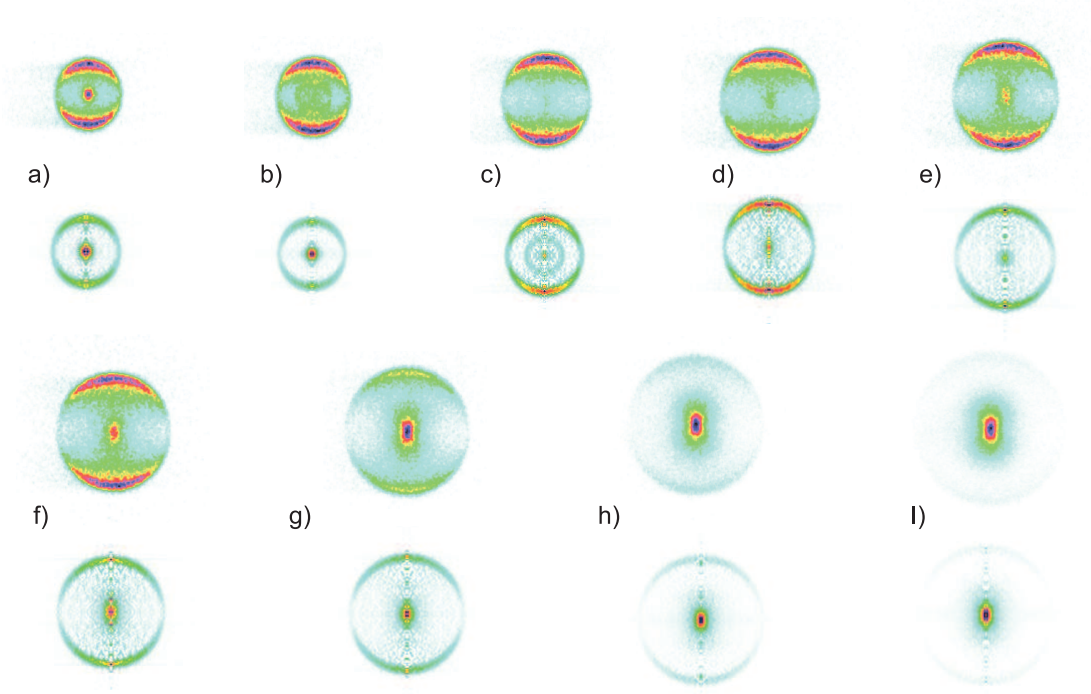

Figure 2.15: Calibration images of NO molecule velocities. Rows 1 and 3 show the 2–D compressed raw velocity-map images, and underneath are shown the relevant slices through Abel Inversion. The relevant calibration data is given in table 2.1, and the letters in the table correspond to the images shown in the diagram.

able to extract both perpendicular and parallel molecular beam temperatures [19]. The velocity distribution of the molecular beam is a critical parameter; the spread of velocities in the molecular beam determines the fraction of the fragments that can be brought to zero-velocity. The velocity distribution can be thought of as a convolution in velocity-space of the COM recoil velocity and the velocity spread of the molecular beam (as described in figure 2.20). The velocity distribution of the molecular beam can be measured using velocity-map imaging of the resonantly ionised NO_2 molecules, and the calibration can be calculated by comparing the mass of the NO_2 to that of the NO:

$$\mathrm{TOF} \propto \sqrt{\frac{m}{qV_\mathrm{R}}}, \tag{2.23}$$

where q is the ion charge, and V_R is the voltage of the repeller plate [11]. The profile of the molecular beam pulse can be determined by recording velocity-map slices

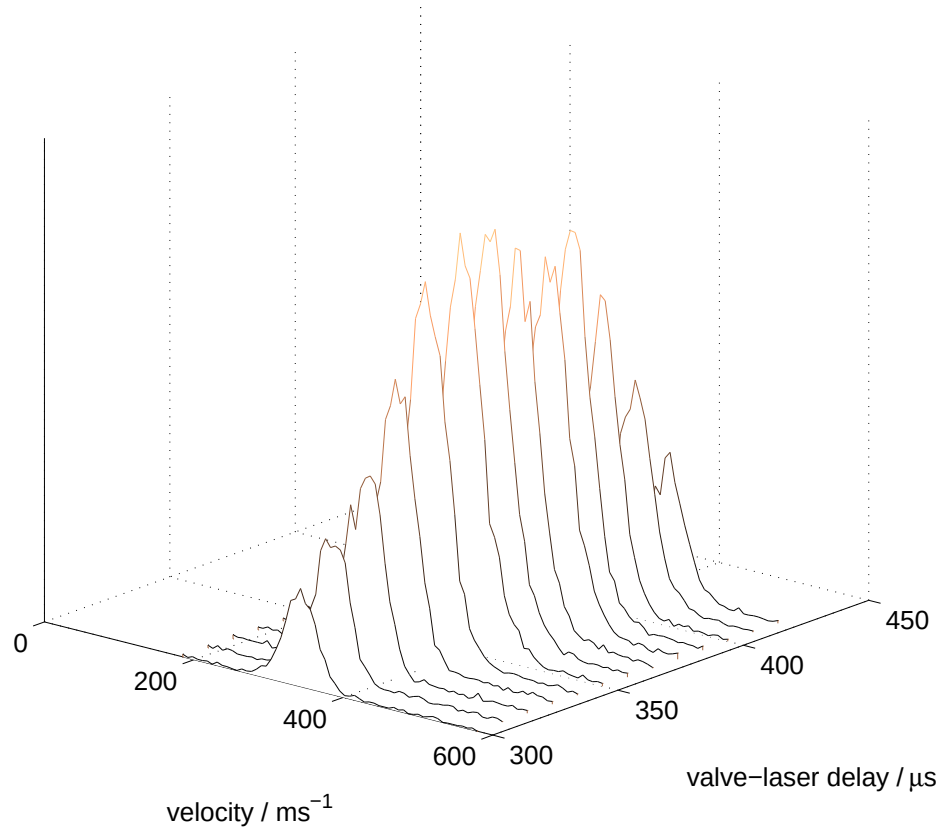

Figure 2.16: Plot of velocities of the NO_2 molecules versus position in the molecular beam, as determined by the time between the nozzle and the laser firing.

through the beam, using the 10 ns long laser pulse to record only a specific velocity portion of the beam.

Figure 2.16 shows how the density and velocity of gas varies through the molecular beam. It is important to know the peak velocity of the molecular beam, since the efficiency of the velocity cancellation process depends upon matching the photodissociation wavelength to cancel the most probable velocity. Figure 2.17 shows the profiles of the 3D plot for clarity.

There are various ways that the molecular beam can be altered in order to best achieve the stopping condition. The composition of the gas in the beam can greatly affect the flow, as described in section 2.2.1. We can alter the carrier gas to change the terminal velocity, or change the relative ratios of the two gases, or change the backing pressure to the valve. In addition, we can change the parameters

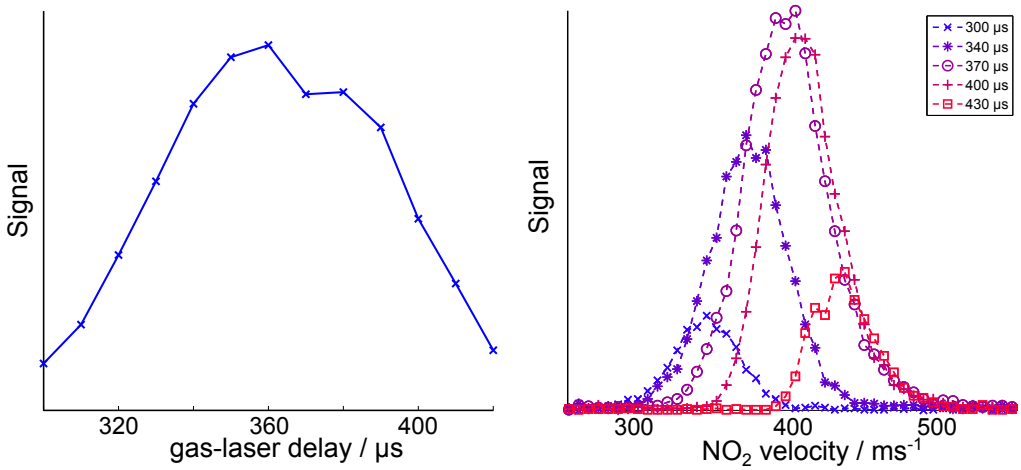

Figure 2.17: Left: Plot of NO_2 intensity as a function of the position through the molecular beam. Right: Plot of velocities of the NO_2 molecules in the molecular beam.

determining the size and shape of the gas pulse. The width of the voltage pulse applied to the solenoid to retract the poppet can be varied; ideally, this would want to be as short as possible, to reduce the possibility of collisions from undissociated molecules or carrier gas with the stopped molecules (see Chapter 5). The tension of the face-plate on the front of the valve can also be adjusted, externally to the experiment. This has a great effect on the shape of the molecular beam pulse, and was therefore optimised during the course of the experiment. The molecular beam shape was analysed with a fast ionisation gauge (FIG), positioned on the molecular beam axis, after the ion optics.

2.4.6 Finding the zero-velocity point

While measuring the diameter of well-characterised rings calibrates the relative velocity-mapping, another method is required to determine the image pixel that corresponds to zero transverse velocity. Using the extraction voltages for velocity-mapping, the main chamber is filled with a low pressure of NO_2 via a leak valve directly connected to the source chamber. This gives a Maxwell–Boltzmann distribution of velocities with a zero-mean (Gaussian spread with a standard deviation, $\sigma = \sqrt{kT/m}$). Ionisation of this gas will produce an image as shown in figure 2.18,

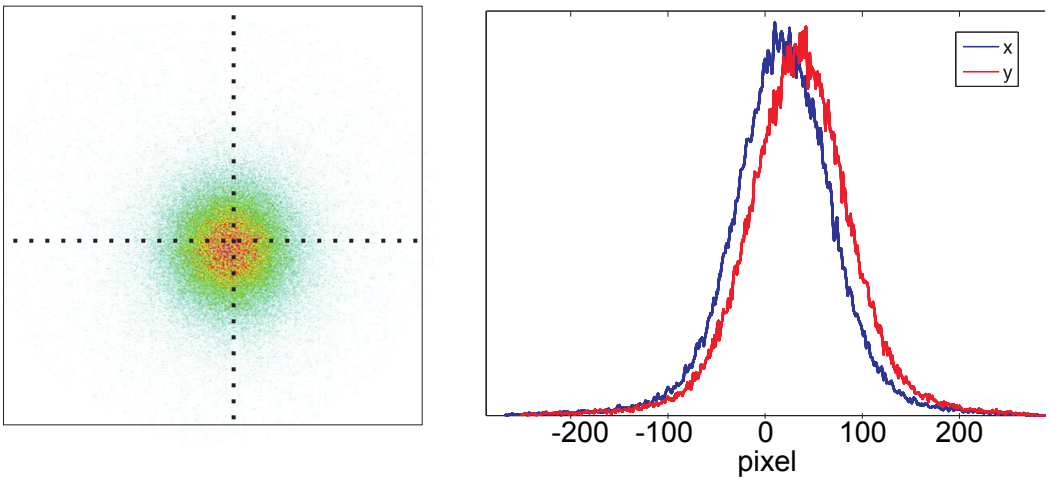

Figure 2.18: Thermal background of NO_2 leaked into the main chamber: velocity-map, left, and plotted Gaussian distributions, right. The Gaussians are shown with their positions relative to the geometric centre of the detection apparatus.

a diffuse blob with its centre at zero velocity. Fitting a Gaussian curve to each of the velocity distributions will yield the zero-velocity point, in pixels, as well as the standard deviation. The offset of the zero-velocity pixel from the geometric centre of the detector is given in table 2.2, and exists due to a minor misalignment between the centre of the CCD camera and the centre of the phosphor screen. Taking the previous velocity calibration and correcting by the ratio of NO to NO_2 masses, the velocity-to-pixel ratio is measured to be 5.30 ms^{-1}/pixel. The standard deviation of a the Gaussian fit to these data is $\sigma = 235$ ms^{-1}. Rearranging the 1D Maxwell-Boltzmann velocity distribution equation gives,

$$f(v) \propto \exp\left(-\frac{m_{\mathrm{NO}} v^2}{k_{\mathrm{B}} T}\right), \tag{2.24}$$

we can extract the temperature:

$$T_{1\mathrm{D}} = \frac{m}{k_{\mathrm{B}}} \sigma_{1\mathrm{D}}^2, \tag{2.25}$$

where 1D represents the fact that this is a measurement along one cartesian axis; this yields a temperature of 320 K, i.e. slightly above room temperature. This shows at the very least, that the velocity-to-pixel calculation is of the correct order

axis	centre / pixels	FWHM / pixels
v_x	18.5	111
v_y	34.9	115

Table 2.2: Zero-velocity point analysed.

of magnitude.

2.4.7 Finding the point of velocity cancellation

Velocity cancellation occurs when the recoil velocity of the NO fragment is equal and opposite to that of the parent NO_2 molecule. The dissociation wavelength required can be expressed using equation 2.26:

$$\lambda_{\text{diss}} = hc \left[\frac{1}{2} \left(\frac{m_{\text{NO}_2} m_{\text{NO}}}{m_{\text{O}}} \right) v_{\text{beam}}^2 + D_0 + E_{\text{int}} \right]^{-1}, \tag{2.26}$$

where v_{beam} is the velocity of the molecular beam. This equation is derived from the rearrangement of equations 2.8 and 2.10. The dissociation process produces one molecule of NO, and one oxygen atom, shown in equation 2.27.

$$\text{NO}_2 + h\nu \rightarrow \text{NO}(v', J') + \text{O}(^3\text{P}_\text{j}), \tag{2.27}$$

where $h\nu$ is the photon energy, v' and J' are the vibrational and rotational levels of the NO molecule and j represents the spin-orbit state of the oxygen atom. Near-threshold dissociation of the NO_2 molecule occurs via the vibrational levels of the $\tilde{\text{A}}\ ^2\text{B}_2$ state. However, there is much nonadiabatic coupling with the higher vibrational levels of the ground state, $\tilde{\text{X}}\ ^2\text{A}_1$. Due to this coupling, the decay of NO_2 into its fragments is a chaotic process and becomes quite complex very near threshold [46]. For the purposes of this experiment, however, the critical factor is that the dissociation anisotropy is highly polarised along the electric field of the laser at the required dissociation energy.

It is helpful to know the rotational temperature of the NO_2, in addition to the

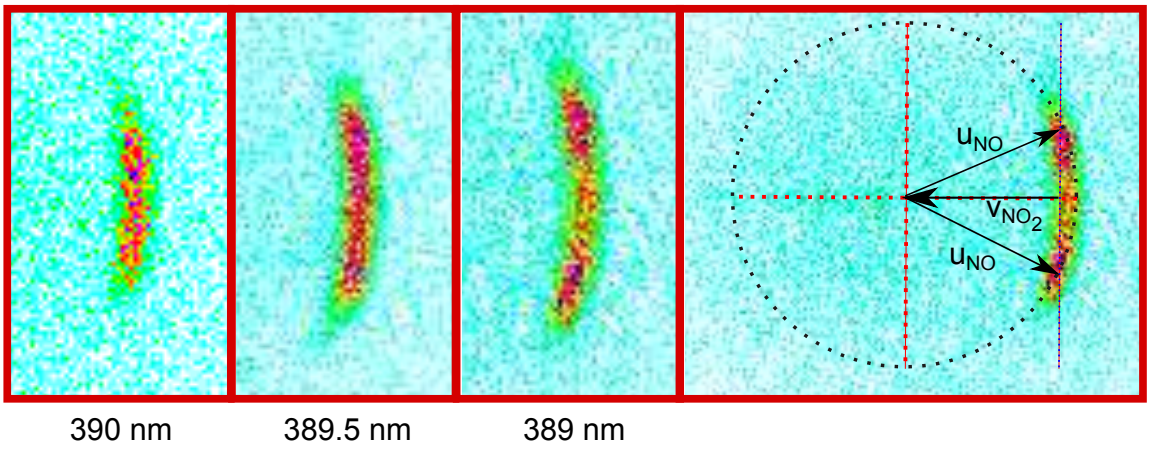

Figure 2.19: Velocity-map images showing the change of transverse velocities of zero v_z atoms with respect to dissociation wavelength, 10 μs after dissociation. On the right-hand side, a Newton diagram descibes how the velocity mismatch generates these 'wings', overlain on the 389 nm case.

fragment rotational distribution. The relative probabilities of dissociation to each of the oxygen spin-orbit states is also necessary. Coupling in the velocity spread of the molecular beam, there are a wide variation of possible recoil velocities for the NO molecule.

Figure 2.19 shows that at a delay of 10 μs, increasing the wavelength of the dissociation laser significantly alters the transverse velocities of the atoms. From left to right, each frame shows the velocity-map image recorded at decreasing dissociation wavelength, and therefore the recoil kinetic energy available is increasing. Thus, in order to match the velocity of the molecular beam along the z-axis, the velocities along the perpendicular axes will have to increase, seen in figure 2.19, (right-hand velocity-map). The dotted line is the $v_z = 0$ line in the laboratory frame. This only intersects with the COM recoil velocity at non-zero perpendicular velocities. On the velocity-map, this manifests as lateral velocity 'wings'. In the experiment, we can vary the dissociation wavelength whilst watching the velocity-map image at a particular delay time to optimise the signal. To get the best signal we want to catch the very crest of the ring, which will lead to perfect velocity cancellation. In practice, it is difficult to obtain a high enough signal level at a long enough delay time to be able to optimise the wavelength in real time. Hence an alternative method of zero-point

determination is needed. An action spectrum can be taken; that is, the dissociation wavelength can be scanned whilst the probe laser wavelength remains positioned on a given REMPI rotational line of NO, and overall signal can be measured, giving some idea of an optimum dissociation wavelength.

2.4.8 Understanding the action spectra

An action spectrum is produced when the dissociation wavelength is scanned for a given probe wavelength, measuring the ionisation signal that remains in the probe volume, at a given pump-probe delay. This will give us some idea of the efficiency of the dissociation process. If make the (erroneous) assumption that all fragments are dissociated such that their velocity vectors point directly back along the molecular beam axis, the problem of velocity cancellation reduces to a purely energetic issue. So, having discounted the angular distribution, what can the action spectrum tell us?

Assuming an infinitely narrow laser linewidth, there is a direct relationship between the photon energy, $h\nu$, and the fragment recoil velocity in the COM frame. For a precursor molecule with a given internal energy, and dissociating to specific product quantum states, the only variable is then the photon energy (see equation 2.8). In this case, *for every photon energy, there is a corresponding fragment recoil velocity.* It is this velocity that can therefore be considered the cancellable velocity; when dissociated with an ideal fragment recoil angle, a precursor molecule moving with the cancellable velocity will yield a fragment with a velocity vector of magnitude zero.

Velocity-map images of the molecular beam can yield the velocity distribution, and from this we can use the same logic to calculate the required photon energies to stop a fragment of each of these molecules. As such, we can convolute the action spectrum with the velocity spread at different gas-laser delays (see figure 2.13, B) in the molecular beam, and get some idea of where the optimum dissociation

wavelength may lie; that is, where the peak density within the molecular beam overlaps with areas of maximum dissociation signal. The 'velocity' spreads seen in figure 2.20 are calculated from velocity-map images of NO_2^+ at various nozzle-laser delay times (see figure 2.13, B), shown in the legend, which have been transformed into required photon energies to plot.

We can see from the convolution that the best strategy for producing zero velocity NO molecules will be to aim for one of the peaks in the action spectrum and therefore try to match the molecular beam to the corresponding velocity. Which peak (here around 389.6 nm), is determined by the molecular beam velocity. Clearly, we want to pick the gas-laser delay that gives the highest convoluted signal, assuming that all of the molecular beam (and implicitly, all velocities at that point in the beam) is capable of creating zero-velocity fragments.

Note that since we are dissociated around 120 mm from the nozzle, the molecules will have had enough time to separate out spatially based on their velocities. As a result, molecules observed at a long nozzle-laser delay time have taken longer to reach the ionization volume, and therefore have a lower mean velocity, requiring a longer wavelength (higher photon energy) to velocity cancel. In other words, the peak distribution, that recorded with a 340 μs nozzle-laser delay, contains the fastest molecules. Subsequent distributuions have a lower mean velocity, and are found later in the molecular beam pulse.

2.4.9 Understanding the rotational distribution

A major drawback of the use of a polyatomic species as a precursor for the Photostop mechanism, is that the fragments can be formed in a multitude of rotational states, and this can lead to dissociation occurring with the correct fragmentation angle, but with an incorrect kinetic energy for velocity cancellation. Essentially, the rotational states act as an energy leech.

Figure 2.21 shows four action spectra taken at different probe wavelengths -

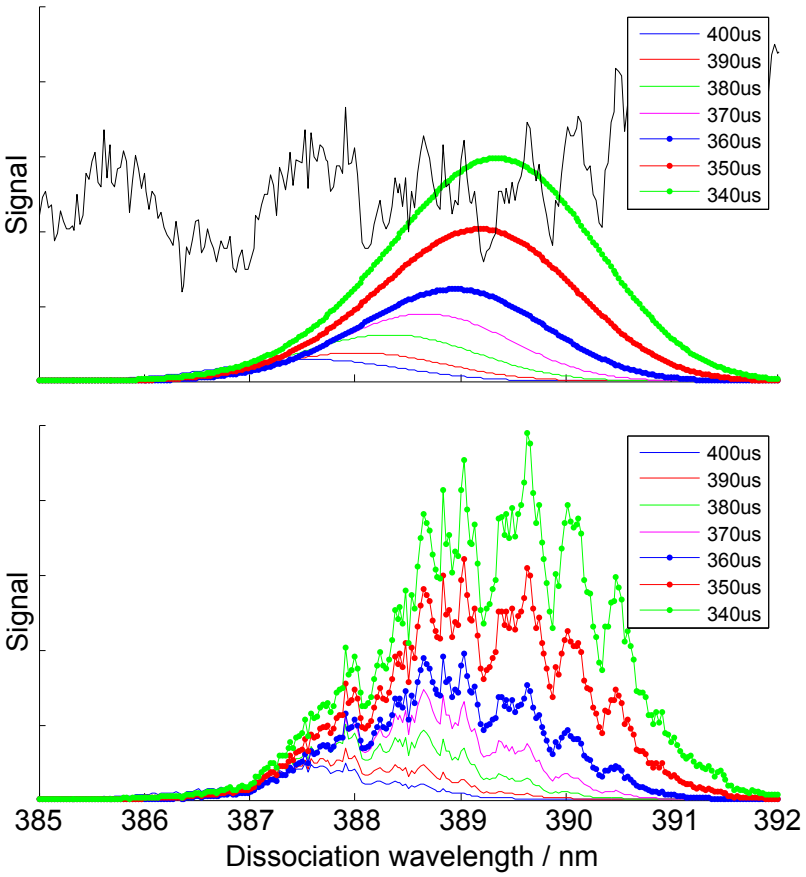

Figure 2.20: Top: action spectrum taken for NO_2 on the NO P_{12} J = 3/2 line at 226.839 nm with the 'velocity' spreads of the molecular beam for different gas-laser delay times. The velocity spreads have been plotted in terms of the dissociation wavelength required to stop an NO molecule. Lower: The convolution of the two, to give optimum velocity cancellation conditions.

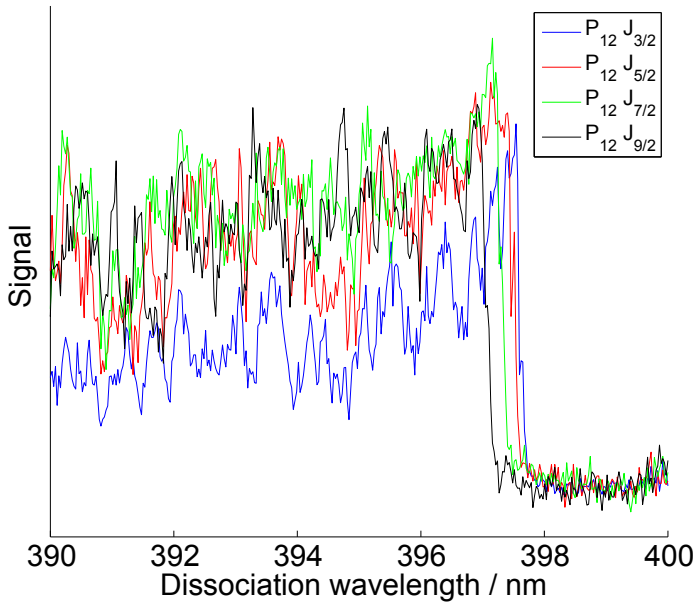

Figure 2.21: Action spectra for four different rotational states of the NO fragment.

226.816, 226.839, 226.860 and 226.877 nm corresponding to the P_{12} lines of the NO molecules at J = 3/2, 5/2, 7/2 and 9/2 respectively. Notably, although the action spectra are broadly similar, there is an overall increase in detected signal at higher rotational states. This suggests that the product state distribution is skewed away from the ground state, although the action spectra are, in reality, a convolution of the rotational population and the line strengths of the transitions. Either way, it is clear that we are not just populating the lowest rotational state of the excited lambda doublet state, $^2\Pi_{3/2}$ of the NO molecule.

Previous studies on NO_2 find that the distribution of rotational states can be reasonably approximated by invoking Phase Space Theory, which calculates the probable final states by considering the conservation of total angular momentum in the dissociation process [47]:

$$\mathbf{j}_{NO_2} = \mathbf{j}_{NO} + \mathbf{j}_{O} + \mathbf{l}, \tag{2.28}$$

where **j** refers to the total angular momentum, and **l** is the orbital angular momentum. For dissociation at 390 nm there is around 500 cm^{-1} of total energy released. Using the rotational constants of NO [48] (see table 2.3), this means that there are around 16 rotational levels available to be populated. This is a large proportion of molecules which will have non-zero velocity, regardless of the direction of fragmentation. The real problem is that the NO_2 molecule is bent in both its ground ($^2A_1$) and excited ($^2B_2$) states, and although it can be photolysed very near to the dissociation threshold, it is predisposed to forming a great number of rotational states post-fragmentation.

Constant	B_e	α_e	D_J
Magnitude/cm^{-1}	1.72016	0.0182	1.023×10^{-5}

Table 2.3: Rotational constants of the (X $^2\Pi_{3/2}$) NO molecule

For this reason, it follows that the most suitable precursors for velocity cancellation using the Photostop technique are diatomic molecules, or highly linear species

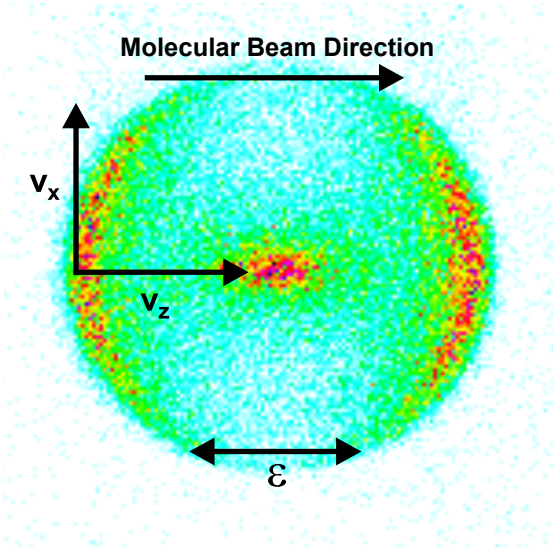

Figure 2.22: A typical velocity-map image taken of NO fragment molecules following NO_2 photodissociation.

which will dissociate in a manner so as to impart as little torque as possible upon the vacating fragment, as is the case for NCNO [49]. Since the products will be atomic or rotationally inactive, there will be no energy leeched into rotational modes.

2.5 Experimental results

The experiment involves the recording of velocity-map images of the type seen in figure 2.22. The molecular beam direction and laser polarisation are shown for clarity. The blob in the centre of this image is residual signal from ionisation of residual NO in the molecular beam, which is centered on the molecular beam velocity – the centre of the ion rings.

2.5.1 NO signal

We need to consider the sources of the NO signal in this experiment. Clearly, the primary contribution is from dissociation of the NO_2 molecules in the molecular beam. However, the longest delay images show a sharp background of NO signal. The source is native NO molecules in the molecular beam, which naturally exist in

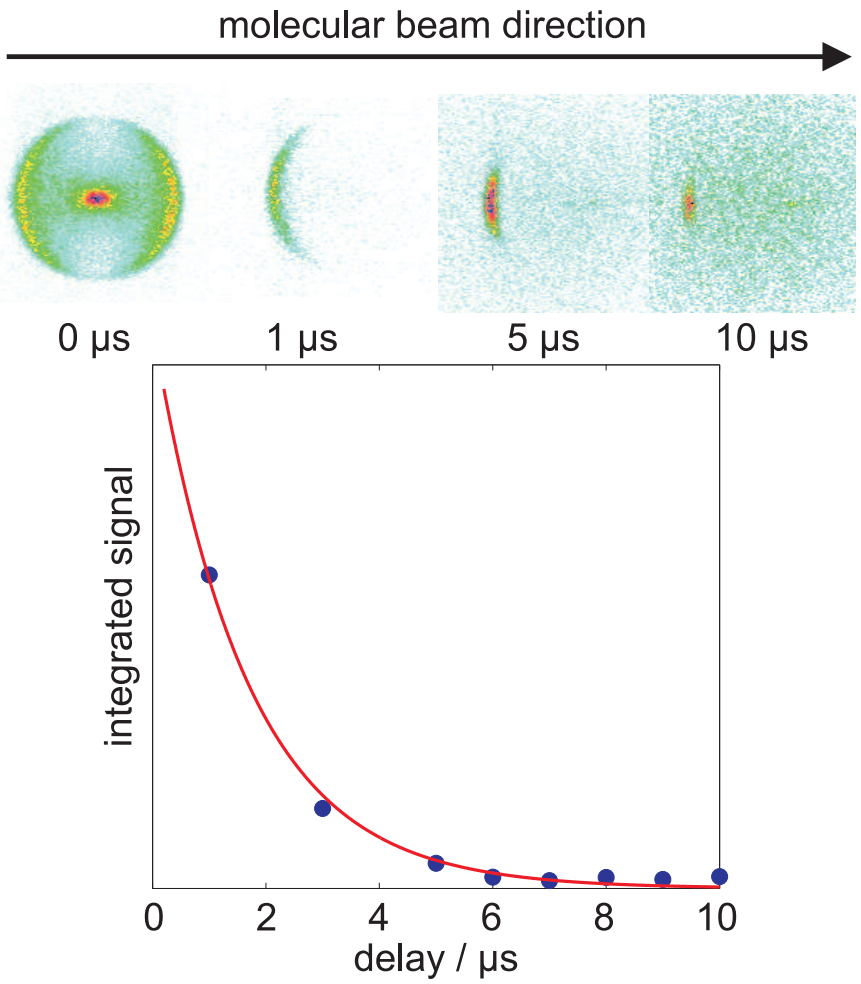

Figure 2.23: Decay of the NO molecule signal, calculated by integration of the signal over the velocity-map images, with respect to delay time, blue points. The velocity-map images at various delays are shown above the figure. The red line is an exponential decay lain over the experimental points.

equilibrium with the pure NO_2 beam. For this reason, the detection is performed using the excited state of the NO. Trottier *et al.* [17] showed that the ratio of native ground state NO ($^2\Pi_{1/2}$) to spin-orbit excited state NO ($^2\Pi_{3/2}$) is 40:1. This ratio reflects the relative populations of the two states at the temperature of the beam (5 K as determined in section 2.2.1). It would be expected that the majority of the molecules will be in the ground state at such a low temperature, since the energy separation of the two states is 119.82 cm^{-3} [50].

A third source of background can be deduced from the experimental images: there is a background ion signal present at longer delay times. This background signal can be easily subtracted, since it appears to be NO ions with a Gaussian velocity distribution, centered around the zero-velocity point. This implies that the signal is a result of residual NO molecules in the main chamber which have not yet been pumped away after the previous shot.

2.5.2 Results

The Photostop technique as a method of cold molecule creation has already been verified most successfully by Trottier and co-workers [17], showing that the NO molecules remained after velocity cancellation for at least 10 μs after dissociation. The aim of the experiments reported here is to replicate this in order to optimise the apparatus on a well-characterised system, before implementing velocity cancellation with other species. Figure 2.23 shows the velocity-map images for a few of the pump-probe time delays used in the experiment. We can see the integrated fragment ion signal decays exponentially with respect to time. This decay results from the fastest atoms vacating the ionisation region, i.e. those moving from left to right in the ion images over the course of the first microsecond or so. The atoms with a high transverse velocity, v_x (vertical axis in the velocity-maps) will be next to vacate the ionisation region, leaving only a small proportion of the initial photofragments in velocity- and real-space. After 10 μs, we can fit the measured velocities to a

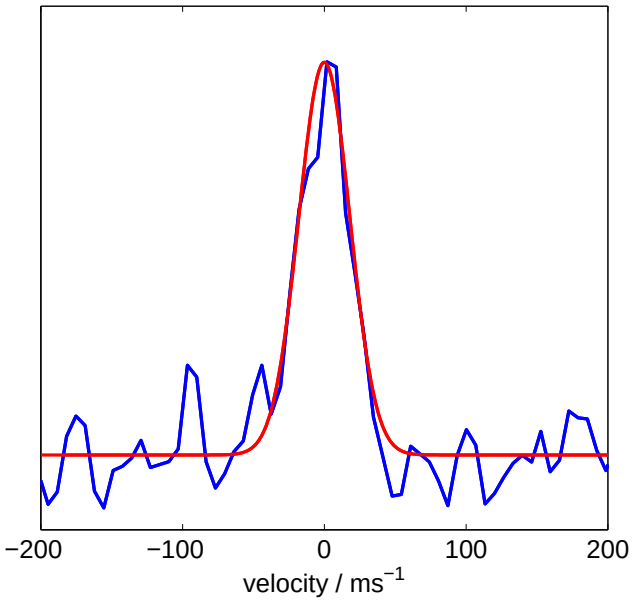

Figure 2.24: A profile of the near-zero-velocity NO after 10μs, blue, and a Gaussian fit to it, red. This can give us the molecular beam axis velocity, v_z, and therefore a temperature.

Gaussian distribution, and determine a sample temperature using equation 2.25.

The sample is visibly colder along the molecular beam axis, z, since there is a stricter velocity-component selection for this axis, set by the aspect ratio of the probe laser volume. The propagation direction of the probe laser is along x, and thus atoms moving with larger v_x can be seen for longer, remaining within the Rayleigh length of the laser beam (see section 2.4.2, and thus can still be ionised along the laser axis. The z-axis velocity coincides with the radial direction of the laser beam; faster atoms can move out of the focus, as described by the laser waist radius, w (equation 2.19) much more quickly if they have a higher v_z component. As such, v_z gives the best indication of the likely sample temperature which we can expect, since anything but the very slowest molecules will depart out of the laser focus very quickly along the z-axis, we see the likely attainable velocity distributions. Figure 2.24 shows the v_z distribution for the ions in the probe volume after 10 μs, and a Gaussian fit. It can be seen that the velocity distribution is very narrow, measured here as $\sigma_z = 18$ ms^{-1}. Using equation 2.25 for a 1D velocity distribution, we

arrive at a sample temperature after 10 μs of $T_z = 1.17$ K. This can be reduced to the sub-Kelvin regime, by selecting out the very core of this velocity distribution, either through experimental improvements, such as using a more favourable precursor species (explored in chapter 3), or otherwise confining only the very slowest molecules (explored in chapters 4 & 5).

If we have created cold molecules which are stationary in the lab-frame, then why are we only able to see them for up to 10 μs after dissociation? The molecules will be visible until they have vacated the laser focal volume. After they have left, no matter how slow they are, we will not be able to observe them. The problem with the technique as it stands is that there are too few molecules remaining at long enough delays to be seen. This is because we are not producing enough molecules at zero-velocity. The problem of stopping a molecular fragment lies in the spread of the internal energy throughout its rotational modes, thus leaving a range of kinetic energies available to the molecule. This limits the effectiveness of the velocity cancellation technique for the molecular case.

2.6 Identifying species suitable for velocity cancellation

How do we go about identifying species which are suitable for producing cold samples via the Photostop technique? Clearly there are several important factors to consider. The first and foremost is that the fragment in question is one of chemical interest. The precursor species needs to have as narrow a velocity distribution as possible, which is achieved here using the cooling provided by the supersonic expansion. The velocity spread is proportional to the total velocity however, ie. a faster beam will have a greater velocity spread. As a result, we want to use a slow molecular beam, which can be achieved by seeding the species in a heavy rare gas, such as Xe (mass = 131 atomic units). To cancel this velocity, we need to photolyse the molecule closer

to the dissociation threshold, so as to limit the amount of energy available to the fragments. Ideally, the energy available to the fragments would all be transferred into kinetic energy, with no avenues for loss into rotational, vibrational or electronic excitations. The most direct way to prevent channels leading to rotationally or vibrationally excited species is to dissociate a diatomic molecule into two atomic fragments. The technique would, from this regard, appear to be better suited to the creation of cold atoms, rather than molecules.

Finally, we need to dissociate using states with a favourable anisotropy parameter, β, as described by equation 2.12. Various precursors and their dissociation dynamics were considered – oxygen from NO [51] or CO [52], NH_2 from NH_3 [53] or Cl from BrCl [54]. It was decided however, that, although dissociation with a light atom departing removed a large proportion of the kinetic energy from dissociation, based on the mass ratios outlined in equation 2.10, using a homonuclear diatomic molecule would double the number of atoms available to be brought to zero-velocity. By using a heteronuclear species, it is possible that only 50% of the fragment atoms recoiling with the correct fragmentation angle could possibly undergo velocity cancellation, due to an unfavourable molecular orientation. The excess kinetic energy released by the dissociation can be offset by changing the dissociation wavelength or the carrier gas. Both Cl_2 [55] and Br_2 [56] offered reasonable channels for velocity cancellation, and Br_2 was eventually chosen on grounds of experimental simplicity; the bromine is less corrosive to the experimental apparatus, and less toxic to humans than chlorine.

2.7 Outlook

As previously shown [17], the Photostop technique is a viable and highly attractive technique for the production of zero-velocity molecules in the lab-frame; velocity cancellation via photolysis is a simple yet effective method. The mechanism of photodissociation is well-understood and has been extensively studied for many

years.

By extending this technique, we can increase the number of species for which we can study cold chemical reactions. From the velocity calibration of the NO images, it ought to be possible to at the very least to produce cold samples down to 1.17 K. In the case of atomic species, the problem of product rotational and vibrational states acting as avenues of loss for kinetic energy cancelling is removed. Further experiments can therefore be carried out on other species to attempt to improve its efficiency.

Bibliography

[1] J. J. Gilijamse, S. Hoekstra, N. Vanhaecke, S. van de Meerakker, and G. Meijer, Eur. Phys. J. D **57**, 33 (2010).

[2] E. L. Raab, M. Prentiss, A. Cable, S. Chu, and D. E. Pritchard, Phys. Rev. Lett. **59**, 2631 (1987).

[3] M. S. Elioff, J. J. Valentini, and D. W. Chandler, Science **302**, 1940 (2003).

[4] D. J. Hollenbach and A. G. G. M. Tielens, Rev. Mod. Phys. **71**, 173 (1999).

[5] R. P. Wayne, J. Geophys. Research. - Planets **98**, 13119 (1993).

[6] J. Lelieveld, F. J. Dentener, W. Peters, and M. C. Krol, Atm. Chem. and Phys. **4**, 2337 (2004).

[7] R. L. Miller, A. G. Suits, P. L. Houston, R. Toumi, J. A. Mack, and A. M. Wodtke, Science **265**, 1831 (1994).

[8] H. H. Holmes and F. Daniels, J. Am. Chem. Soc. **56**, 630 (1934).

[9] G. P. Morley, I. R. Lambert, M. N. R. Ashfold, K. N. Rosser, and C. M. Western, J. Chem. Phys. **97**, 3157 (992).

[10] D. H. Mordaunt, M. N. R. Ashfold, R. N. Dixon, P. Loffler, L. Schnieder, and K. H. Welge, J. Chem. Phys. **108**, 519 (1998).

[11] A. T. J. B. Eppink and D. H. Parker, Rev. Sci. Instr. **68**, 3477 (1997).

[12] M. Brouard, E. K. Campbell, A. J. Johnsen, C. Vallance, W. H. Yuen, and A. Nomerotski, Rev. Sci. Instr. **79**, 123115 (2008).

[13] E. S. Wilman, S. H. Gardiner, A. Nomerotski, R. Turchetta, M. Brouard, and C. Vallance, Rev. Sci. Instr. **83**, 013304 (2012).

[14] W. G. Doherty, Master's thesis, Oxford University (2008).

[15] S. J. Matthews, S. Willitsch, and T. P. Softley, Phys. Chem. Chem. Phys. **9**, 5656 (2007).

[16] B. S. Zhao, S. E. Shin, S. T. Park, X. Sun, and D. S. Chung, J. Phys. Soc. Japan **78**, 094302 (2009).

[17] A. Trottier, E. Wrede, and D. Carty, Mol. Phys. **105**, 725 (2010).

[18] A. A. Passchier, J. D. Christian, and N. W. Gregory, J. Phys. Chem. **71**, 937 (1967).

[19] G. Scoles, *Atomic and Molecular Beam Methods* (OUP, New York, 1988).

[20] W. Demtröder, *Laser Spectroscopy : Basic Concepts and Instrumentation* (Springer, 1996), second enlarged ed.

[21] R. E. Smalley, L. Wharton, and D. H. Levy, Accounts of Chemical Research **10**, 139 (1977).

[22] C. M. Western, *PGOPHER, a Program for Simulating Rotational Structure*, university of Bristol, URL `http://pgopher.chm.bris.ac.uk`.

[23] R. Zare and D. Herschbach, Proc. IEEE **51**, 173 (1963).

[24] R. N. Zare, *Angular Momentum* (Wiley, New York, 1988).

[25] J. C. Miller and R. N. Compton, J. Chem. Phys. **84**, 675 (1986).

[26] J. Garthwaite and C. J. Boulton, Ann. Rev. Physiology **57**, 683 (1995).

[27] I. Goldstein, T. Lue, H. Padma-Nathan, R. Rosen, W. Steers, P. Wicker, and S. S. Grp, N. Eng. J. Med. **338**, 1397 (1998).

[28] J. MacMicking, Q. Xie, and C. Nathan, Ann. Rev. Immun. **15**, 323 (1997).

[29] D. M. Leahey and M. C. Hansen, Atmos. Environ. A **24**, 2533 (1990).

[30] O. L. A. Monti, H. Dickinson, S. R. Mackenzie, and T. P. Softley, J. Chem. Phys. **112**, 3699 (2000).

[31] S. Jung, E. Tiemann, and C. Lisdat, Phys. Rev. A **74**, 040701 (2006).

[32] O. Bucicov, M. Nowak, S. Jung, G. Meijer, E. Tiemann, and C. Lisdat, Eur. Phys. J. D **46**, 463 (2008).

[33] R. Jost, J. Nygård, A. Pasinski, and A. Delon, J. Chem. Phys. **105**, 1287 (1996).

[34] D. C. Robie, M. Hunter, J. L. Bates, and H. Reisler, Chem. Phys. Lett. **193**, 413 (1992).

[35] A. V. Demyanenko, V. Dribinski, H. Reisler, H. Meyer, and C. X. W. Qian, J. Chem. Phys. **111**, 7383 (1999).

[36] S. J. Matthews, Ph.D. thesis, Oxford University (2007).

[37] C. Jonah, J. Chem. Phys. **55**, 1915 (1971).

[38] D. W. Chandler and P. L. Houston, J. Chem. Phys. **87**, 1445 (1987).

[39] K. Bergmann, W. Demtröder, and P. Hering, Appl. Phys. A **8**, 65 (1975).

[40] G. Herzberg, *Spectra of diatomic molecules* (Litton Educational Publishing Inc., 1950), 2nd ed.

[41] W. C. Wiley and I. H. McLaren, Rev. Sci. Instr. **26**, 1150 (1955).

[42] G. M. Roberts, J. L. Nixon, J. Lecointre, E. Wrede, and J. R. R. Verlet, Rev. Sci. Instr. **80**, 053104 (2009).

[43] A. S. Bracker, E. R. Wouters, A. G. Suits, and O. S. Vasyutinskii, J. Chem. Phys. **110**, 6749 (1999).

[44] M. J. Bass, M. Brouard, A. P. Clark, and C. Vallance, J. Chem. Phys. **117**, 8723 (2002).

[45] C. R. Gebhardt, T. P. Rakitzis, P. C. Samartzis, V. Ladopoulos, and T. N. Kitsopoulos, Rev. Sci. Instr. **72**, 3848 (2001).

[46] A. Delon, F. Reiche, B. Abel, S. Y. Grebenshchikov, and R. Schinke, J. Phys. Chem. A **104**, 10374 (2000).

[47] M. Hunter, S. A. Reid, D. C. Robie, and H. Reisler, J. Chem. Phys. **99**, 1093 (1993).

[48] J. E. Sansonetti and W. C. Martin, J. Phys. Chem. Ref. Data **34**, 1559 (2005).

[49] I. Nadler, H. Reisler, M. Noble, and C. Wittig, Chem. Phys. Lett. **108**, 115 (1984).

[50] J. W. C. Johns, J. Reid, and D. W. Lepard, J. Mol. Spectr. **65**, 155 (1977).

[51] B. L. G. Bakker, A. T. J. B. Eppink, D. H. Parker, M. L. Costen, G. Hancock, and G. A. D. Ritchie, Chem. Phys. Lett. **283**, 319 (1998).

[52] B. L. G. Bakker and D. H. Parker, Chem. Phys. Lett. **330**, 293 (2000).

[53] D. H. Mordaunt, M. N. R. Ashfold, and R. N. Dixon, J. Chem. Phys. **104**, 6460 (1996).

[54] M. Beckert, E. R. Wouters, M. N. R. Ashfold, and E. Wrede, J. Chem. Phys. **119**, 9576 (2003).

[55] P. C. Samartzis, B. L. G. Bakker, T. P. Rakitzis, D. H. Parker, and T. N. Kitsopoulos, J. Chem. Phys. **110**, 5201 (1999).

[56] P. C. Samartzis, T. N. Kitsopoulos, and M. N. R. Ashfold, Phys. Chem. Chem. Phys. **2**, 453 (2000).

Chapter 3

Production of cold bromine atoms

Bromine is an interesting molecule to choose as a precursor for velocity cancellation experiments. To date, cold atom production has been mostly focussed around the left hand edge of the periodic table. Hydrogen atoms have been cooled by various methods, such as Zeeman deceleration [1, 2] or evaporative cooling [3]. All of the alkali metals have been reduced to sub-Kelvin temperatures [4–9], and chemistry has been observed with cold alkaline earths [10]. An obvious route to observing chemical behaviour at low temperatures would be to match up these electron-donating species with electron accepting species from the right hand side of the periodic table: for instance, the halogen atoms. The alkali metals famously react with the halogens under ordinary conditions, making a variety of salts, such as: NaCl, used widely as a flavouring and preservative; LiBr, previously used as a sedative; KCl, used in the manufacture of fertilizers, not to mention the lethal injection; LiF, widely used in optics due to its transparency in the short wavelength UV region; and CsCl, used extensively as a radioisotope in the medical sciences.

Some of the most successful work in the field of ultracold molecules has arisen from the creation of ultracold dipolar molecules, such as KRb [11]. Replacement of one of the alkali atoms with an atom such as chlorine, would create a molecule with a much greater electric dipole moment, and would be very interesting for the study of dipole-dipole interactions.

There has been some limited exploration of the rest of the periodic table: elements in both the d-block [12] and f-block [13] have been buffer-gas cooled. However, it is in the elusive p-block that cold chemistry may begin to become more interesting. As yet, the p-block elements have not been cooled to ultracold temperatures. There has been interest in exploring options for laser cooling gallium [14, 15], but the halogen atoms lack accessible routes to perform laser cooling (see section 1.3). A novel technique to create cold halogen atoms would therefore be quite welcome.

3.1 Molecular Br_2

Molecular bromine appears to be a good precursor for producing cold bromine atoms via the Photostop technique. Dissociation of the molecule has been extensively studied [16, 17]. In its ground state, molecular bromine (X $^1\Sigma_g$ (0_g)) absorbs light over the range 320 to 600 nm [18]. This broad absorption band covers three separate excitations: $A\ ^3\Pi_u(1_u), B\ ^3\Pi_u(0_u^+)$, and $C\ ^1\Pi_u(1_u) \longleftarrow$ X, each peaking at around 400, 490 and 550 nm respectively. The notation for the bromine molecule arises from the strong spin-orbit coupling in the Hund's case (c) limit (term symbol $^{2\Sigma+1}\Lambda_\Omega$), where Ω (the projection of the spin-orbit coupling onto the molecular axis), is a good quantum number, but Σ (spin projection) and Λ (orbital angular momentum projection) are not [19].

At long internuclear separation, the ground state potential rises to the dissociative limit, leaving two ground state ($^2P_{3/2}$) bromine atoms [20]; this is the first dissociation limit, $D_0 = 15890\ cm^{-1}$. Above this threshold, there are higher dissociation limits, leading to one ground state and one excited state atom (Br ($^2P_{3/2}$) + Br* ($^2P_{1/2}$)) above the second dissociation limit, and two excited state atoms from the third dissociation limit. The energy of each limit increases by the spin-orbit splitting of the bromine atom ($3685.24\ cm^{-1}$ [21]), and subsequently the threshold wavelengths for one photon dissociation are 629.0, 510.6 and 429.8 nm respectively.

The near-threshold dissociation of Br_2 near to the second dissociation limit is

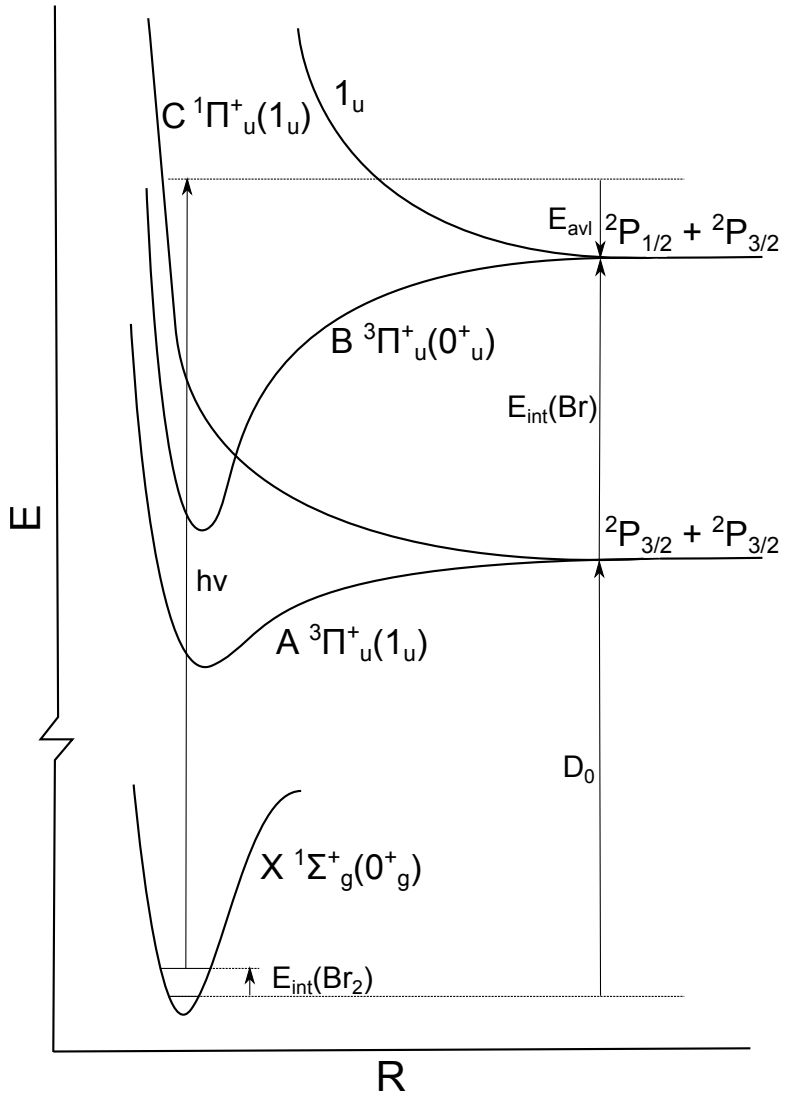

Figure 3.1: Depiction of the energy level diagram for bromine. We excite just above the second dissociation threshold to try and access the favourable recoil dynamics arising from parallel dissociation from the B state, leading to Br + Br*.

fascinating because of the interplay between two of the three excited states of the molecule. In the region around the 450-500 nm dissociation wavelength, the tails of the B and C state absorptions will overlap. Since there is a real curve crossing in this region, dissociation occur adiabatically on either surface competitively, leading to the two product channels. In figure 3.1, we can see a schematic of the energy levels. Dissociation occurs above the second dissociation threshold, at 19580 cm^{-1}, and products can be formed as either pair of products, Br + Br or Br + Br*. An important factor to note, then, is the branching ratio to either product state, given

by equation 3.1.

$$\phi(\mathrm{Br} + \mathrm{Br}^*) = \frac{[\mathrm{Br} + \mathrm{Br}^*]}{[\mathrm{Br} + \mathrm{Br}^*] + [\mathrm{Br} + \mathrm{Br}]} \tag{3.1}$$

Cooper *et al.* [17] studied the photolysis of Br_2 in the wavelength region of 260–580 nm, and have mapped out the branching ratio over the region of 360–500 nm. At very high photon energies, $\lambda < 430$ nm, the dissociation occurs to give solely ground state bromine atom fragments, attributed to direct dissociation from the C state, a purely repulsive potential. Closer to the dissociation threshold, there is some mixing between this state and the attractive B state potential, which dissociates directly to $\mathrm{Br} + \mathrm{Br}^*$. The closer to threshold one gets, the higher the probability of dissociation via the B state, and the higher the branching ratio. The highest branching ratio (approximately 0.8) occurs at wavelengths from around 480 nm, until the second dissociation threshold at 510.6 nm. As the $\mathrm{Br} + \mathrm{Br}^*$ channel gives fragments of the right energy for velocity cancellation, dissociation in this wavelength region will give the optimum number of atoms centered at zero velocity.

3.1.1 Alternative channels

We have specifically chosen the dissociation wavelength to use in the experiment, to attempt to maximise the number of stopped atoms generated. However, molecular bromine absorbs light much more readily in the wavelength region below 430 nm, so why do we not dissociate in this region?

The greater photon energy supplied to the system means that we will be unable to velocity cancel the atoms dissociated via the C state, since the velocities involved will be much greater than those available to a molecular beam, without seeding in helium. Seeding in helium would give us the opportunity to velocity cancel, but as the recoil velocity increases, the fraction of atoms that would adequately velocity cancel, i.e. those with a residual velocity below a given threshold, decreases. In addition, the C state gives fragments with a perpendicular dissociation pattern, requiring a change in experimental configuration to velocity cancel initially. From a $0_g \rightarrow 0_u$ parallel

transition, the expected product angular distribution can be characterised by a β parameter of +2, whereas for the $0_g \rightarrow 1_u$ transition, a β parameter of -1 is presumed. This implies that when imaging the rings from dissociation, the fragments from the two states should appear different not only in terms of kinetic energy release (and therefore radius), but also in fragmentation direction. The innermost ring will appear to have dissociated along the molecular beam axis, and the outer ring will appear larger, and rotated by 90°.

3.1.2 Isotope abundance

There are only two stable isotopes of atomic bromine, which exist in a near 50–50 ratio naturally. ^{79}Br and ^{81}Br are separated by two atomic mass units, and as a result, we see that there are differences in the recoil velocities. In the molecular beam, the Br_2 molecules have a 1:2:1 ratio of the isotopomers: $^{158}Br_2$, $^{160}Br_2$ and $^{162}Br_2$. The relative kinetic energies of each isotope are related by equation 3.2,

$$E_{\text{kin}}^{\text{Br}^{\text{A}}} = \frac{m_{\text{Br}^{\text{B}}}}{m_{\text{Br}^{\text{A}}} + m_{\text{Br}^{\text{B}}}} . E_{\text{kin}}^{\text{Br}_2^{\text{AB}}}, \tag{3.2}$$

so we see a spread of recoil velocities. For instance, for dissociation at 20570 cm^{-1}, $^{158}Br_2$ yields two ^{79}Br at 388.2 ms^{-1}, $^{160}Br_2$ gives a ^{79}Br atom at 390.4 ms^{-1} and one ^{81}Br atom at 380.7 ms^{-1}, whilst the $^{162}Br_2$ molecule produces two ^{81}Br atoms at 382.9 ms^{-1}. This analysis takes into account the slightly different dissociation thresholds for each of the states: $D_0 = 15890$ cm^{-1}, 15891 cm^{-1}, 15892 cm^{-1} [22] for the $^{158}Br_2$, $^{160}Br_2$ and $^{162}Br_2$ molecules respectively. Ideally, we would want to use an isotopically pure sample of bromine. In practice, pure Br_2 is not commercially available, and in reality, the mass has little effect upon the final velocity distribution. The velocity spread arising from the isotopes, is smaller than the velocity spread of the molecular beam, so all recoil velocities can indeed be cancelled.

The isotope abundance can be experimentally verified by using a TOF detection scheme; the REMPI laser was positioned at 263.007 nm to create Br_2^+ [23], though

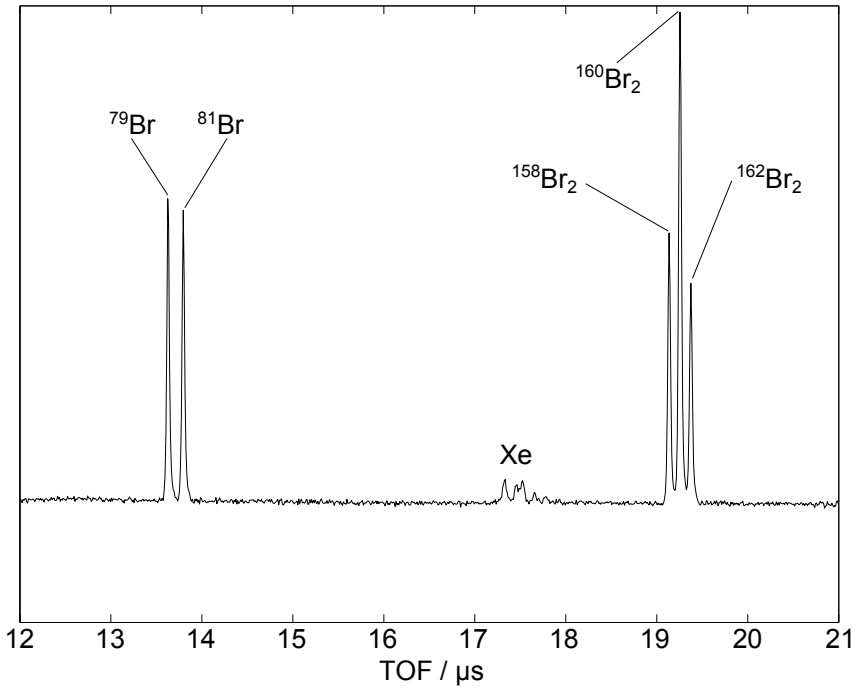

Figure 3.2: A time-of-flight mass spectrum for ionisation on the Br_2^+ REMPI line, showing the different isotopes of Br around TOF = 13.8 μs, and the different isotopomers of Br_2 around TOF = 19.3 μs. The signal around TOF = 17.5 μs is residual Xe from the NO_2 experiment.

some one-colour dissociation giving Br^+ ions was also observed. The arrival times of the ions could be seen on the detector, in accordance with their mass ratios, as seen in figure 3.2. Attempts to gate by mass on the detector by pulsing the voltage on the MCPs during the experiment to improve the signal-to-background ratio, proved fruitless. The gating for some reason reduced the absolute visible signal level by around an order of magnitude. This presumably was due to the pulsing unit not providing an adequate pulse to the MCPs to be able to detect ions, and as such, the gating was not used in later experiments.

3.2 Experimental set-up

The experiment is a traditional photodissociation apparatus with the imaging plates positioned perpendicular to the plane of the molecular beam as described in section 2.4.3. A mixture of approximately 10 % Br_2 in Kr is allowed to equilibrate in

a mixing cylinder with heated arms aiding convection mixing. Bromine exists as a liquid at room temperature, and was stored in a sealed vial on the gas line. The vapour pressure of the liquid is negligible at -78 °C, so by placing a dry ice/acetone bath around the vial and then pumping on the gas line, we are able to remove any air in the system. The uncooled portion of the gas line was then heated with a heat gun, to attempt to vapourise any water adsorbed onto the surface of the pipework. Any reaction between water and bromine leads to HBr, which is corrosive to the metal of the gas line. The vial is then allowed to return to room temperature, where the vapour pressure is approximately 0.3 atm. A carrier gas can then be added to the mixture. The molecular beam itself is formed by a 10 Hz pulsed supersonic expansion through a 0.5 mm diameter nozzle, followed by a 1 mm skimmer. The dissociation laser (Nd:YAG 3rd-harmonic pumped dye laser, 1 mJ per pulse) photolyses the Br_2, in the wavelength region of 480-490 nm. This photodissociation wavelength yields mostly Br + Br* fragments, from the first electronically excited product channel. After a variable delay, the probe laser (Nd:YAG 3rd-harmonic pumped dye laser pulsed at 10 Hz, frequency doubled, 0.15 mJ per pulse) ionises the bromine atoms remaining in the laser focal region via a (2 + 1) REMPI scheme, probing the $^4D_{5/2} \leftarrow^2 P_{3/2}$ transition at 264.211 nm. The experimental apparatus is identical to that for the NO_2 experiment, as described in section 2.4.3 (see figures 2.11 and 2.12.

3.2.1 Determination of the dissociation wavelength

The wavelength of the dissociation laser is critical to the success of this experiment, and therefore must be carefully considered prior to performing the experiment. To get the greatest stopped signal, the wavelength of the greatest absorption peak must coincide with that which produces photofragments matching the peak velocity of the molecular beam. Previous experiments on NO_2, had too much background noise to be able to scan quickly and determine the wavelength required for velocity cancel-

lation simultaneously – it was impossible to be both fast and accurate. Therefore some extra measurements were required. For Br_2, this proved to be unneccessary – the zero velocity signal was strong enough such that it was possible to scan the dissociation laser with a short delay before probing, and still be able to see the signal in real-time, thus being able to take the maximum of the scan to be the point of velocity cancellation. The calibration of the dissociation wavelength could be done via the velocity-map images using the velocity 'crests' as described in section 2.4.7. The ease with which this measurement could be taken renders the action spectrum convolution method somewhat obsolete. The method may still prove useful if molecular velocity cancellation is attempted in the future.

3.2.2 Bromine calibration

The calibration of the velocity-map for bromine was performed in an identical manner as for the NO fragments described in section 2.4.4. The images, taken at zero-delay time, were Abel inverted to best determine the radii of the individual rings, and a velocity was calibrated in terms of pixel count. This calibration worked correctly for wavelengths above the dissociation threshold for the B state at 510.4 nm. At 495 nm dissociation, a second ring appeared just outside the innermost ring, showing that a second dissociation channel had opened to create faster fragments. The energy of the laser probe is much too large to create a ring of this radius from photodissociation alone: at 495 nm dissociation wavelength, the total kinetic energy release (TKER) for the new ring is around 660 cm^{-1} above that of the innermost ring. Similarly, a third ring can be seen around the ring arising from dissociation to Br + Br, for dissociation to the limit of the C state, implying that this also has excess energy coming from an internal mode of the Br_2 molecule.

If we attempt to quantify which internal degrees of freedom are exhibiting this behaviour, we can presumably exclude the rotation modes, since the rotational constant for Br_2 is very small (B_e = 0.082 cm^{-3} [24]), a great many rotational levels

would have to be populated to produce an excess energy of 660 cm^{-1}. If we account for the vibrational levels, the TKER could be explained by $v = 4$ for the inner ring of the at $\lambda = 495$ nm, and $v = 5$ and $v = 6$ for the 500 nm pair.

However, at 5 K there ought to be no appreciable vibrational states populated other than $v = 0$. Even at 300 K, the Boltzmann equation (3.3) shows that 80 % of the molecules will be in the $v = 0$ state, and this fraction has dropped off to 0.2 % for $v = 4$.

$$\frac{N_i}{N} = \frac{e^{E_i/k_{\mathrm{B}}\mathrm{T}}}{\sum_j e^{E_j/k_{\mathrm{B}}\mathrm{T}}}, \tag{3.3}$$

where $\frac{N_i}{N}$ is the fraction of molecules populating state i, and E_i is the energy of the vibrational state. The energy of each state can be calculated using equation 3.4.

$$\Delta E(v_n - v_0) = v\omega_e + v(v+1)\chi_e\omega_e, \tag{3.4}$$

where v is the vibrational level, ω_e is the vibrational constant and χ_e is the anharmonicity constant. For bromine, these values have been sourced from the NIST Chemistry Webbook [21].

Notably, this dissociation wavelength region is the same region for which the A $^3\Pi_u(1_u)$ state of the bromine molecule begins to absorb. It could be possible that there are some other effects beginning to emerge. Since we are unable to see any rings for $v = 1$, 2 or 3, it stands to reason that the dissociation photon energy comes into resonance with a higher excited state, which may offer a competing dissociation pathway. Critically, the presence of this unknown dissociation pathway does not affect the calibration of the velocity-map images, since this can be calculated purely from the $v = 0$ rings.

The other side-effect of having a variety of ring sizes with which to calibrate the velocity-maps, is that we can extrapolate the data to get a dissociation energy, D_0, with which we can compare to existing data as a check for accuracy. Figure 3.3 shows this, giving D_0 to be 19578 cm^{-1}, which is very close to the literature value

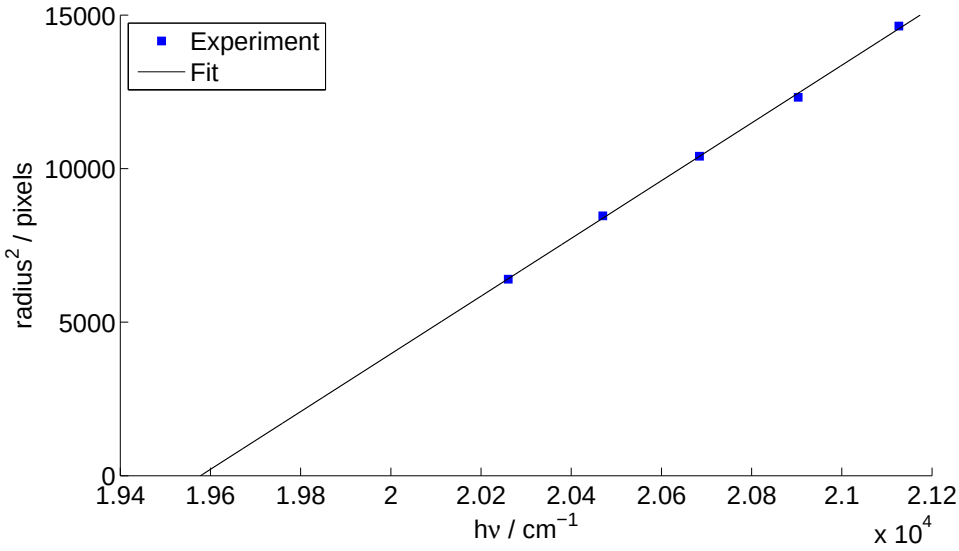

Figure 3.3: Plot of the dissociation photon energy versus the square of the inner ring radius for 475-495 nm, extrapolated to zero radius. This yields the dissociation energy, D_0, of 19578 cm^{-1}.

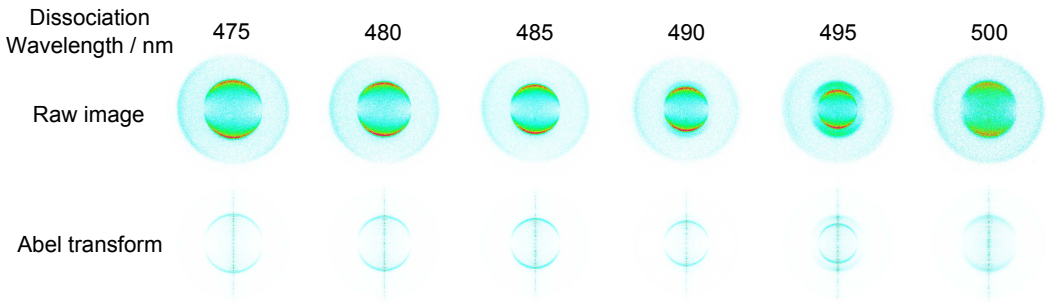

Figure 3.4: Velocity-map images at zero pump-probe delay for various photolysis wavelengths, with the Abel inverted distribution shown below. The ring sizes are given in table 3.1.

of 19580 cm^{-1} [17].

The data gives a velocity to pixel ratio of around 3.95 ms^{-1}/pixel. We can now use this to calculate the velocity to pixel ratio for the Br_2 molecules in the molecular beam from the TOFs.

$$t_{\mathrm{Br}_2} = t_{\mathrm{Br}} \frac{m_{\mathrm{Br}_2}}{m_{\mathrm{Br}}}, \tag{3.5}$$

where t is the TOF of the species and m is the mass. The average TOF for the Br^+ ions is 13.7 μs, and is 19.3 for the $Br_2{}^+$ ions. This gives a velocity to pixel ratio of about 2.8 units for the Br_2 molecule, which we can use to calibrate the molecular

λ(air) / nm	hν / cm^{-1}	pixel radius (inner ring)	pixel radius (outer ring)	ms^{-1} / pixel (inner ring)	ms^{-1} / pixel (outer ring)
475	21126.58	121	226	3.98	3.92
480	20903.15	111	223	4.01	3.88
485	20684.39	102	215	3.99	3.94
490	20470.17	92	213	3.97	3.89
495	20260.33	80 / 112	205 / 222	3.99 / 4.01*	3.94 / 3.98**
500	20054.76	111	223	4.01**	3.94***

Table 3.1: Velocity-space calibration for the Br atom. Notably, as the wavelength approached the dissociation threshold (510.4 nm), extra rings appear (figure 3.4). In the cases of the 495 and 500 nm dissociations, the rings can be approximated by invoking the vibrational levels of the Br_2 molecule – $v = 4^{*}$, 5^{**} and 6^{***}.

beam velocity-maps to get the molecular beam velocity average and distribution width.

In order to determine the temperature of the molecular beam, velocity maps were created by preparing $Br_2{}^{+}$ ions with a (2 + 1) REMPI process at 264.333 nm [25]. Using the data shown in figure 3.5, we can estimate the molecular beam temperature from the velocity distribution of the gas. Along the z-axis, the FWHM velocity is 39 ms^{-1}, about 10 % of the molecular beam velocity, and along the x-axis, the FWHM is 8 ms^{-1}. This corresponds to moving-frame kinetic temperatures of $T_z \sim 5$ K and $T_x \sim 250$ mK.

3.2.3 Optimization of the zero-velocity signal

There are various techniques that can be tried to optimize the signal. It is however, important to ensure that any signal improvement is due to an increase in stopped signal and not the background of the system. It is quite easy to accidently increase the level of the background signal in the experiment and be unaware that the signal has disappeared. Examples of experimental parameters and their effects are outlined below.

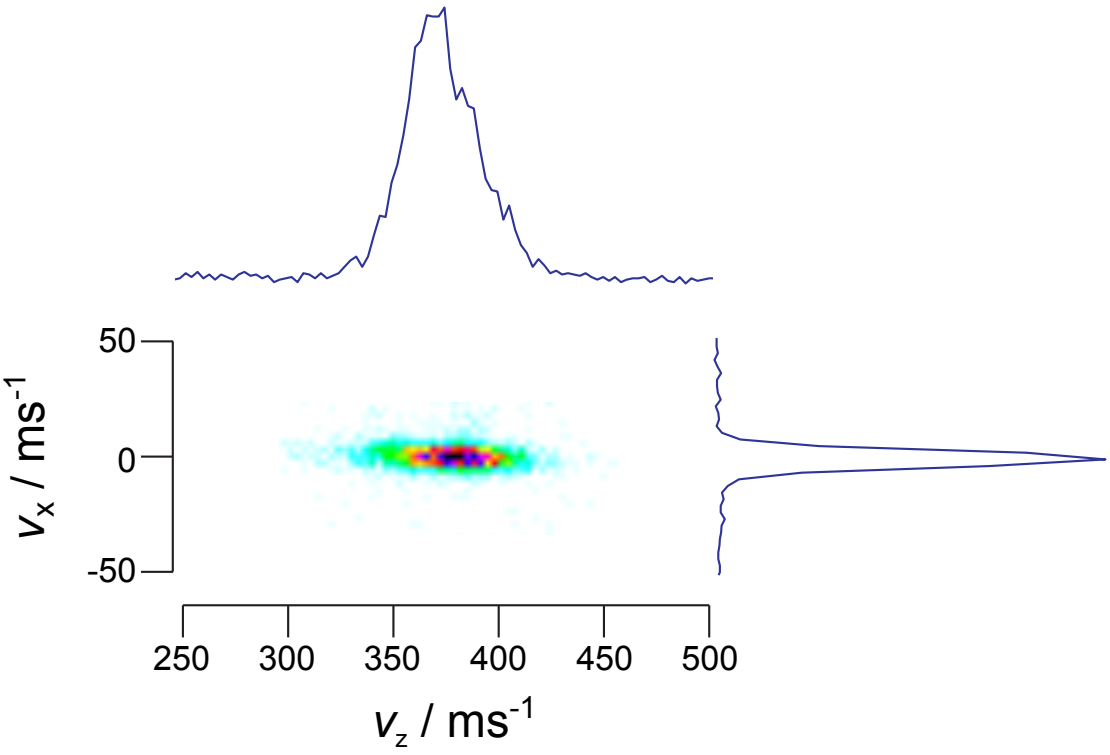

Figure 3.5: A velocity-map image of the molecular beam, taken on a Br_2^+ REMPI line. The velocity profiles through the centre of the pulse are shown

Pressure

The molecular beam backing pressure was varied by creating a 10 % mixture of bromine in krypton gas at 2 bar in a sealed mixing vessel. If we consider a binary gas mixture, the partial pressures of the final gas mixture will be related to their mole fractions:

$$p = p_{Br_2} + p_{Kr}, \tag{3.6}$$

$$p_{Br_2} = \chi_{Br_2} p, \tag{3.7}$$

$$p_{Kr} = \chi_{Kr} p, \tag{3.8}$$

where p is the total system pressure, and χ_x and p_x are the mole fraction and partial pressure of species x respectively. If we reduce the overall system pressure, the mole fractions remain the same, and therefore the relative concentrations of each species within the molecular beam remain the same. Thus, the pressure was changed by pumping out small amounts of the gas mixture from the mixing chamber, to keep

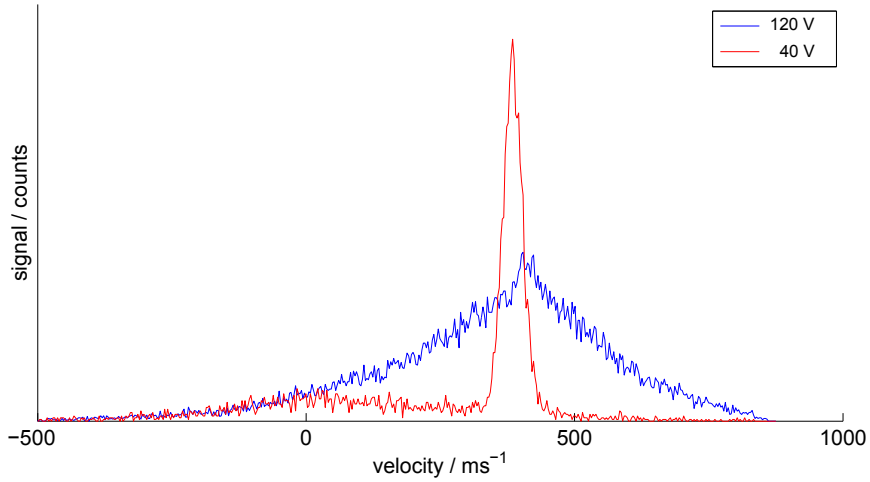

Figure 3.6: Profiles of the molecular beam images at settings of 120 V(blue) and 40 V(red). It is fairly clear then, that the background level is unsatisfactory at high opening voltages, and a clean molecular beam is only formed at the lower voltages.

the ratio of Br_2 to Kr identical. The experiment took images of the Br_2 molecular beam, and of a stopped signal at 20 μs to compare the effects on both the molecular beam and fragment signals.

A major problem in the detection of signals at long pump-probe delay was the amount of background noise centered around zero velocity, which can obscure the stopped signal. Background noise is determined to be any signal that cannot be described as being part of the supersonic expansion, with the associated narrow velocity distribution, for instance, that which would be created by ionisation of background gas in the chamber. Generally, background signal is centered around zero-velocity with a room-temperature distribution. Examples of mostly supersonic (red) and mostly background (blue) signals can be seen in figure 3.6. To obtain these data, a velocity-map image of Br_2^+ gas was taken using REMPI at 264.1291 nm [23] at differing backing pressures of the gas mixture and voltages applied to the nozzle. Both of these factors will have a great effect on the gas load to the chamber. Figure 3.7 shows two plots: the blue plot is the total integrated signal from the images, which is clearly increasing linearly as the backing pressure increases. This is due to the greater gas load entering the chamber. However, the red points show the ratio of the supersonic part of the expansion to the background signal, as calcu-

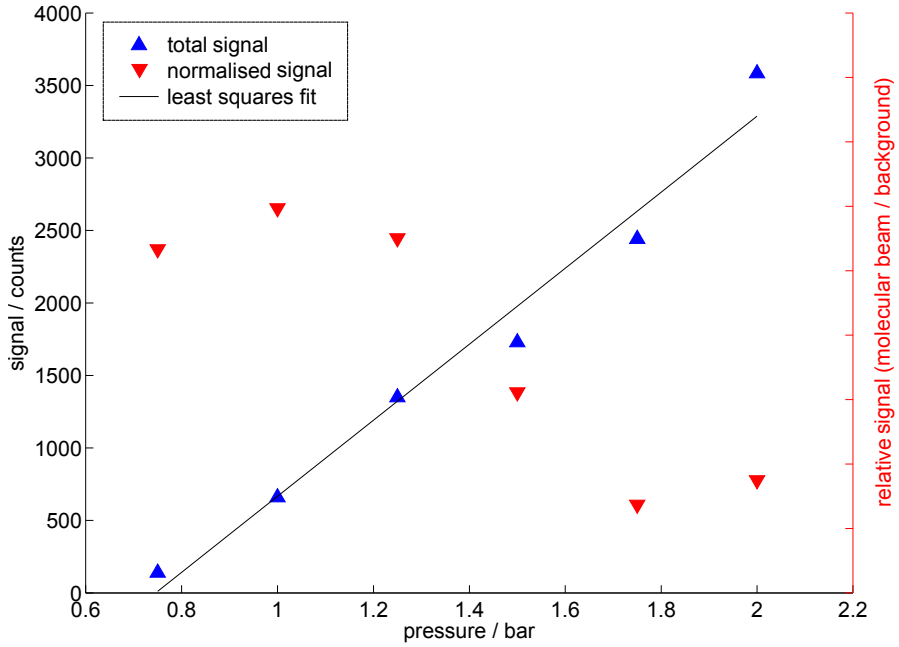

Figure 3.7: Molecular beam signal along molecular beam axis from VMI images. The blue points show the raw signal level over the whole signal integrated over the velocity-map image, and the red points show the relative proportions of signal to background counts in the images. The plots are for different Kr backing pressures, and show the increase in background noise above approximately 1.5 bar. Relative signal is calculated by integration of two Gaussians on the image, one supersonic and one thermal, and comparing the levels. The baseline levels are included as a guide for the eye.

lated by fitting Gaussian peaks to each part of the distribution, and comparing the integrated areas of the two. The background appears to increase with the molecular beam backing pressure; however, further study showed that there was a threshold at around 1.5 bar, above which there was a sharp increase in the background level, as illustrated by the drop in the molecular beam to background ratio seen in figure 3.7 (red triangles). At lower pressures, the ratio of background gas to supersonic signal is relatively constant.

To quantify the effect, ion images of the molecular beam pulse were taken at different backing pressures, but under otherwise identical conditions. The images were compared by integrating the number of counts over all pixels for a given v_z (the velocity along the molecular beam axis). This compresses the two dimensional ion image into one dimension, and the noise levels could be compared. The sudden

increase in noise at a critical backing pressure is confusing, although it could be attributed to the changing flow properties of the molecular beam at different backing pressures, or possibly be related to Br_2 molecule cluster formation [26].

There is a linear relationship between the pressure of the backing gas, and the stopped signal, up to the 2 bar measured in the experiment, as seen in figure 3.7. It is possible that the molecular beam becomes less well-defined at the low pressures, such that supersonic expansion is not completely realised, and there is a more effusive quality to the gas expansion, though in this case there should really be a plateau in the pressure dependence.

Nozzle voltage

Varying the voltage pulse applied to the solenoid of the valve changes the flow of the molecular beam. Figure 3.8 illustrates the behaviour of the signal amplitude as a function of this voltage. As the amplitude is increased, the overall signal increases (blue stars). The primary cause of this increased signal, however, is residual gas in the vacuum chamber. Increasing the molecular beam valve pulse amplitude has little effect on the density of Br_2 in the beam (red squares). In fact, the increase in amplitude appears to have an adverse effect upon the actual stopped signal (green circles); at the highest voltages, the signal at 20 μs completely vanishes, indicating that the extra background gas is removing stopped atoms from the focal region through elastic collisions.

It is possible that increasing the voltage keeps the solenoid in the open position for too long, and the source becomes less supersonic in nature. The plots of z-axis velocity distribution for two different opening voltages are illustrated in figure 3.6. For the lower voltage pulse, red, the molecular beam velocity distribution is narrow and sharp, indicating successful supersonic expansion. However, for a larger voltage, blue, there is an almost Gaussian distribution of velocities around the molecular beam speed, spreading for hundreds of metres-per-second. The source of this messy

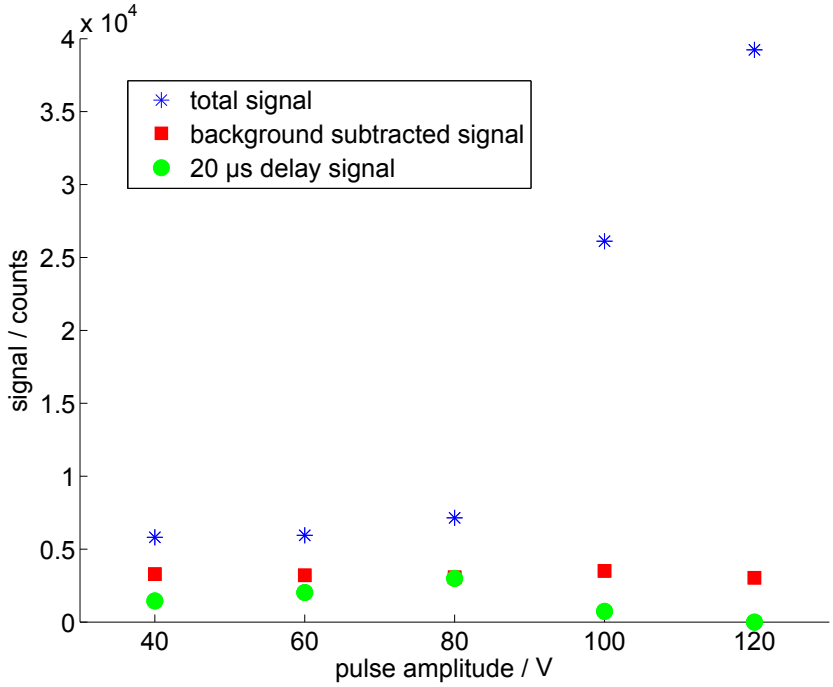

Figure 3.8: A plot of the voltage amplitude versus the signal taken from the velocity-map images. The blue stars show the total signal from the images, taken for on a Br_2^+ REMPI line at 264.1291 nm, the red squares show the same signal with the Gaussian background removed, and the green circles show the Br^+ ion signal at a delay of 20 μs.

signal is unclear. It may be a result of the longer opening time of the nozzle flooding the chamber with gas, but without a more detailed investigation we cannot be certain. We can be certain that the lower opening voltages should be used in the experiment.

Power saturation

There is an obvious limit to increasing the power of the dissociation laser to increase the stopped signal; there are a limited number of bromine molecules in the beam, and at some laser power, all available molecules will be dissociated, and there will be no further benefit to increasing the power. Figure 3.9 shows this; this signal increases linearly with dissociation laser power, up until around 1 mJ, at which point the signal plateaus, indicating saturation.

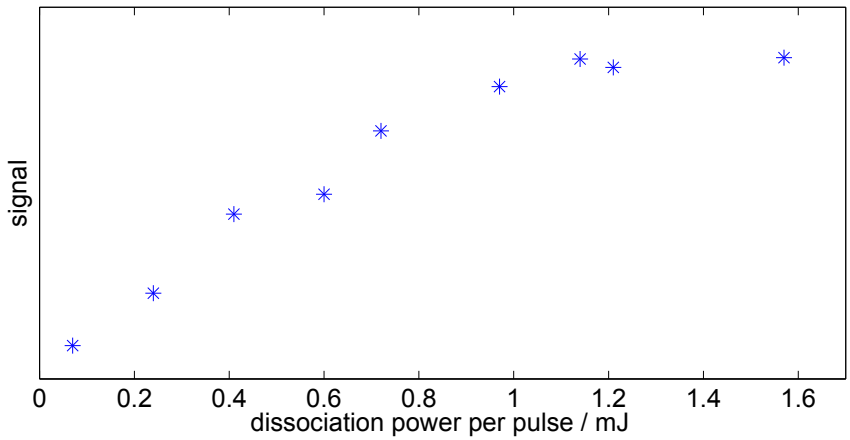

Figure 3.9: Plot of dissociation laser power at the chamber versus signal for the experiment.

3.3 Results

The experiment yielded velocity-map images of the type seen in figure 2.22. In these images, the molecular beam is travelling from left to right, with ions extracted perpendicular to the page. The electric vector, ϵ, of the dissociation laser is horizontal in the images, which is parallel to the molecular beam in the experiment.

The bromine signal could be seen for in excess of 100 μs, which is an order of magnitude greater than that seen for the experiments with NO. In the velocity-map images, the loss of the faster atoms from the ionisation region can clearly be seen, as can the overall contraction of the velocities of the ions as the delay is increased. Figure 3.11 shows that as the delay time increases, the signal drops off almost exponentially. However, since we can see signal at very long delay times – a pump-probe delay in excess of 100 μs – and the fact that the logarithmic plot asymptotically approaches a finite value, shows us that there is a real signal being maintained in the ionisation region, which cannot be attributed to anything other than atoms remaining in the laser focal volume due to velocity cancellation. These images however, were taken in three batches to maintain single ion-counting levels. Since the imaging software counts the number of strikes above a certain threshold, we do not want to lose signal by having two ions hitting the same point on the detector

The zero-velocity point, is located on the left hand side of the image. As the delay between dissociation and probing is increased, the faster moving atoms, i.e. those on the right hand side of the image, leave the focal volume of the probe laser, leaving only the atoms which have achieved velocity cancellation (see figure 3.10).

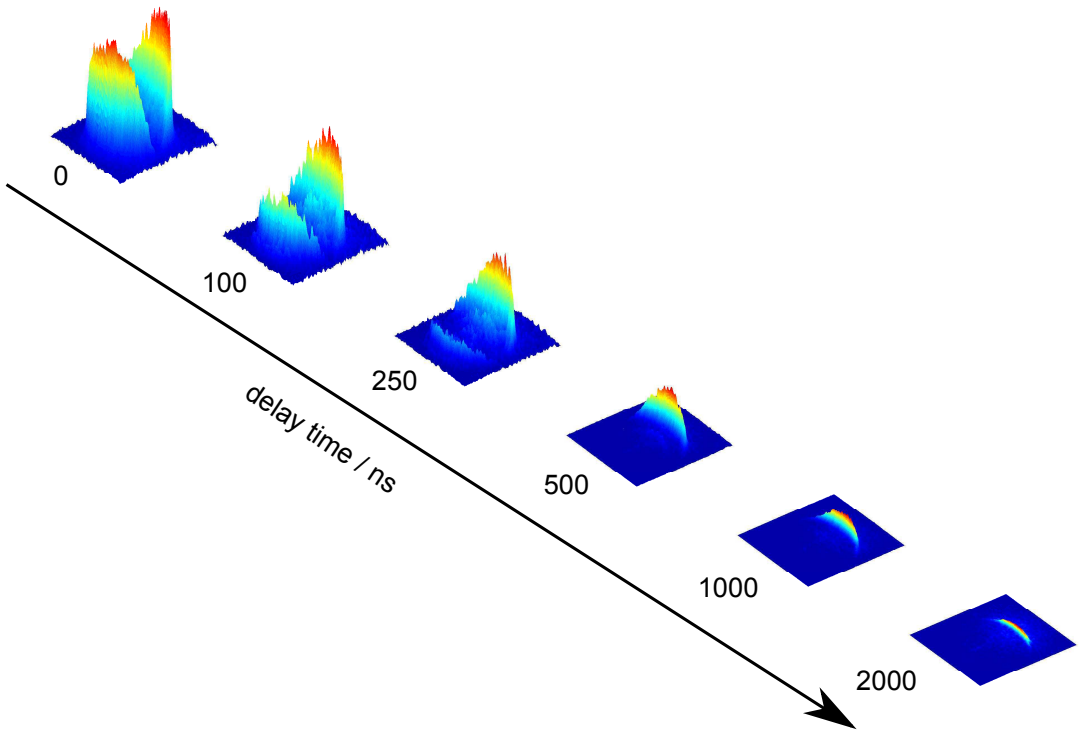

Figure 3.10: A visualisation of the short delay time decay of Br^+ ion signal over the first 2 μs, showing the velocity-dependent reduction in signal level from the experimental data. The faster atoms will be moving towards the left in this image, and the signal from these decays much faster than those that have undergone velocity cancellation.

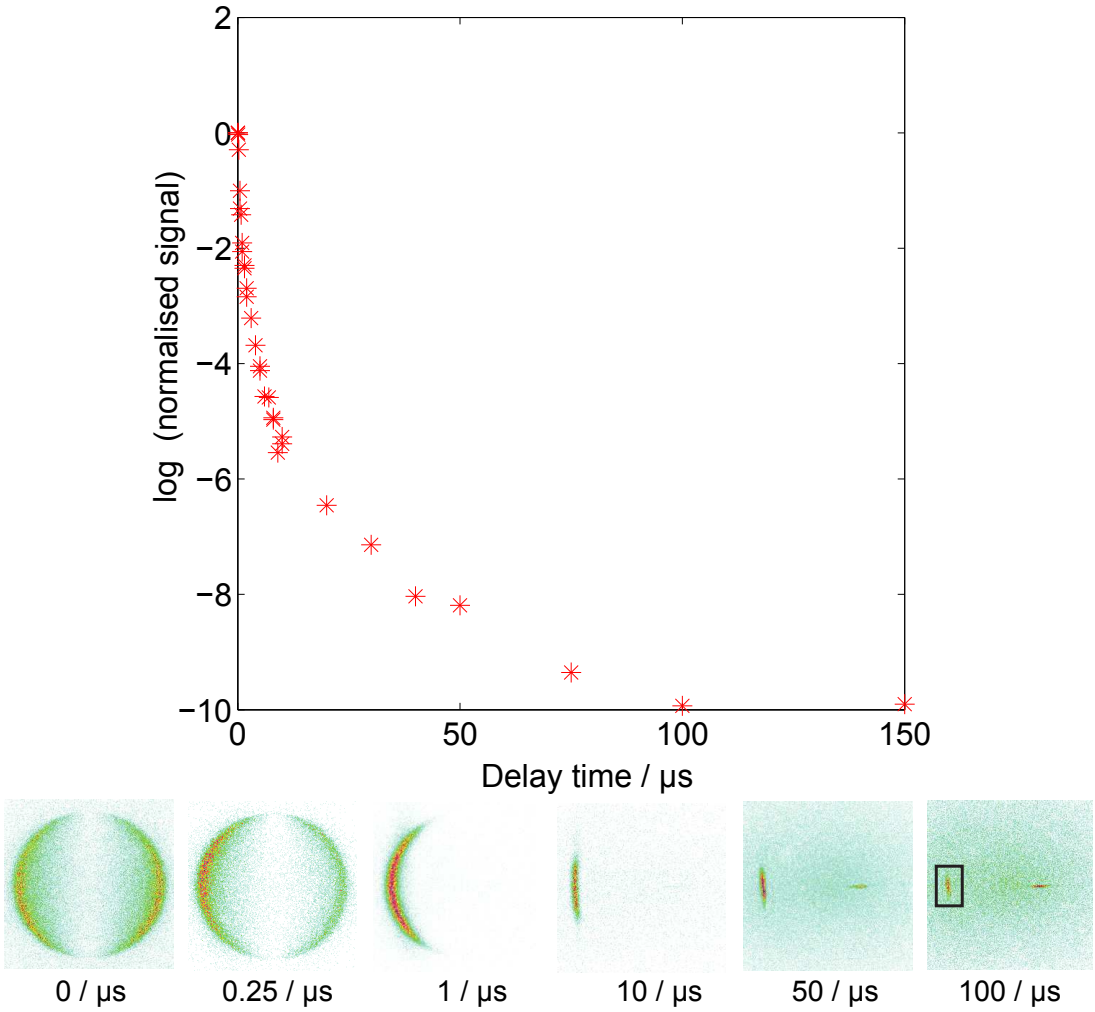

Figure 3.11: Above: Logarithmic plot of the integrated signal against delay time. Below: The associated ion images at various delay times are shown. The signal at 100 μs is boxed for clarity.

simultaneously. Hence, the probe laser intensity is decreased at the shortest delay times, when there is an abundance of ions being generated, and the intensity is increased at the longest delays for which there are few ions created. The short time data, taken between -10 ns–2 μs, and visualised in figure 3.10, were taken at the lowest laser power. The negative time signal was taken to make sure that our temporal laser overlap was correct; at negative time, i.e. probe before dissociation, we see the signal disappear. The medium time data were taken over the interval of 0–10 μs, overlapping the chosen delays so that the two curves could be normalised to one another. These data were taken at a slightly higher laser power. Finally, the long time delay data were taken at the full laser power of 0.15 mJ/pulse, and cover the region of 5–150 μs. To construct the full decay curve, scaling factors were determined by comparing the overlap regions of the 3 experimental conditions. Having obtained these, the three curves could be normalised to zero delay.

A notable point is that the zero delay image is not in fact the image that was used for normalisation, since there appeared to be some enhancement of the ionisation of the atoms when the two lasers were temporally overlapped, by a factor of approximately two. This is due to a (2 + 1') REMPI process, with ionisation occurring using a dissociation laser photon. Hence, the 10 ns delay signal was actually used for normalisation.

3.3.1 Analysis of the images

The velocity-map images, a sample of which can be seen in figures 3.12 and 3.13, were analysed by measuring the integrated number of counts per pixel. Doing so not only gives us an idea of the velocities of the ions, but also of the rate of production, and therefore allows comparison of signal magnitude. These could then be normalised to the zero-delay image level, and we can manufacture a decay curve – a measure of the rate of loss of faster atoms over time.

3.3.2 Theoretical analysis of the data

To simulate and quantify the data from the experimental images, a theoretical treatment of the process was created. The initial positions and velocities were created using Monte Carlo selection from the known distributions, and the molecules were then allowed to fly freely into a simulated dissociation region. The positions of atomic fragments are then propagated with statistically weighted recoil velocities, calculated from the angular anisotropy parameter, β (equation 2.12) and the branching ratio, ϕ (equation 3.1). After a given delay, the atoms were counted as detected if they remained within a set region. Simulated velocity-maps and decay curves could then be built up based on the final velocities of the ions.

The Monte Carlo simulation was written in Matlab. A sample of atom positions were generated in a cylindrical region approximating the dissociation laser focal volume, taken to have a radius of 200 μm and a length of 5 mm. These were each assigned a velocity, randomly assigned from a normal distribution of velocities centered at the molecular beam velocity, with parameters calculated from the velocity-map image of the Br_2 molecular beam. With the Br_2 positions and velocities calculated, the next step was to create the COM fragment properties. A program was written to calculate the correct distribution of recoil velocities. This meant determining the correct branching ratio, ϕ, of the fragmentation to the two different dissociative states, each with their respective β parameters, and then calculating the distribution of the recoil angles, θ and φ (see figure 2.3) to give a set of recoil velocities along each axis. The β parameters were taken from Cooper *et al.* [17]; for the dissociation via the B state, to the Br + Br* products, the β parameter was taken as +1.8, whereas for the dissociation via the repulsive C potential, to Br + Br, it was taken to be -1. The molecular beam velocity, v_z, was generated by calculating the cumulative probability of dissociation at angle θ, and then randomly assigning θ from interpolation of that function, thus maintaining the correct probabilities under randomisation. The perpendicular velocities, v_x and v_y could

then be calculated from this value and a randomly assigned angle φ. In addition, the isotopic abundances were accounted for when calculating the recoil velocities, again under randomisation. These velocities are then combined with the molecular beam velocities to reveal the lab-frame velocities of the fragments.

To generate a decay curve, the atoms are allowed to fly freely for a given amount of time, and are then tested to see if they remain in the probe laser focus, here optimised to be 180 μm radius and 4 mm long. The critical factor in determining the decay rate for the experiment is the size of this ionisation volume: altering this changes the initial rate of decay over the first microsecond. The optimisation was performed using the experimental data, looking at the short delay part of the decay curve to estimate the radius of the laser beam. We determine the probe laser dimensions by fitting this initial decay to the model. The signal is then normalised to the zero-time level. The simulation of the velocity-map images is created from the same source, via a 2-dimensional histogram with velocity bin sizes equal to the size of one pixel on the experimental images. This can be seen in figure 3.12, third row, where the points in red are the experimental points, and the dashed blue line is the simulated fit, based on the calculated laser volume. The experimental points were determined by integration of the signal, with the background gas signal removed where possible.

Significantly, the simulations allow us to calculate the velocity distributions of the atoms at very long delay times. We can compare the distributions along the $x-$ and $z-$axes, calculated from the integration of the 2D velocity distributions along v_x and v_z of the velocity-maps, (see figure 3.13). Notably, at the longest delay times (50–100 μs), the expected velocity distribution calculated in the Monte Carlo simulations, are much narrower than those observed experimentally. This could be attributed to the effect of ionisation upon the atom velocities. Ordinarily, ionisation can be considered to have a negligible effect upon the velocity distribution; in the ionisation process, the departing electron takes the majority of the kinetic energy

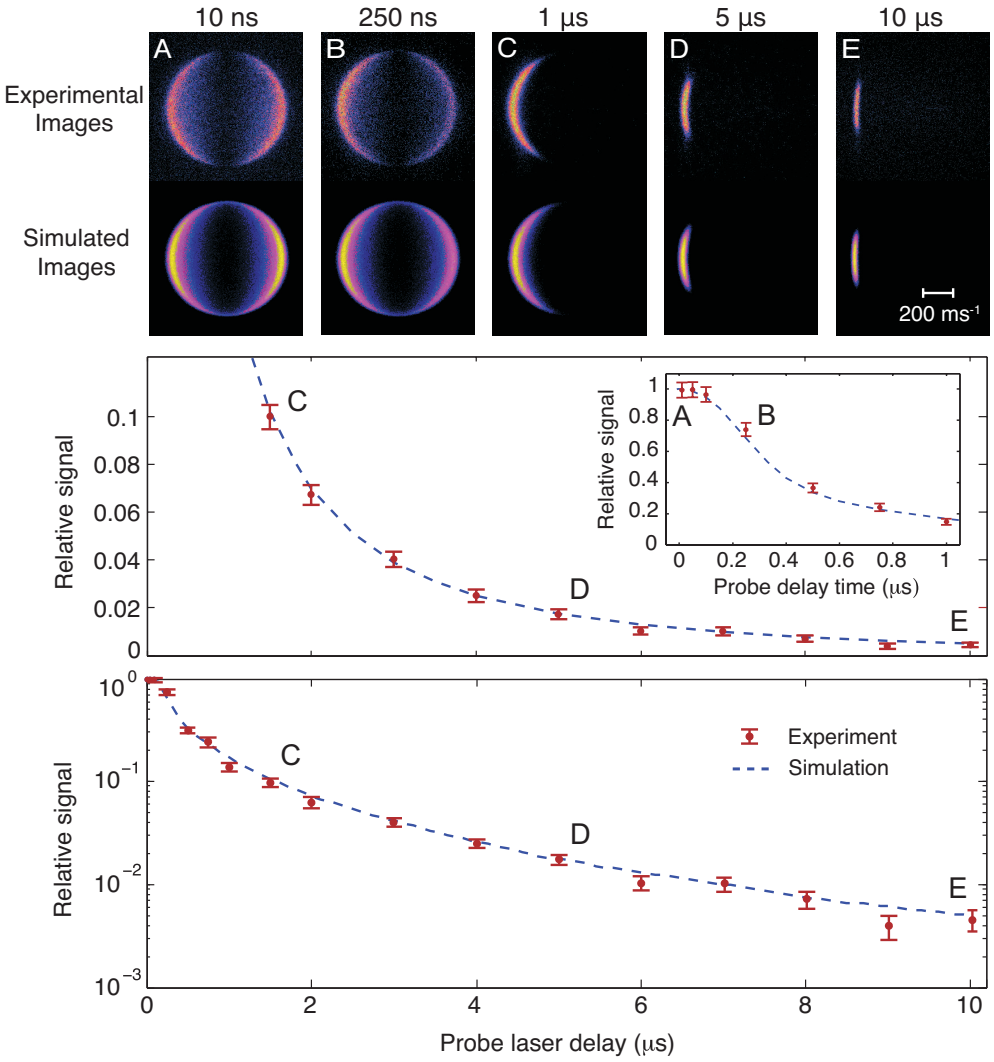

Figure 3.12: The decay of the bromine ion signal with respect to delay time between dissociation and probe. Top: experimental velocity-map images at delays of 10 ns, 250 ns, 1 μs, 5 μs and 10 μs, respectively. Second row: Simulated velocity-map images from a Monte Carlo simulation atom expansion. Third row: Decay curve over the first 10 μs with experimental points in red, and the simulated decay curve in blue (Inlay shows the very short delay times). Bottom: Logarithmic plot of the decay curve, experimental in red, simulation in blue.

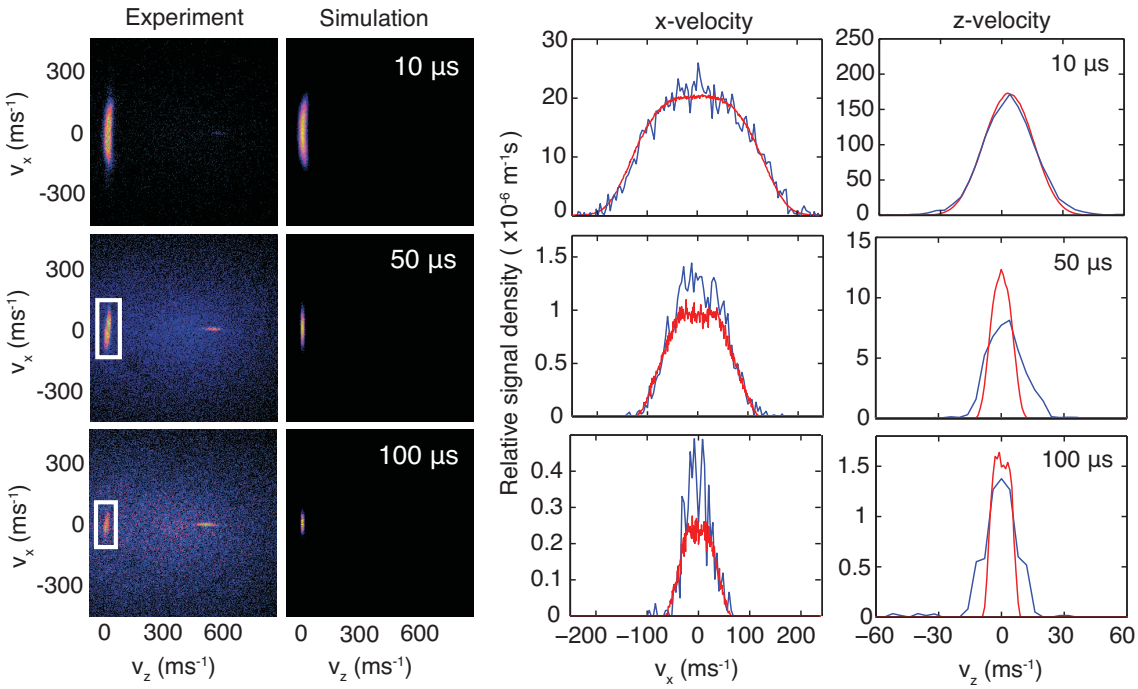

Figure 3.13: The comparison of the real experimental images (far left) at long delay times, and the equivalent simulated images (centre left). The profiles of the velocities in the laser direction, v_x (centre right) and the molecular beam direction, v_z (far right) are also shown. The experimental profiles are shown in blue, and the simulations in red. Note that the profiles are taken only from the boxed region on the velocity-map images.

Probe Delay	10 μs	20 μs	50 μs	100 μs
$\Delta v_z^{\mathrm{exp}}$ (m s^{-1})	29	21	20	17
$\Delta v_z^{\mathrm{sim}}$ (m s^{-1})	28.7	18.6	11.3	10.5
$\Delta v_x^{\mathrm{exp}}$ (m s^{-1})	255	219	143	59
$\Delta v_x^{\mathrm{sim}}$ (m s^{-1})	263	211	150	75
T_z^{exp} (K)	1.51	0.80	0.73	0.52
T_x^{exp} (K)	112	83.2	35.5	6.0
Δv_z^{Br} (m s^{-1})	27	17	7.0	3.9
T_z^{Br} (K)	1.26	0.49	0.09	0.03

Table 3.2: Velocity spreads (FWHM) and associated temperatures derived from experimental and simulated Br^+ ion velocity distributions along the z- and x-axes (see Fig. 3). The underlying z-velocity spread, Δv_z^{Br}, and temperature, T_z^{Br}, for the neutral Br atoms obtained through simulations is also given. Effective temperatures are defined here assuming a 1D Maxwell-Boltzmann distribution

release, purely from a mass ratio argument (see equation 3.9).

$$E_{\mathrm{kin}}^{\mathrm{Br}^+} = \frac{m_{\mathrm{e}}}{m_{\mathrm{Br}}}.E_{\mathrm{kin}}^{\mathrm{Br}}. \tag{3.9}$$

This equates to the bromine ion receiving 6.8×10^{-6} of the available kinetic energy, ordinarily a negligible amount. However, with the high excess energy associated with photoionisation, this equates to an added recoil velocity of approximately 6 ms^{-1}, which confers a significant blurring effect onto a velocity distribution which ought to be very narrow, and centered around zero. Hence, it can be assumed that the atom velocity distribution is narrower than that of the ion velocity, as can be seen by comparing Δv_z^{Br} and $\Delta v_z^{\mathrm{exp}}$ in table 3.2. This blurring effect from electron recoil has been incorporated into the simultated results. Hence, the temperatures listed are obtained from the simulated Br *atom* profiles (as opposed to ion profiles), as these ought to be the realistic velocities which we will be able to trap in future experiments.

It is also plausible that some of the broadening of the profiles could be attributed to the non-zero dissociation laser linewidth, although the effect of this on the final velocity distributions has not been added to the simulated results.

3.3.3 Density

A critical factor in determining whether or not the experiment will become a viable source of cold atoms is the density of the sample. The method of detection, allowing fragments to fly out of the laser volume, necessarily means that as the experiment progresses, the density of the bromine atoms will decrease exponentially. However, for the technique to progress, we will need to find some method of confining the cold fragments. Thus, we can estimate a density that could be trapped, which is a better gauge of the usefulness of the experiment than attempting to calculate the density seen at 100 μs.

The absolute detection efficiency of the experiment is an unknown quantity, hence making it impossible to create an accurate estimate for the number of atoms stopped from the data. However, we do have some idea of the expected numbers of atoms that we are creating, so an upper limit can be calculated from the molecular beam density [27, 28]. If we assume that the measured molecular beam temperature from the Br_2 is equally applicable to the krypton, then at a distance of 121 mm from the nozzle, we predict that the Kr density will be of the order of 10^{13} atoms cm^{-3}, and therefore the Br_2 density to be on the order of 10^{12} molecules cm^{-3}. Photodissociation simulations indicate that the fraction of bromine atoms produced with a kinetic energy less that 1 K (i.e. $\frac{1}{2}mv^2 \leq k_B T$, where $T = 1$ K) is 2.5×10^{-4}. The highest strength commercially availble NdFeB magnets have a remanence of approximately $B_r = 1.5$ T, which, if this is taken to be the trap depth, should correlate to a temperature of about 1 K. Using this definition, and assuming for the moment that we are in a collision-free environment, and that the dissociation is fully saturated, then this equates to a zero time density of near zero-velocity atoms of around 10^8 atoms cm^{-3}. This is comparable to previous experiments using velocity cancellation techniques [29], and should therefore be sufficient to study chemical reactions, as suggested in chapter 1.

3.4 Experimental issues

It was noted that there were several issues with the implementation of the experiment as it stood. Stopped signal is incredibly sensitive to the overlap of the two lasers. Any misalignment would prevent the zero-velocity signal from being seen at all. It is also important to keep a keen eye on any drift in the wavelength of the probe laser. At times, if the wavelength wandered at all, the photon absorption of the atoms with different velocities would change, due to the Doppler effect. This meant that it was possible to pick up background signal but not the zero-velocity signal if the wavelength was not perfectly resonant.

Over the course of a day, it was sometimes possible to see even zero-delay signal vanish to almost nothing, for no change in laser intensity or wavelength. This may be due to a depletion of the bromine gas from reactions with the steel gas line. What had at first seemed a simple addition to the experiment – adding a metal vial of bromine liquid onto the end of the gas line – was now corroding the tubing, and in the process, removing the reagent gas itself. Keeping a separate reservoir of Br_2/Kr mixture helped in the short term, but future designs would have to consider this reactivity more carefully. The bromine also reacted with the metal interior of the general valve, which meant that this had to be cleansed on a relatively regular basis.

3.5 Appraisal of the atomic and molecular cases

Clearly, this chapter has demonstrated the greater applicability of the atomic case (section 3.3) when compared to the molecular case (section 2.5). The length of time after dissociation for which atoms can be observed is an order of magnitude greater than for molecules. The reasons for this are fairly plain to see. The dispersal of the photon energy between internal and kinetic energy of the fragments is considerably more predictable for the atomic case. One only has to consider the electronic excitation of the fragments, and by carefully tuning the dissociation wavelength,

the process can be encouraged to preferentially dissociate to the atomic states of choice [17].

When dealing with molecular fragments, there is a great deal more uncertainty. The energy can be leeched into internal rotational and vibrational states, often with limited options to control the apportionment. In the case of NO, the bent state of the precursor NO_2 means that there will be significant torque imparted upon the NO molecule upon dissociation. As such, there will be a great number of rotational levels populated. This diminishes the effectiveness of velocity cancllation

It is clear that the easiest route to advancing the applicability of the Photo-stop method will be to optimise the system with the atomic case, and attempt to demonstrate spatial confinement of the atoms.

3.6 Confirmation of the results and optimisation

In setting up the experiments in Oxford, the first step was to recreate the data from the Durham experiment [30]. This first meant a redesign of the existing Oxford experimental chamber, previously used in velocity-map imaging studies of NO_2 dissociation [31], in order to match the experimental oreientation used in Durham (see figure 2.11). The previous velocity-mapping apparatus was rearranged, so that the detection axis was perpendicular to the molecular beam. The alteration process was straighforward, indicating that the change from a standard velocity-map imaging rig to a machine capable of performing velocity cancellation is relatively trivial provided the vacuum chamber has been constructed with sufficient ports, and can be installed in a reasonably short time period.

There were a few experimental differences between this generation of experiment and the apparatus in Durham. For instance, there was no automated image processing software, so a new camera-PC interface had to be constructed, written in Labview by myself and Dr Chris Rennick. A new scaffold for the extraction electrodes had to be constructed; to ensure that the electrodes were fully co-linear with

the detection axis, an extension to the time-of-flight tube had to be built. The molecular beam, now pressurised behind the nozzle to 4 bar with argon as a carrier gas, was attached to an x–y translation stage on the entrance flange to the main chamber. The nozzle could thus be moved to optimise the signal. This made sure that the core of the molecular beam was being skimmed, rather than a component with a higher perpendicular velocity. This could be monitored on the velocity-map images; if the translation stage was too far to one side, molecules with a higher lateral velocity would be dissociated, and would hit the detector to one side.

The source chamber was pumped to a pressure of 2×10^{-7} mbar by a turbopump (Leybold TMP 1100c) backed by a two-stage rotary pump (Leybold Trivac), and the main chamber was pumped to a pressure of 1×10^{-7} mbar by a turbopump (Alcatel TMP 5400) with a two-stage rotary backing pump (Leybold Trivac).

The dissociation laser (Nd:YAG, Quanta-Ray, 3rd-harmonic pumped dye laser, Sirah Cobra-Stretch, using Coumarin 460, 2 mJ/pulse, measured at the chamber) operated at around 460 nm, a lower wavelength than that used in the Durham experiment. This is due to the increased photon energy required to stop bromine atoms produced from Br_2 moving with a velocity equal to the terminal velocity of a pure argon expansion. The bromine ionisiation was performed with a second laser (Nd:YAG, Continuum, 3rd-harmonic pumped dye laser, pulsed at 10 Hz, Sirah Cobra-Stretch, frequency doubled, using Coumarin 503, 0.15 mJ/pulse) to detect the bromine 2-photon atomic resonance $^4D_{3/2} \longleftarrow {}^2P_{3/2}$ transition at 260.536 nm.

3.6.1 Optimisation

Focussing

The focussing lenses for the two lasers were both reduced from a focal length of 500 mm to 300 mm in this iteration of the experiment. Hence the corresponding focal volumes were changed considerably. Referring back to equation 2.21, the beam radius at the focus is linearly proportional to the focal length, and as a result, the

beam radius is this experiment will be smaller than previously used. We observed that in the Durham experiment, the fast 'crescent' in the velocity-map image vanished after 250 ns, whereas in the Oxford case, it disappeared after 150 ns, which is consistent with a smaller laser focus. This will couple with the fact that the gas we are now seeding in, argon, has a higher terminal velocity (see equation 2.5) than krypton, and as such, are using a higher energy dissociation laser, creating faster fragments which will vacate the ionisation region more rapidly.

Corrosion

Initially, it was thought that the best method for creating the gas mixture was to use an identical bromine containment source as utilised in Durham; a steel vial of bromine liquid which could be heated and cooled to create the desired vapour pressure of bromine gas in a mixing chamber before adding a known pressure of seed gas. However, it was noted that the greater length of metallic gas line inside the source chamber was not efficiently heated by ordinary external heating tape, leading to the problem of bromine liquid condensing on the metalwork. Corrosion of the stainless steel pipework by bromine gas, most probably through reaction of bromine with water to form the corrosive HBr, was also a concern. Hence, a redesign of the external gas line was implemented. The tubing was replaced with PTFE pipework (Swagelok), which is chemically inert to halogen species. The steel bromine reservoir was replaced with a 250 ml glass bulb, which served as both bromine liquid housing, and gas mixing chamber. This amendment minimises the amount of metal that comes into contact with the bromine vapour at any time, thus limiting any possible corrosion. The only remaining problem would then be the General Valve nozzle itself, which is by necessity metallic, and would need cleaning on a regular basis. Cleaning the nozzle brought additional problems, however. Having bare metal in the nozzle merely facilitated reaction with any remaining bromine, so gas depletion whilst experimenting was noticeable. All metal surfaces must therefore be passivated, by

repeatedly passing the bromine gas over the surface. A more permanent solution may be to coat the internal mechanisms of the valve in a corrosion resistant substance, e.g. PTFE. The effect that this may have upon the operation of the valve is unclear, however, and this was not attempted here.

Spatial-map imaging

Spatial-map imaging (SMI) is an extension of the standard VMI arrangement, and was given as an alternative possibility in the original article by Eppink and Parker [32]. The voltage applied to the extractor electrode is greatly reduced when compared to the VMI case, resulting not in a mapping of particles of a single velocity to a single point on the detector, but those created at a given position in the focal region to a single detector point [33]. Figure 3.14 shows what happens to the spatial-map when the focus of the probe laser is moved horizontally (in the plane of the images). SMI turns out to be a useful tool in this experiment, since knowledge of the focal position of the probe laser is very important. The position of the spatial-map image of the bromine ions on the detector gives us information on where in the plane parallel to the ion-optics the ions are being formed. It is worth reiterating the advice offered by Wu [33], that whilst VMI is the major use of the Eppink and Parker ion optics design, the simple changeover to the SMI regime offers a powerful diagnostic for experimental optimisation.

Laser drift

An important complication (noted in section 3.4) was the drift in the wavelength of the probe laser. It could be seen in the previous iteration of the experiment that being slightly off the REMPI resonance would essentially image atoms with a different transverse velocity. This is best illustrated in figure 3.15; as the wavelength shifts, the probability of detecting atoms with higher velocities along the axis of the laser beam (left to right) is increased.

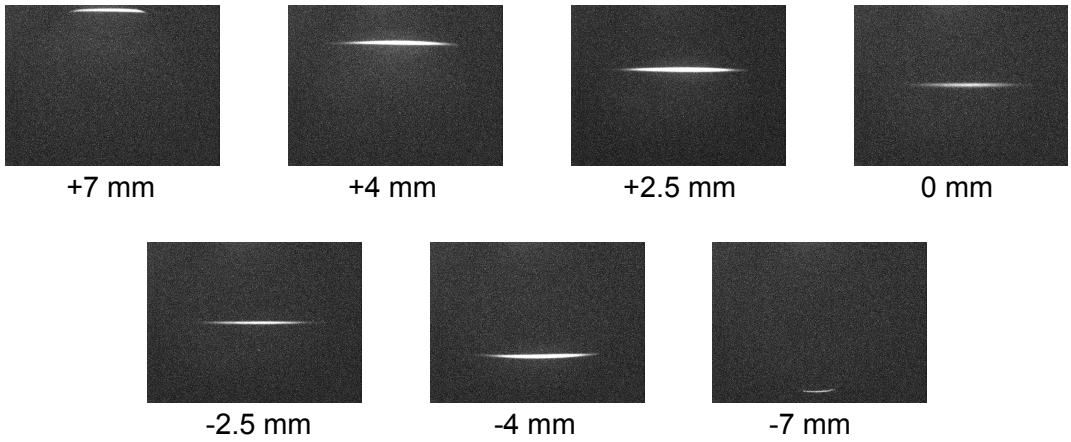

Figure 3.14: Spatial-map images of the Br_2 molecular beam, with the extractor plate voltage reduced to 1000 V. The distances indicate the displacement of the focus of the probe laser beam, calculated by measurement of the position of the entrance and exit of the beam from the chamber.

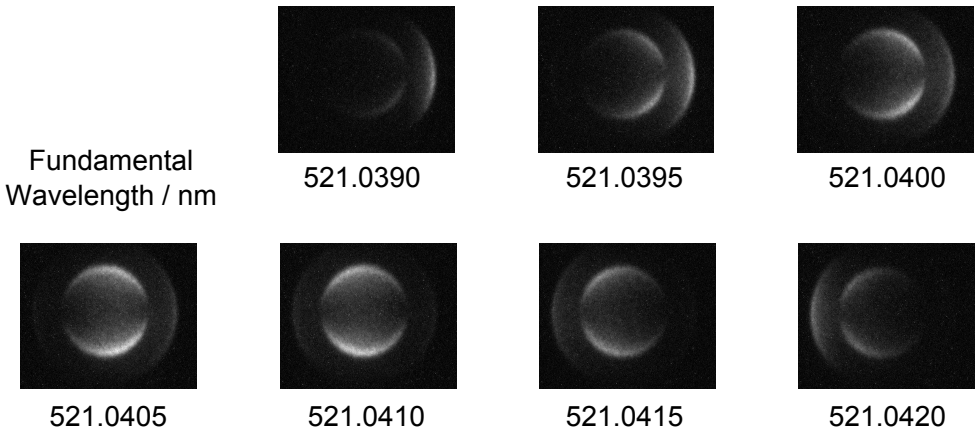

Figure 3.15: As the wavelength of the probe laser is increased, the Doppler shift experienced by atoms with different velocities along the axis of the laser beam brings the atoms in and out of resonance.

The wavelength of the probe in figure 3.15 would need to be centered at 521.0410 nm in order to be able to most efficiently detect atoms with zero lab-frame velocity along the laser axis, x. This dye laser is not frequency-stabilised to an external standard, so in order to consistently measure a zero-velocity signal, the wavelength must be constantly monitored. The ion image was therefore scrutinised for symmetry after every data acquisition stage. Symmetrisation confirms that the laser is not preferentially exciting atoms with a non-zero perpendicular velocity due to the Doppler effect.

In addition, a shutter for the dissociation laser was implemented, which could be controlled from the laboratory computer. This meant that the background subtraction could occur over much shorter periods, over which the wavelength is stable. For instance, a single experimental run may comprise of 20 shots with the dissociation laser blocked, and then 20 with the block removed. This would then be repeated several hundred times. As such, this was superior to previous methods of background subtraction, whereby one long scan would be taken with the block in, and one long one without, in which time the conditions may have changed more noticeably.

Secondary dissociation

A surprising side-effect noticed during the course of the Oxford experiment, was an unwanted dissociation pathway of the Br_2, arising from single-colour one-photon excitation by the probe laser, leading to an excess energy of just under 19000 cm^{-1}, or a fragment recoil velocity of about 1700 ms^{-1}. This is attributed to rapid dissociation following excitation to the $^3\Sigma_u^+$ (1_u) state [34]. The ring contributed little in most velocity-map images, since it was dwarfed by the two-colour signal. However, the ring can be clearly seen when overlap between the two lasers is poor (see figure 3.16), and needs to be considered in the simulations and later, time-of-flight experiments, as described in section 5.2.1.

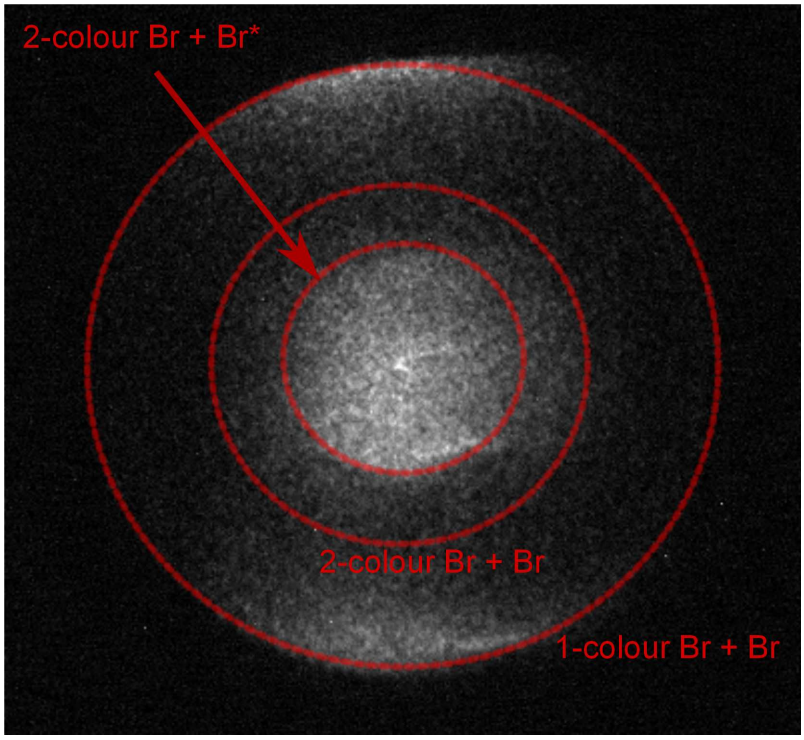

Figure 3.16: Velocity-map image captured during poor spatial overlap of the dissociation and probe lasers. Since very little signal is two-colour, the larger ring, attributed to one-colour dissociation by the probe laser, is clearly visible. The rings for the two two-colour pathways and the one-colour dissociation have all been circled for clarity.

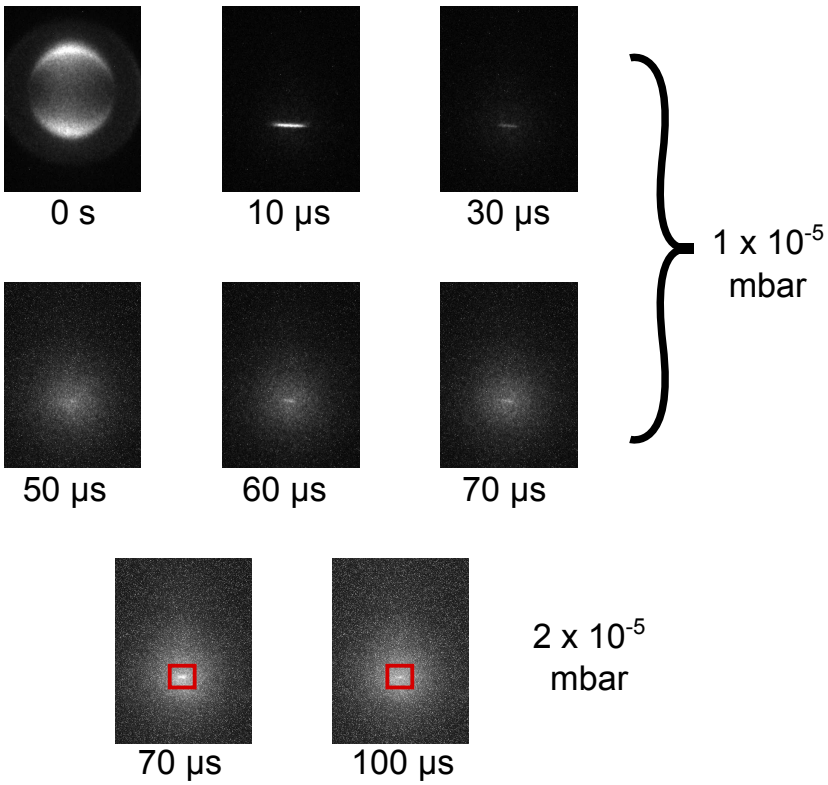

Figure 3.17: The results of the testing of the Oxford apparatus. The pressures on the right-hand side are the running pressures of the source chamber during the experiment. In the lowest two images, the zero-velocity signal has been highlighted to differentiate it from the molecular beam signal.

3.6.2 Results

The aim of these experiments was to prove that the newly reconfigured apparatus in Oxford was equal to the task of stopping bromine atoms. Therefore, the objective was to prove that atoms remained in the laser focal region for at least 100 μs. The results proved to be similar to those seen in the Durham experiment (see figure 3.17, and section 3.3), at least visually.

The velocity-map images show that the atoms can be stopped using the photolysis equipment available in Oxford, but that the signal at long delay times is heavily obscured by the signal generated from background gas in the main chamber. Ideally, these two signals should be separated. Since they have largely different velocities along the detection axis, they will have different times-of-flight to the detector, even if their perpendicular velocities are both centered on zero.

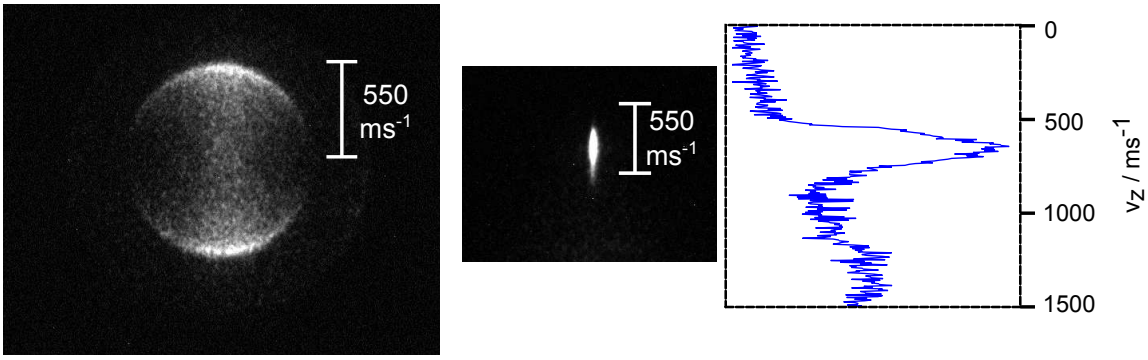

Figure 3.18: A comparison of the ion image rings at 457 nm dissociation, left, to the molecular beam velocity spread, centre. The crush profile of the molecular beam along the z-axis is also shown, right. Just from the ion image, we can see that the molecular velocity distribution is much broader than would be expected from a well cooled supersonic expansion. The scales in the two images account for the different velocity-to-pixel calibrations between the Br^+ and $Br_2{}^+$ cases.

Calibration

Using the velocity-map calibration technique as utilised in the previous experiments (sections 2.4.4 and 3.2.2), we can readily determine the temperatures of the Br atoms in the apparatus. The velocity to pixel ratio for the bromine ions is 5.14 ms^{-1}/pixel, and this equates to a Br_2 ratio of 3.63 ms^{-1}/pixel, giving our molecular beam velocity as 549 ms^{-1}. However, a noticeable problem manifested when calculating the beam speed from the ion image of the $Br_2{}^+$ ions; the velocity spread appears to be very broad, much broader than would be expected from a supersonic expansion (see figure 3.18). It is plausible that the high level of signal in the velocity-map image may be leading to some blurring from a Coulomb explosion of the ions (many ions formed simultaneously repel one another via Coulomb repulsion), or we may indeed just have an imperfect expansion under the new set-up. It is possible that the corrosion of the general valve as observed in section 3.6.1, is leading to a less than optimal expansion of the bromine gas.

Wavelength dependence

As in all iterations of the Photostop experiment, the tuning of the dissociation wavelength changes the excess energy provided to the system, in turn changing the

velocity at which the atoms can be stopped. It was noted during the course of the experiment, that the overall 'stopped' signal changed little over the range of the dye curve for Coumarin 460. This was rather disconcerting, since the velocity cancellation conditions are very strict when concerning the fragment energies. Stopped signal could be seen for dissociation from 455–475 nm, an increase in the excess energy of around 1000 cm^{-1}, which would seem to be highly counterintuitive.

However, as seen in section 3.6.2, the velocity spread of the molecular beam is feasibly much greater than we may have originally predicted, and hence it is likely that there is an opportunity to velocity cancel a subset of the atoms at a variety of dissociation wavelengths. This is illustrated in figure 3.19, in which Gaussian approximations to the molecular beam spread have been plotted for a variety of standard deviations, σ_z, assuming a molecular beam velocity of 549 ms^{-1}, as calculated for a mixture of Ar and Br_2. The widest of these Gaussians is constructed using the σ_z as calculated in section 3.6.2 of 62 ms^{-1}. It can be seen that the spread of the molecular velocities easily encompasses the corresponding range of photolysis wavelengths produced by the dye curve, illustrated by the dotted lines. These lines indicate the velocities at which you would expect velocity cancellation to occur, for the given photon energies. If the molecular beam velocity distribution is indeed this broad, then that would explain our apparent insensitivity to dissociation wavelength. The other curves are added to show what may happen if we had a beam spread ranging from the measured case, $\sigma_z = 62$ ms^{-1}, to the black line, $\sigma_z = 20$ ms^{-1}, corresponding to the expected velocity spread from a supersonic expansion.

Clearly, the way to be certain of this is to narrow the velocity distribution in the dissociation volume, either by some form of velocity selection with the nozzle set-up, or by improving the supersonic expansion source.

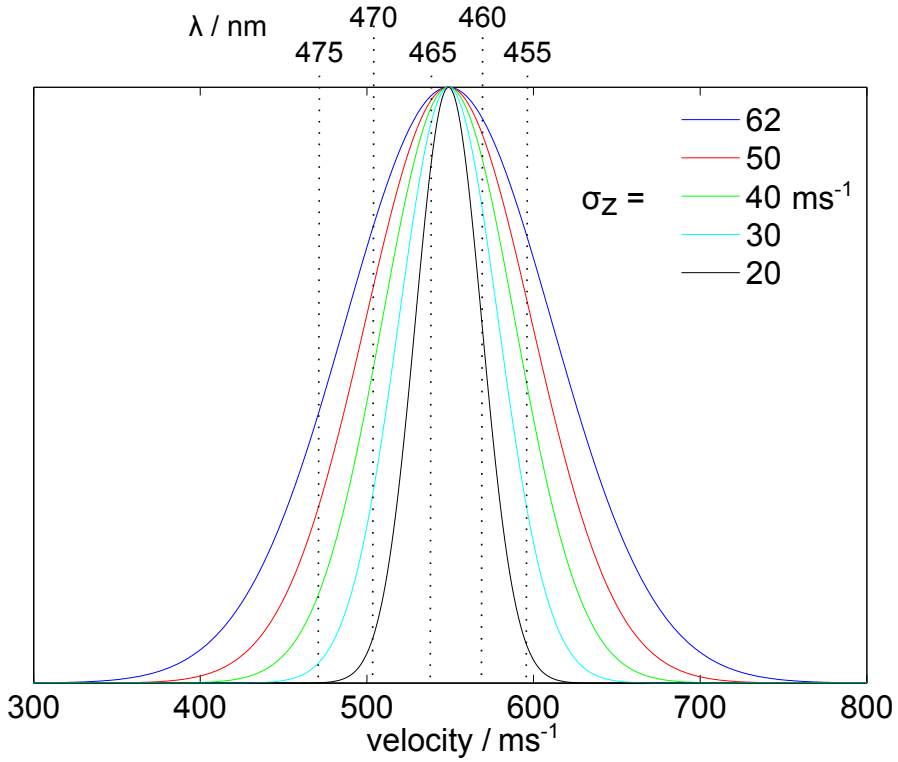

Figure 3.19: A plot of various possible velocity spreads within the molecular beam. Whilst effective internal cooling for the molecular beam should reduce the velocity spread to something on the order of the black Gaussian, analysis shows that we may in fact have a much broader set of velocities than we first imagined, leading to a lack of sensitivity to the wavelength of the dissociation laser.

3.7 Conclusions

This work has demonstrated that the Photostop technique works exceedingly well for cold atom production when compared to the molecular case. This is attributed primarily to the reduction in competing channels which will not lead to velocity cancellation; that is, in the absence of product rotational and vibrational states. In the case of the bromine atoms, we need only consider the product spin-orbit state branching ratio, over which we can exert some control by careful selection of the dissociation wavelength [17].

We have shown via the powerful velocity-map imaging technique, that the velocity distribution of the detected ions is on the order of a few Kelvin at the longest delay times, and the simulations point to an underlying atomic velocity distribution that is in the milliKelvin regime (see table 3.2). The data can be simulated in a relatively straightforward manner, and point to number densities of the atomic sample of being on the order of 10^8 cm^{-3}. This is of a magnitude that may be viable for cold chemical reactive studies.

Bibliography

[1] N. Vanhaecke, U. Meier, M. Andrist, B. H. Meier, and F. Merkt, Phys. Rev. A. **75**, 031402 (2007).

[2] E. Narevicius, A. Libson, C. G. Parthey, I. Chavez, J. Narevicius, U. Even, and M. G. Raizen, Phys. Rev. A. **77**, 051401 (2008).

[3] D. G. Fried, T. C. Killian, L. Willmann, D. Landhuis, S. C. Moss, D. Kleppner, and T. J. Greytak, Phys. Rev. Lett. **81**, 3811 (1998).

[4] C. C. Bradley, J. G. Story, J. J. Tollett, J. Chen, N. W. M. Ritchie, and R. G. Hulet, Opt. Lett. **17**, 349 (1992).

[5] E. L. Raab, M. Prentiss, A. Cable, S. Chu, and D. E. Pritchard, Phys. Rev. Lett. **59**, 2631 (1987).

[6] G. Modugno, G. Ferrari, G. Roati, R. J. Brecha, A. Simoni, and M. Inguscio, Science **294**, 1320 (2001).

[7] P. S. Jessen, C. Gerz, P. D. Lett, W. D. Phillips, S. L. Rolston, R. J. C. Spreeuw, and C. I. Westbrook, Phys. Rev. Lett. **69**, 49 (1992).

[8] C. Salomon, J. Dalibard, W. D. Phillips, A. Clairon, and S. Guellati, Europhys. Lett. **12**, 683 (1990).

[9] S. N. Atutov, R. Calabrese, V. Guidi, B. Mai, E. Scansani, G. Stancari, L. Tomassetti, L. Corradi, A. Dainelli, V. Biancalana, et al., J. Opt. Soc. Am. B **20**, 953 (2003).

[10] S. Willitsch, M. T. Bell, A. D. Gingell, and T. P. Softley, Phys. Chem. Chem. Phys. **10**, 7200 (2008).

[11] K.-K. Ni, S. Ospelkaus, M. H. G. de Miranda, A. Pe'er, B. Neyenhuis, J. J. Zirbel, S. Kotochigova, P. S. Julienne, D. S. Jin, and J. Ye, Science **322**, 231 (2008).

[12] J. M. Bakker, M. Stoll, D. R. Weise, O. Vogelsang, G. Meijer, and A. Peters, J. Phys. B **39**, S1111 (2006).

[13] J. Kim, B. Friedrich, D. P. Katz, D. Patterson, J. D. Weinstein, R. DeCarvalho, and J. M. Doyle, Phys. Rev. Lett. **78**, 3665 (1997).

[14] R. Chen, J. F. McCann, and I. Lane, J. Phys. B **40**, 1535 (2007).

[15] L. Rutherford, I. C. Lane, and J. F. McCann, J. Phys. B **43**, 185504 (2010).

[16] P. C. Samartzis, T. N. Kitsopoulos, and M. N. R. Ashfold, Phys. Chem. Chem. Phys. **2**, 453 (2000).

[17] M. J. Cooper, E. Wrede, A. J. Orr-Ewing, and M. N. R. Ashfold, J. Chem. Soc., Faraday Trans. **94**, 2901 (1998).

[18] T. G. Lindeman and J. R. Wiesenfeld, J. Chem. Phys. **70**, 2882 (1979).

[19] P. Atkins and R. Friedman, *Molecular Quantum Mechanics* (OUP, 2005).

[20] M. Brouard and C. Vallance, *Tutorials in Molecular Reaction Dynamics* (Royal Society of Chemistry, 2010).

[21] J. E. Sansonetti and W. C. Martin, J. Phys. Chem. Ref. Data **34**, 1559 (2005).

[22] R. Barrow, D. Broyd, L. Pederson, and K. Yee, Chem. Phys. Lett. **18**, 357 (1973).

[23] R. Donovan, A. Flexen, K. Lawley, and T. Ridley, Chem. Phys. **226**, 217 (1998).

[24] R. Barrow, T. Clark, J. Coxon, and K. Yee, J. Mol. Spectr. **51**, 428 (1974).

[25] O. P. J. Vieuxmaire, M. G. D. Nix, J. A. J. Fitzpatrick, M. Beckert, R. N. Dixon, and M. N. R. Ashfold, Phys. Chem. Chem. Phys. **6**, 542 (2004).

[26] A. A. Passchier, J. D. Christian, and N. W. Gregory, J. Phys. Chem. **71**, 937 (1967).

[27] G. Scoles, *Atomic and Molecular Beam Methods* (OUP, New York, 1988).

[28] S. DePaul, D. Pullman, and B. Friedrich, J. Phys. Chem. **97**, 2167 (1993).

[29] M. S. Elioff, J. J. Valentini, and D. W. Chandler, Science **302**, 1940 (2003).

[30] W. G. Doherty, M. T. Bell, T. P. Softley, A. Rowland, E. Wrede, and D. Carty, Phys. Chem. Chem. Phys. **13**, 8441 (2011).

[31] S. J. Matthews, S. Willitsch, and T. P. Softley, Phys. Chem. Chem. Phys. **9**, 5656 (2007).

[32] A. T. J. B. Eppink and D. H. Parker, Rev. Sci. Instr. **68**, 3477 (1997).

[33] S.-M. Wu, Ph.D. thesis, Radboud University Nijmegen (2007).

[34] Y. Jee, M. Park, Y. Kim, Y. Jung, and K. Jung, Chem. Phys. Lett. **287**, 701 (1998).

Chapter 4

Design of the magnetic trap

4.1 Introduction

Whilst the creation of cold bromine atoms is a step forward, it is difficult to perform experiments on a free cloud of atoms, however slowly they are moving. Therefore, the ideal solution would be to confine the cold atoms spatially, as considered in chapter 1. As with any method of creating cold atoms, the overall number densities are low, meaning that in order to progress the Photostop technique into a useful route to cold reactive chemistry, we need to increase the interaction times, which can only be achieved by moving to a regime where the atoms are spatially confined. To successfully confine the atoms, we require a 3-dimensional trapping field. However, we also need optical access and an ion ejection route for detection.

4.1.1 Bromine magnetic moment

The bromine atom energy levels will split into Zeeman states under the influence of a magnetic field. The ground state bromine atom will split into four states since it has $J = 3/2$. These m_J states can be classified as either high- or low-field seeking states, depending on whether they are attracted to or repelled by a magnetic field. Figure 4.1 shows the effect of the magnetic field upon these states. The blue line shows the Zeeman shift of the simple form shown in equation 4.1.

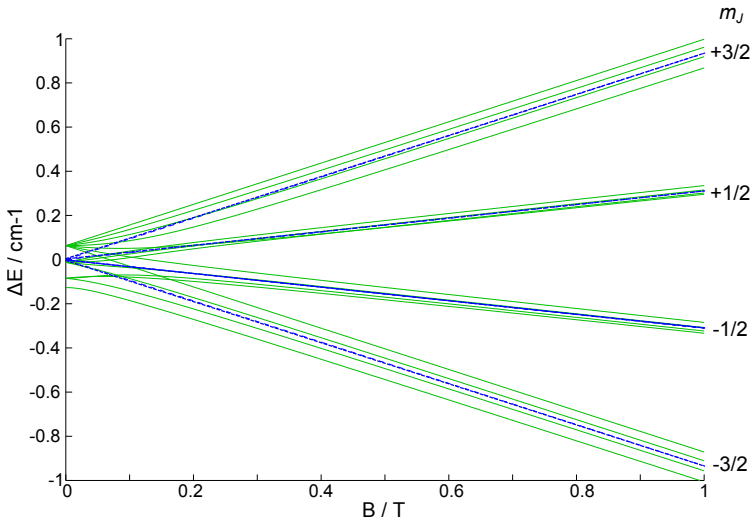

Figure 4.1: The effect of a magnetic field upon the m_J states of the ground state ^{79}Br atom. The blue dotted lines are the simple linear splitting of the states, and the green solid lines show the full hyperfine splitting from coupling to the nuclear spin.

$$\Delta E = g_J m_J \mu_B |B| \tag{4.1}$$

The green lines show the calculated energies when including the coupling of the nuclear spin with the total angular momentum to give the hyperfine states, as calculated for ^{79}Br [1]. There are 3 hyperfine states at zero-field, but this splits into 16 m_F states when a magnetic field is applied. That the calculation is explicitly for the ^{79}Br atom alludes to the fact that we will, in fact, be stopping both isotopes of bromine. There is a small difference between the hyperfine coupling constants of the two isotopes, in addition to the differing masses. The broad picture is that although there will be minimal difference between the two isotopes, but the heavier atom will be slightly harder to trap, purely because of the mass effect; the difference in the Zeeman shift is negligible.

The other point of note here is that the calculation has been explicitly performed for ground state ($^2P_{3/2}$) bromine. The procedure will simultaneously halt the excited Br* $^2P_{1/2}$ state, since it has an identical mass. This state will only split into m_J states of $\pm$ 1/2, of which, the high-field seeking state, $m_J = +1/2$, will be considerably less effectively confined than the ground state atoms $m_J = +3/2$ level. As such,

in calculations of trappable atoms, the excited state atoms have been completely neglected. It is therefore unclear what the effect that atoms with a large amount of electronic energy will have upon the others. It is assumed in this instance, that the atoms will be so poorly trapped that they will vacate the magnetic region in the same manner as in the regular ballistic expansion case. Indeed, all calculations have been run to only include the Br $^2P_{3/2}$ $m_J = +3/2$ state atoms, due to their experiencing the greatest restrictive magnetic field gradient.

4.2 Trap design

Clearly, since the atom exhibits a Zeeman shift in its ground electronic state, it would be desirable to use this to confine it spatially. Considerable amounts of design work had to be done to ensure the optimum fields in the current experimental arrangement, whilst still being able to image the ions produced from trapped atoms.

4.2.1 Trapping geometries

It was quickly decided that the most effective method to generate trapping fields would be to use permanent magnets in the magnetic trap. Unless superconducting magnets were to be used (which would only be viable once cooled to very low temperatures) it would be difficult to generate a magnetic potential deep enough to confine bromine atoms with the velocities that we generate. Magnetic fields generated by current-carrying wires create very shallow traps, and although the field can be switched off, such traps are only viable for the very coldest species. Whilst permanent magnets cannot be switched off, they will be the most direct route to insertion of a magnetic field inside the velocity-mapping region. Neodymium Iron Borate (NdFeB) magnets have the highest available remanent magnetic field strength (Arnold Magnetics: `http://www.arnoldmagnetics.com`) and were chosen as the magnetic material. Various configurations were considered along with their relative merits. Evidently the best configuration from the view of the magnetic

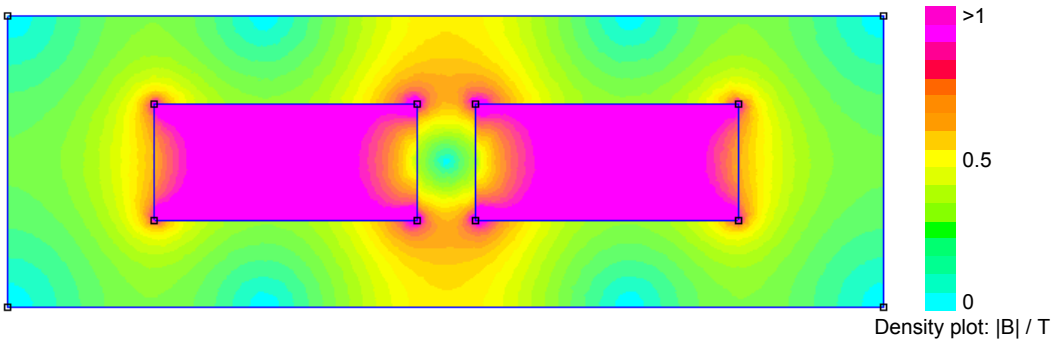

Figure 4.2: Finite element method modelling of the proposed magnet setting. The two bar magnets are positioned so as to point north to north. The field strength is shown by the colours: pink/red indicates regions of high field, blue/green regions of low field.

field would involve building a 3-dimensional trap, with magnets along each axis. However, such an arrangement would limit the extraction of ions. If we were probing a species that could be detected using LIF as opposed to REMPI, then a magnetic trap with a more uniform field, such as one created by a higher order multipole set-up, may be worthwhile. The requirement for extracting bromine ions means that the best solution for our experimental conditions would involve plenty of physical access. Hence the simplest solution was to use a pair of NdFeB magnets facing north-to-north. The exact configuration was a subject of much consideration. The most straightforward possibilities were ring magnets or bar magnets, at a given separation. Magnetic field strength was one consideration, as was optical access. Two ring magnets would give a more spherically symmetric field, whereas the bar magnets would allow for a more straighforward laser alignment procedure, as well as being more easily mounted into the apparatus. The latter concern turned out to be the critical factor in choosing the initial magnet design. A pair of $2 \times 4 \times 10$ mm cuboidal NdFeB magnets were inserted into the apparatus end-on to one another, at a separation of 2 mm. To simulate the magnetic field, an open source finite element analysis program, FEMM [2] was used (the result is shown in figure 4.2). Finite element analysis is used to find the approximate solutions to partial differential

equations, in this case, Maxwell's equations:

$$\Delta \times \mathbf{H} = J, \tag{4.2}$$

$$\Delta \cdot \mathbf{B} = 0, \tag{4.3}$$

$$\mathbf{B} = \mu_0 \mathbf{H}, \tag{4.4}$$

where $\mathbf{H}$ is the magnetising field, J is the total current density, $\mathbf{B}$ is the magnetic field and μ_0 is the magnetic constant, or permeability of free space. Equation 4.4 is only valid for a linear magnetic material, i.e. the relationship between $\mathbf{B}$ and $\mathbf{H}$ is linear. If this were not the case, we would replace μ_0 with $\mu(\mathbf{B})$. Luckily, NdFeB magnets are very well behaved under normal temperature conditions, and are as close to linear as can be commercially bought. This simplifies the magnetic field calculations.

Most finite element analysis tools use a magnetic vector approach, whereby the flux density is written in terms of a vector potential, $\mathbf{A}$:

$$\mathbf{B} = \Delta \cdot \mathbf{A}, \tag{4.5}$$

which allows equation 4.2 to be rewritten as:

$$\frac{1}{\mu_0}\Delta^2 \times \mathbf{A} = J. \tag{4.6}$$

It is equation 4.6 which can then be solved. The main advantage of the finite element technique is that it treats the boundary conditions of magnetic problems very robustly, concentrating its computational resources in these problematic areas. The calculations have been performed assuming a uniform magnetic field strength over the surface of the magnets, and ignoring any effects of the external field on the interior of the NdFeB, such as hysteresis [3].

The limiting boundaries are at $(x, z) = (0, 0)$ and $(y, z) = (0, 0)$, where saddle

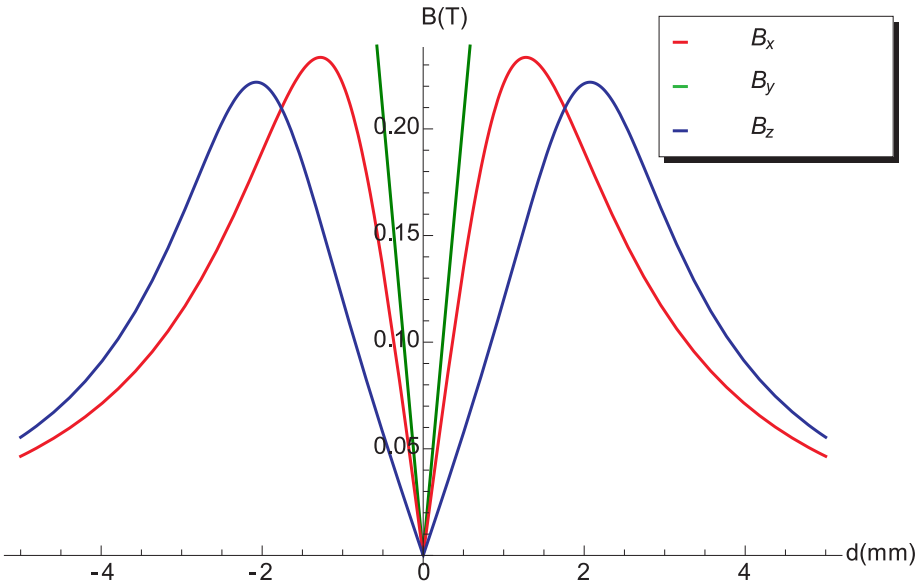

Figure 4.3: Plot of the magnetic field strength along the $x-$, $y-$ and $z-$axes, in each case setting the other two axial positions to zero. The magnets are positioned along the $y-$axis.

points in the magnetic field are formed, as can be seen in figure 4.3. The magnetic fields have linear gradients within the $2 \times 4 \times 2$ mm region between the two magnets, however, the closer the magnets are to one another, the larger the potential at the saddle point. It can be seen, that with the unequal axial lengths of the bar magnets, the magnetic field gradient is different in all three directions. When a limiting trap depth is calculated (approximately 0.2 T), the resulting isosurface is highly ovoidal (figure 4.4). This can now be defined as the confining volume of the trap, the volume in which we will consider atoms below a certain energy to be trapped. We can visualise this fraction as a percentage of the fragments that are ejected in the photolysis process. In figure 4.5, the atoms with a velocity lower than the maximum allowable for confinement have been circled, giving an idea of how many of the atoms can be trapped per pulse. This fraction, purely from a kinetic energy perspective, is around $2{\times}10^{-5}$, corresponding to a velocity of no more than 8 ms^{-1}, or a maximum trapped temperature of 300 mK (using $\frac{1}{2}mv^2 = k_{\mathrm{B}}T$). Factoring in the random assignment of the individual m_J states, only a quarter of these will be trappable, in addition to half of the atoms being created in the

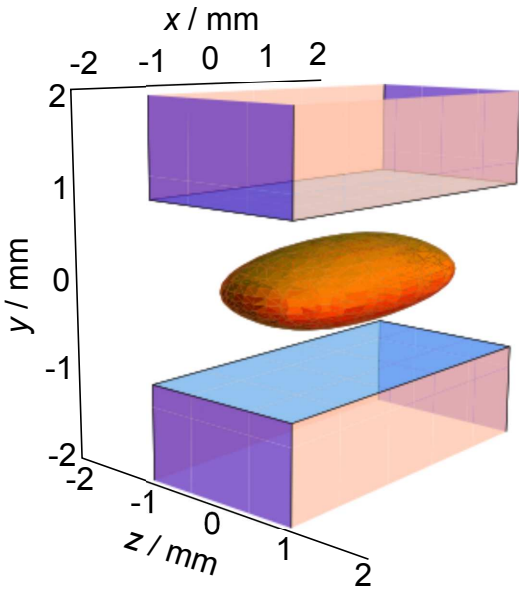

Figure 4.4: The isosurface of 0.2 T within the space between the magnets, orange. This is defined from here on to be the trapping volume.

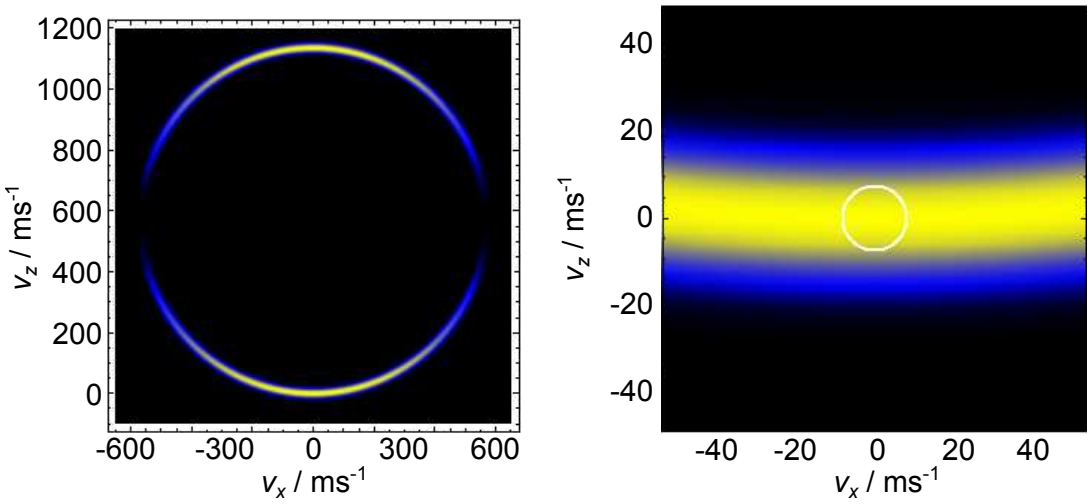

Figure 4.5: Left: a slice through the Newton sphere for the bromine photolysis process, showing the LF velocities of the atoms. Right: a close-up centered around zero-velocity. Atoms that with a velocity less than $v_{\max}$, the maximum velocity that can be confined in the trap, are circled.

$^2P_{1/2}$ excited state. This leaves a trappable fraction of around 2.5×10^{-6} atoms per pulse. With a conservative molecular beam density of bromine around 10^{12} molecules cm^{-3}, this should still yield densities in excess of 10^6 atoms cm^{-3}, assuming 100% photodissociation efficiency.

The effect of the trap is best illustrated by figure 4.6. With the magnetic fields included, the atoms do not vacate the trapping region and are forced back to the field origin ($x, y, z = 0$). This can be seen in the images on the left hand side at 250, 500, 750 and 1000 μs. In the case of no magnetic fields, the atoms are free to expand, and diffuse out of the trapping volume. This should manifest itself experimentally; the accummulated density in the trapping region should give us a higher signal at long delay times.

4.3 Extraction optics

Evidently, the main issue with inserting anything into the ion optics region will be the extra difficulty with extraction of ions. Ideally, we would want to disrupt the standard VMI plate setting as little as possible. LIF is not possible for bromine atoms, so the ion detection scheme must be maintained. In figure 4.7, we can see some early designs for the trap mounting. In each case the lighter more central items are made of polyether ether ketone (PEEK), a non-conductive material selected so as not to disrupt the extraction fields around the magnets (the two black blocks in each schematic). In the upper case, the entire region between the plates would be filled with PEEK for ease of attachement to the outer ion optics mounts. The magnets would be sandwiched between the two PEEK spacers, and a shallow channel would be milled into the PEEK to allow laser access. This plan was discarded on grounds of cost.

In the lower schematic in figure 4.7, a much smaller amount of PEEK is used, to save on costs, but a new pair of extractor and repeller electrodes would have to be made in order to effectively clamp the PEEK mount in place around the magnets.

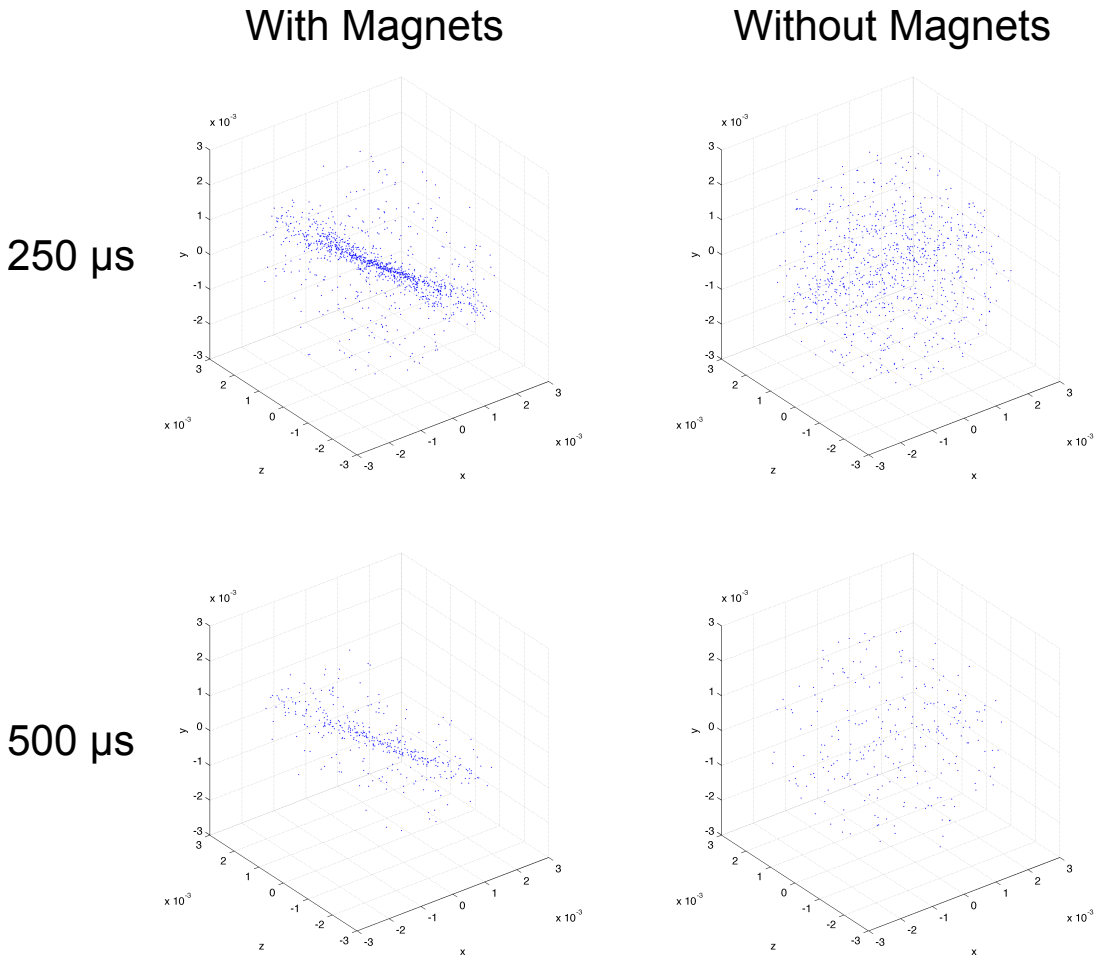

Figure 4.6: Monte Carlo simulated trajectories of bromine atoms in the trapping volume over the course of 500 μs, both with and without magnetic fields. The magnet case (left column) shows the constraining of the atoms with low kinetic energy, whereas in the non-magnetic case (right column), normal ballistic expansion occurs.

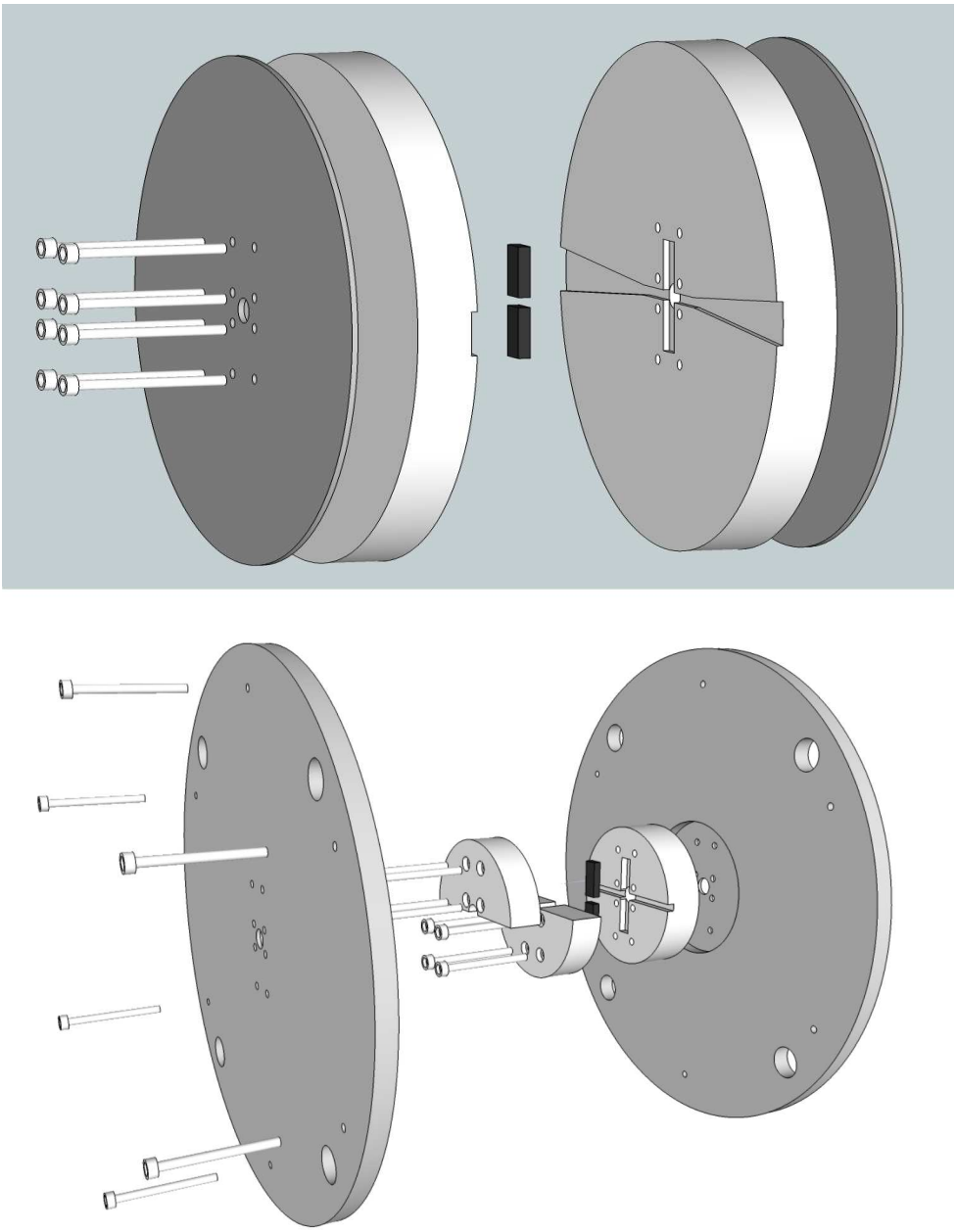

Figure 4.7: Schematics of possible PEEK spacer designs, magnets shown in black.

The top PEEK section would be cut into two so that only one magnet at a time needed to be clamped, making magnet insertion more straightforward. The top and bottom sections of the PEEK mount would be held together with eight plastic bolts, which would clamp directly onto the repeller plate. Both repeller and extractor would have a recess milled into the surface to centre the magnets in the electrode stack, and the two electrodes could be clamped together with six more plastic bolts in order to hold them parallel to one another. The whole repeller-extractor section could then be put into the electrode mounting as one.

Figure 4.8 shows the final attempted design for the PEEK spacer, attached to the repeller plate. From an engineering perspective, it was simplest to use a cuboidal block of PEEK from which to create the spacer, hence the change in design from figure 4.7. The image shows the extra adaptation to the design over the schematic; in the original plans, it was assumed that the magnets would automatically charge to the intermediate voltage of the repeller and extractor plates. Consultation with the electronics workshop suggested connecting the plates resistively, with a 1 MΩ resistor between the magnets and each of the plates, connected by copper shims inserted around the PEEK. This would ensure that we could be certain of the voltage of the magnets for simulation purposes. The path through the trap centre can be seen in figure 4.9. Clearly, overlapping the lasers would be tricky, but possible due to the small area of acceptance for laser passage.

The major issue with this design proved to be a fault with using PEEK itself; the plastic began to charge up when struck by the lasers or charged particles perhaps, disrupting the extraction of the ions, and signal would disappear at random intervals. PEEK would have to be removed from the design of the extraction optics. Therefore, the only way of mounting the magnets would be with an extra electrode plate, in between the repeller and extractor plates, with a separate power supply. From here onwards, this plate will be referred to as the magnet plate.

The next design to be tested was a very simple attachment of the magnets to

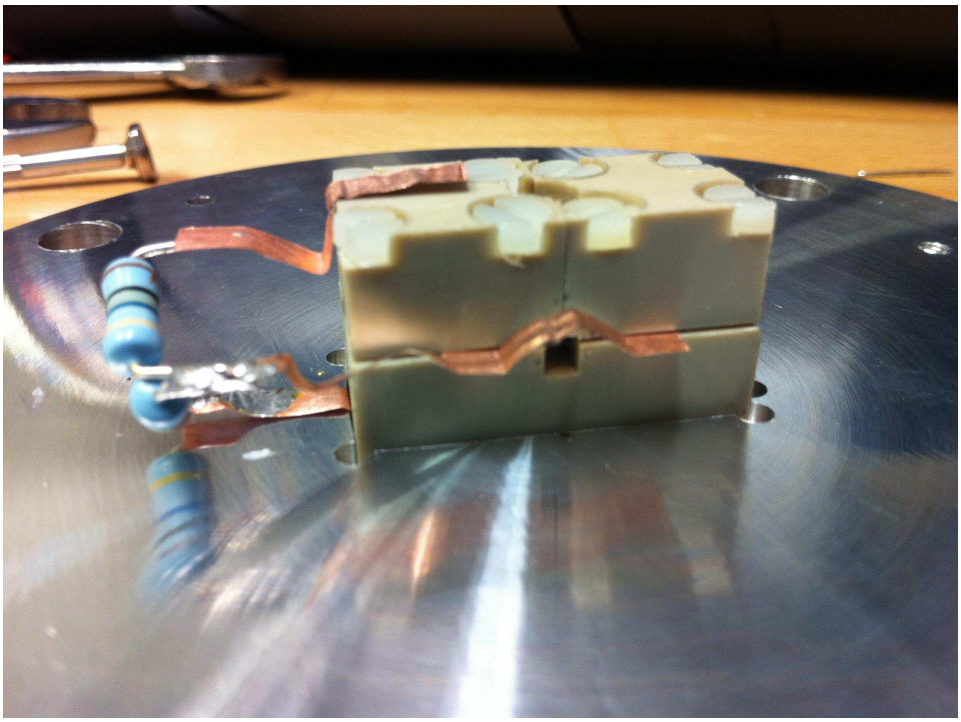

Figure 4.8: Photograph of the final design for the PEEK spacer, with magnets inserted. Resistors were added to the design to attempt to position the magnets at an intermediate voltage to the extractor and repeller plates. This is essentially a rectangular version of the lower panel in figure 4.7.

an existing plate; an epoxy resin (Araldite) was used to glue the magnets to the surface of the plate, and electrical connections were formed to the magnet surface with conductive tape (see figure 4.10. This too proved to be experimentally unsuccessful, albeit for a different reason. Alignment of the lasers into the magnet region was hampered by the proximity of the magnets to the surface of the electrode, thus causing a large amount of scattered laser light, often towards the detector, in addition to photoelectrons being ejected from the surface of the electrode. Although this did not damage the MCPs, it was a substantial risk to take. Glueing the magnets to the surface was also something of a challenge, since the repulsion of the magnets from one another whilst the resin set required unusual clamping configurations in order to prevent the clamp from becoming stuck to the electrode. In short, this design is not recommended for anything other than quick testing purposes, since it is relatively easy to implement into existing apparatus. It should also be noted that at our vacuum pressures, $\sim 10^{-7}$ mbar, there was no noticeable outgassing effect

Figure 4.9: Photograph of the full ion optics stack with PEEK spacer. The path that the laser beam takes through the centre of the trap is clearly visible.

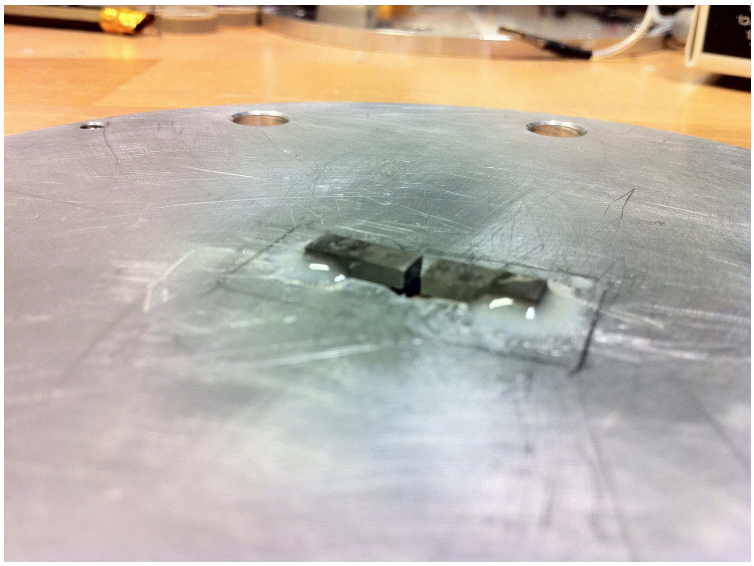

Figure 4.10: Photograph of the electrode with the magnets attached, affixed with 2-part epoxy resin.

from the resin, although one might be dubious about trying this sort of test in a very high vacuum situation.

All things considered, another design was required. A compromise between the two previous designs was eventually decided upon. Clearly, the magnets needed to be away from the surface of their mounting electrode to aid laser alignment, but the mounting blocks needed to be constructed out of an electrical conductor. However, from SIMION simulations [4], the protruding blocks required to mount the magnets would warp the extraction fields, making it near impossible to detect the ions. So, a novel plate with a deep channel was designed (Figure 4.11). This plate would not be compatible with a velocity-map image set-up. However, the notation used in this thesis will refer to the ion optics stack in terms of the repeller and extractor plates, which are carried over from the velocity-mapping set-up. The new plate, which was installed in between the repeller and extractor plates, is referred to as the magnet plate. No further imaging studies were carried out after the installation of this new electrode.

The final plate was built in the Oxford Physical and Theoretical Chemistry Laboratory student workshops, and included irises on the plate itself for ease of alignment

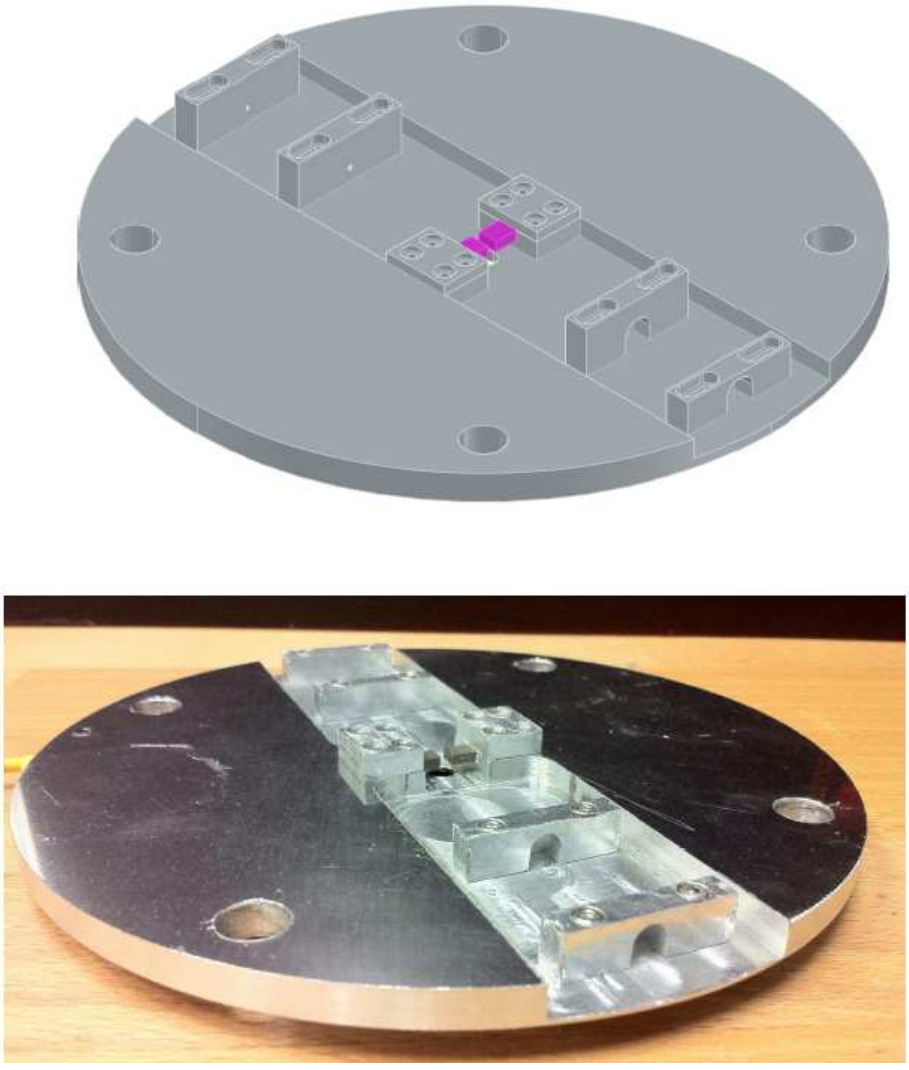

Figure 4.11: Top: schematic of the magnet plate prior to construction. Bottom: photograph of the final plate on the bench.

through the centre of the magnets. These 'doghouse' irises were designed so as to attempt to avoid scattering of stray beams towards the trap centre, thus attempting to minimise any detection of background species, in addition to protecting the detector from wayward beams. The iris holes were drilled to be 0.5 mm in diameter, thus leaving very little leeway for misalignment. These irises sit in the deep channel cut into the plate to sit at the level of the magnets. There is a very small amount of adjustability in the possible positioning of the magnets to be able to adjust them if the laser will not pass through cleanly.

The magnets themselves are attached to the plate in recessed grooves, with extra metal blocks bolted onto the top to clamp them into place. This allows direct electrical contact with the plate, while positioning the magnets above the surface of the plate itself, aiding the alignment procedure. The new design was still susceptible to damage from the laser, if poorly aligned on the iris apertures (figure 4.12), so in the experiment itself, only the outermost two irises were actually used to keep light from scattering closer to the magnets, as well as to prevent the generation of photoelectrons close to the trap centre.

4.3.1 Ion detection from within the trap

The same detection scheme to that employed in the conventional velocity cancellation experiment can be employed. A (2 + 1) REMPI scheme was utilised to ionize the atoms, and electric fields were used to propel the ions towards the micro-channel plate detectors. However, the extraction process is less simple with the inclusion of the magnets and the insulating framework. There are new factors to consider; namely, the perturbing effect of the magnetic trapping field on the trajectories of the ions, and the effect of the presence of the electrically conductive magnets.

The electric fields for the new configuration were simulated in SIMION [4], using a cylindrically-symmetric potential array for the ion optics, and a higher-resolution, three-dimensional array for the magnet region. The smaller gridpoint size was used-

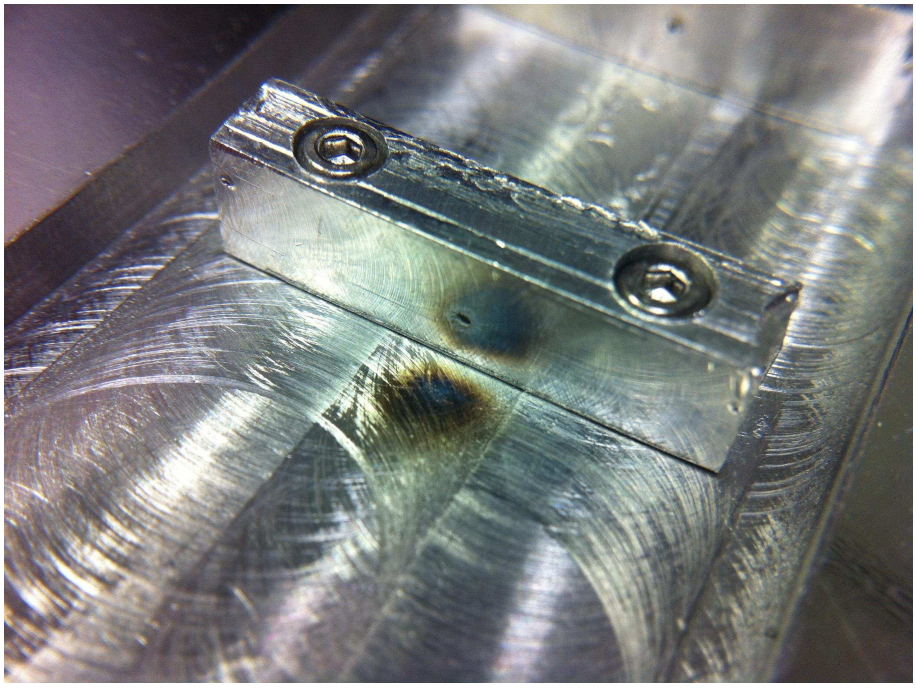

Figure 4.12: Laser damage to the electrode plate. Poor alignment could cause serious burns to the metalwork. Shown here is damage caused by reflection off of the back of one of the irises.

for the magnet region, since the asymmetry of the magnets had to be simulated fully in three dimensions to accurately obtain the ion trajectories. The simulated fields are shown in figure 4.13. There are several things to consider when attempting to accumulate density within the trap. We need to be sure that the new geometry within the electric field is not interfering with the extraction. For this we test the case where the magnetic field was absent, but the geometry of the magnets were still in place. To achieve this end, a pair of 'magnots' - aluminium blocks of identical size to the neodymium magnets - could be inserted into the magnet housing as a control.

4.3.2 Trap losses

If we stop a certain number of bromine atoms inside the trapping volume, with a kinetic energy that is below the trap depth, should we expect the atoms to remain in the magnetic region indefinitely? It is instructive to look at the avenues of loss

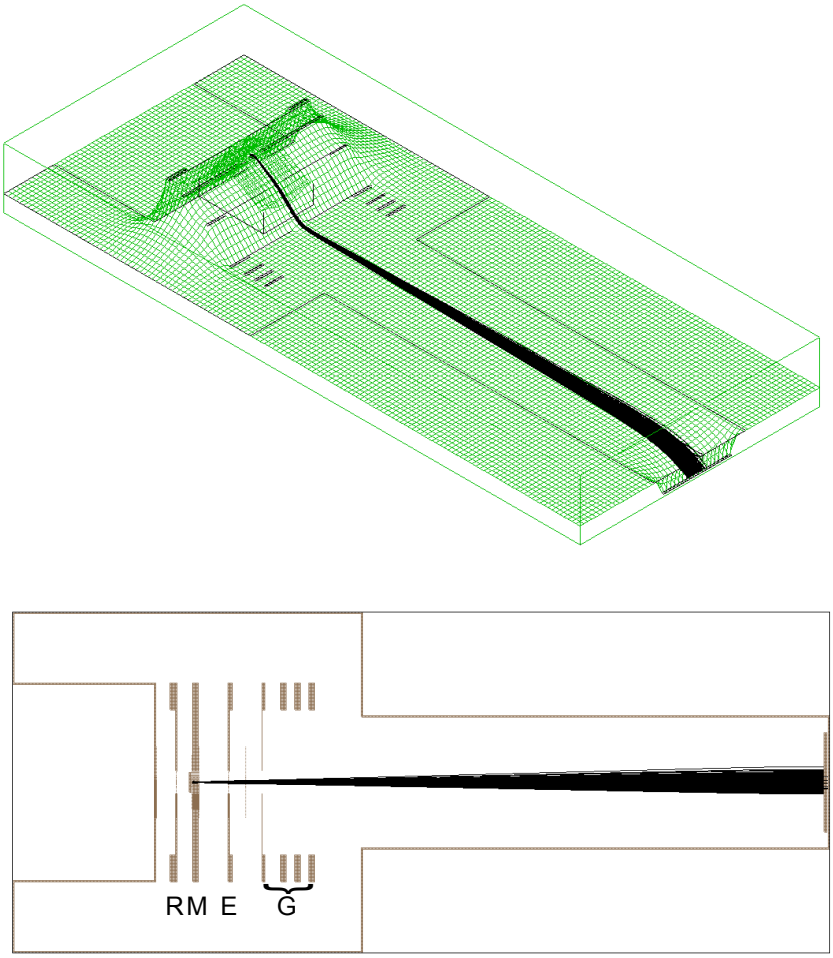

Figure 4.13: Main experimental chamber as simulated in SIMION. The upper image shows the potential gradient for the ion extraction as used in the experiment. Below is the schematic of the whole chamber. Multiple potential arrays of varying scales had to be combined to fully simulate the magnet region of the ion optics. R, M, E and G refer to repeller, magnet, extractor and ground plates respectively. Some trajectories for the ions, with positions and velocities generated in Matlab, are shown.

for trapped atoms. One could consider the possibility that the trapped atoms could collide with one another, and that such a collision could knock one or both of the atoms out of the trap. This can be considered a negligible source of loss for the trap, since the density of bromine atoms will be low, as well as the fact that trapped atoms will have a very low kinetic energy in the trap, making collisions unlikely to impart enough energy for trap loss to occur. So, what other possibilities are there?

Molecular beam collisions

The major problem with loading a trap directly inside the ion optics in the path of the molecular beam, is the barrage of carrier gas atoms (and, to a lesser extent, Br_2 molecules) from the beam that will likely knock most of the atoms out of the trap. The absolute number density in a molecular beam is a difficult number to determine experimentally with any degree of accuracy [5]. At the kind of distance (121 mm) from nozzle to laser focus in our experiment, there will be some significant divergence of the molecular beam, leading to a decrease in the number density downstream [6].

Background collisions

The vacuum in the main chamber is maintained by a turbo pump (Leybold Turbovac 600c), which keeps the pressure at approximately 1x10^{-7} mbar. Using the ideal gas equation:

$$pV = nRT, \tag{4.7}$$

we can calculate that this equates to 10^9-10^{10} molecules cm^{-3}. Considering basic collision frequency theory [7], the rate of collision will be linearly dependant upon the number densities of the sample which is trapped and the background gas. Since the background density is considerably less than that of the molecular beam, it seems sensible to ignore collisions with the background as a loss source, certainly in the short term. The vacuum is not Ultra-High Vacuum, unlike that used in many modern experiments, which can reach 10^{-10} mbar, and so the initial goal of

the trapping experiment will be to attempt to witness an increase in the signal remaning in the trap volume over the timeframe of the molecular beam pulse length and upwards. Subsequent experiments, if trapping can be shown to occur for 100 ms and above, i.e. the duration from one molecular beam pulse to the next, we may consider the background collision rate more thoroughly.

Majorana losses

Majorana losses occur when the atomic spin state is nonadiabatically changed, arising from a zero-point in the magnetic field [8]. Adiabatic motion occurs when following condition is met:

$$\omega_{\mathrm{L}} = \frac{\mu_{\mathrm{B}}\mathrm{B}}{\hbar} >> \left|\frac{\mathrm{dB}}{\mathrm{d}t}\right| \frac{1}{\mathrm{B}} = \left|\frac{\mathrm{dB}}{\mathrm{d}r}\right| \frac{v}{\mathrm{B}}, \tag{4.8}$$

where ω_{L} is the Larmor frequency, μ_{B} is the Bohr magneton, B is the magnetic field strength, t is time, and $v$is the velocity [9].

If an atom passes through the zero-field point, the adiabatic condition is violated, and the spin state can flip, and be the atom will be lost from the trap. This is pictured as a hole in the centre of the trap through which the atoms can escape.

There have been various attempts in the field of magnetic trapping to avoid Majorana losses. Time-Orbiting-Potential (TOP) traps [10] limit the exposure of the atoms to the zero-point by rotating the magnetic field potential, thus moving the zero-point spatially faster than the atoms themselves can move, so that the spins do not have time to respond to the presence of the field. Another option is to build a trap that has a non-zero magnetic field minimum, such as the Ioffe-Pritchard trap [11]. In this case, bias fields are applied to a quadrupolar field to create another trapping axis, but also raising the level of the potential minimum. A third option is to use a laser as an optical plug [12], whereby the laser field creates a repulsive potential around the zero-point in the centre of the trap, preventing the atoms from accessing the Majorana transition region.

In the case of velocity cancellation, Majorana transitions are assumed to be negligible compared to the collisional losses mentioned previously. Since the trap volume is much greater than the area in which Majorana flips could occur (in the case of Cs, the radius over which the zero-field may be an issue is of the order of 2 μm [9]), the atoms are unlikely to often be found in the lossy region. The energy separation between hyperfine states needs to be incredibly small for spin-flip to occur. Brink and Sukumar [13, 14] estimate that Majorana losses are near-negligible for microtraps for alkali metal BECs, which are considerably colder than the bromine atoms here, and are in much shallower traps. Hence, it will be valid to ignore the loss rate from Majorana transitions.

4.4 Prospects

The final magnetic trap design ought to provide us with a region in which the bromine atoms can be confined, assuming they are stopped below a certain velocity. The trap depth will not be able to confine as many atoms as previously considered in section 3.3.3. However, from finite element analysis of the magnetic fields, we ought to obtain a trapping depth of around 0.2 T, and trap a fraction of around 2.5×10^{-6} atoms per pulse, calculated from the Monte Carlo simulations. If this does indeed provide us with the calculated density of 10^6 atoms cm^{-3}, then we may well indeed be able to perform some collision experiments upon the sample with another species. The main obstacles are the likely sources of loss, which will have to be investigated experimentally. The critical advantage of this design of magnetic trap is that, since dissociation occurs within the magnetic field itself, the atoms do not have to be transferred from the point of velocity cancellation into an area of confinement. This implies, that although we may face losses due to collisions with the incoming gas pulse, there is the possibility of reloading the trap over many gas pulses, thus steadily accumulating cold atom density. This would be a major advantage in trying to overcome the effect of having a low number density of cold

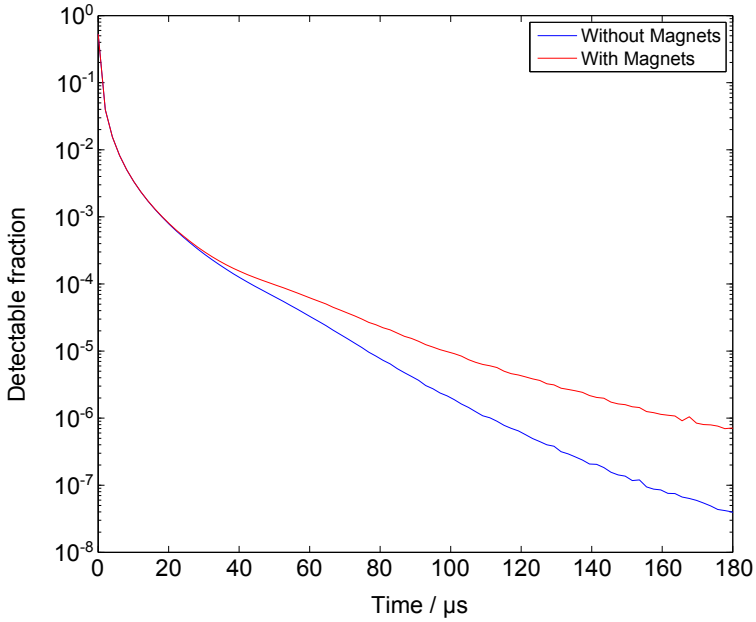

Figure 4.14: Short time delay decay curves for velocity cancellation under the conditions used in the Durham experiment, calculated in Matlab using a Monte Carlo technique [15].

atoms formed in each gas pulse.

Our main objective initially, ought to be an analysis of what difference we would expect to see between the cases with and without the magnetic fields. Clearly one thing we can look for is signal at very long delay times; if the magnetic trap works correctly, then the bromine atoms will not vacate the trapping region, but they will disappear in the 'magnot' case. As mentioned in chapter 3, we don't know the absolute detection efficiency of the Br ions, so at very low signal levels, as are expected for the longest delays, the difference in signal may not be obvious.

Alternatively, we can look at the relative differences in signal over the early part of the decay curve for the two cases. It is fairly obvious from the simulations shown in figure 4.14, that over the very shortest timespans, the decay curve is predicted to be identical for magnets and magnots. This is driven by the ballistic expansion of the fastest atoms, which will be barely perturbed by the magnetic fields. It is only after around 50 μs that any noticeable difference appears between the curves, when the slowest atoms which are affected by the magnets are reflected back by the field into the detection region. Clearly this implies that the ideal scenario would

be a trap which was well matched in size to the probe volume, since there would be minimal 'loss' from atoms which were in the trapping region, but spending very little time in the ionisation volume. This may not be achieveable, given that the ionisation is a REMPI process, therefore needing to be tightly focussed to achieve the necessary ionisation intensity. However, matching of the dissociation laser focal size to the trapping volume would be desirable, as it would be possible to stop at all poiints in the trap, thus limiting density loss from the atomic cloud expanding to fill the trap volume.

Bibliography

[1] H. H. Brown and J. G. King, Phys. Rev. **142**, 53 (1966).

[2] D. C. Meeker, *Finite Element Method Magnetics*, URL `http://www.femm.info`.

[3] R. Engel-Herbert and T. Hesjedal, J. Appl. Phys. **97**, 074504 (2005).

[4] D. A. Dahl, *SIMION 3D version 8.0*, URL `http://www.simion.com`.

[5] N. E. Schofield, D. M. Paganin, and A. I. Bishop, Rev. Sci. Instr. **80**, 123105 (2009).

[6] G. Scoles, *Atomic and Molecular Beam Methods* (OUP, New York, 1988).

[7] P. W. Atkins, *Physical Chemistry* (OUP, 2010), ninth ed.

[8] M. Lara, B. L. Lev, and J. L. Bohn, Phys. Rev. A **78**, 033433 (2008).

[9] V. Gomer, O. Harms, D. Haubrich, H. Schadwinkel, F. Strauch, B. Ueberholz, S. aus der Wiesche, and D. Meschede, Hyperfine Interactions **109**, 281 (1997).

[10] D. J. Han, R. H. Wynar, P. Courteille, and D. J. Heinzen, Phys. Rev. A **57**, 4114 (1998).

[11] D. E. Pritchard, Phys. Rev. Lett. **51**, 1336 (1983).

[12] D. S. Naik and C. Raman, Phys. Rev. A **71**, 033617 (2005).

[13] C. V. Sukumar and D. M. Brink, Phys. Rev. A **56**, 2451 (1997).

[14] D. M. Brink and C. V. Sukumar, Phys. Rev. A **74**, 035401 (2006).

[15] M. T. Bell, private communication.

Chapter 5

Magnetic trapping of bromine atoms

As discussed in chapter 4, bromine atoms are expected to be trapped in a magnetic field as a result of the Zeeman shifting of their atomic energy levels. This chapter will aim to demonstrate this experimentally.

5.1 Magnetic trap implementation

Performing the experiment in the perpendicular configuration proved that velocity cancellation could be achieved with the apparatus at hand, since velocity cancellation and velocity-mapping could be simultaneously realised. However, this meant that the experiment was not conducive for magnetic trapping, as originally imagined. The implementation of the magnetic holder, as described in section 4.2.1, prevented access to one of the axes, blocking what was originally the molecular beam axis. Hence the experiment had to be returned to its original configuration, as depicted in figures 5.1 and 5.2.

This alteration necessitates a change regarding the way the experiment is conducted; the velocity cancellation cannot be experimentally analysed by velocity-mapping. If the polarisation vector of the laser is pointed along the molecular beam

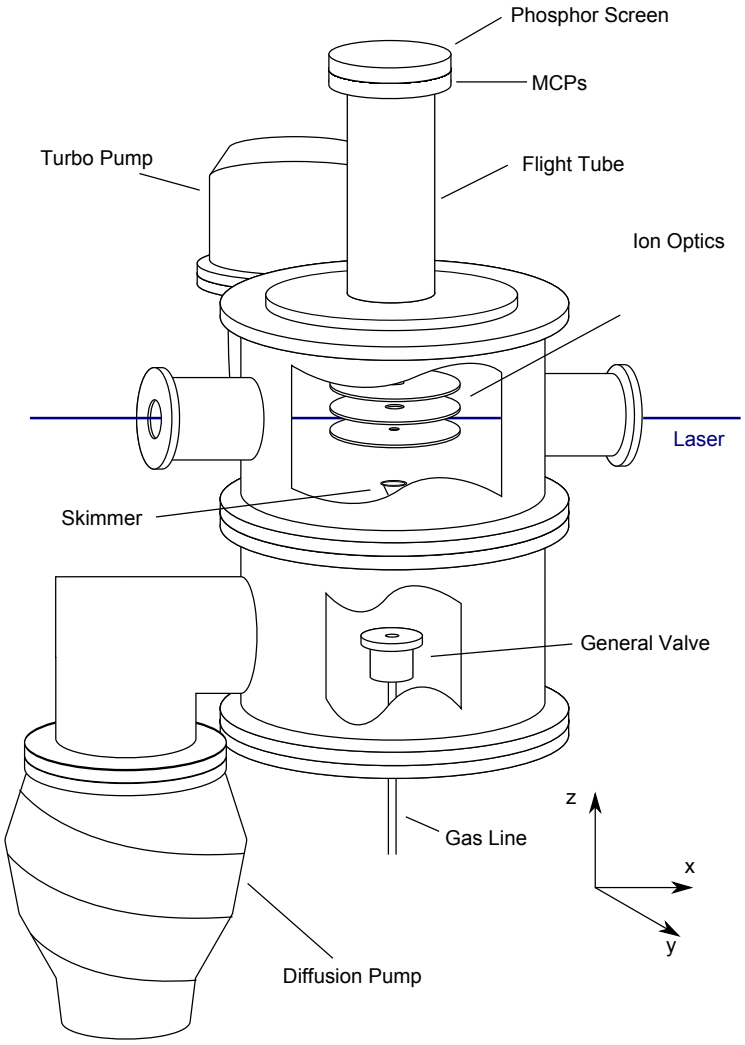

Figure 5.1: Schematic view of the experimental chambers used in the Oxford Experiment.

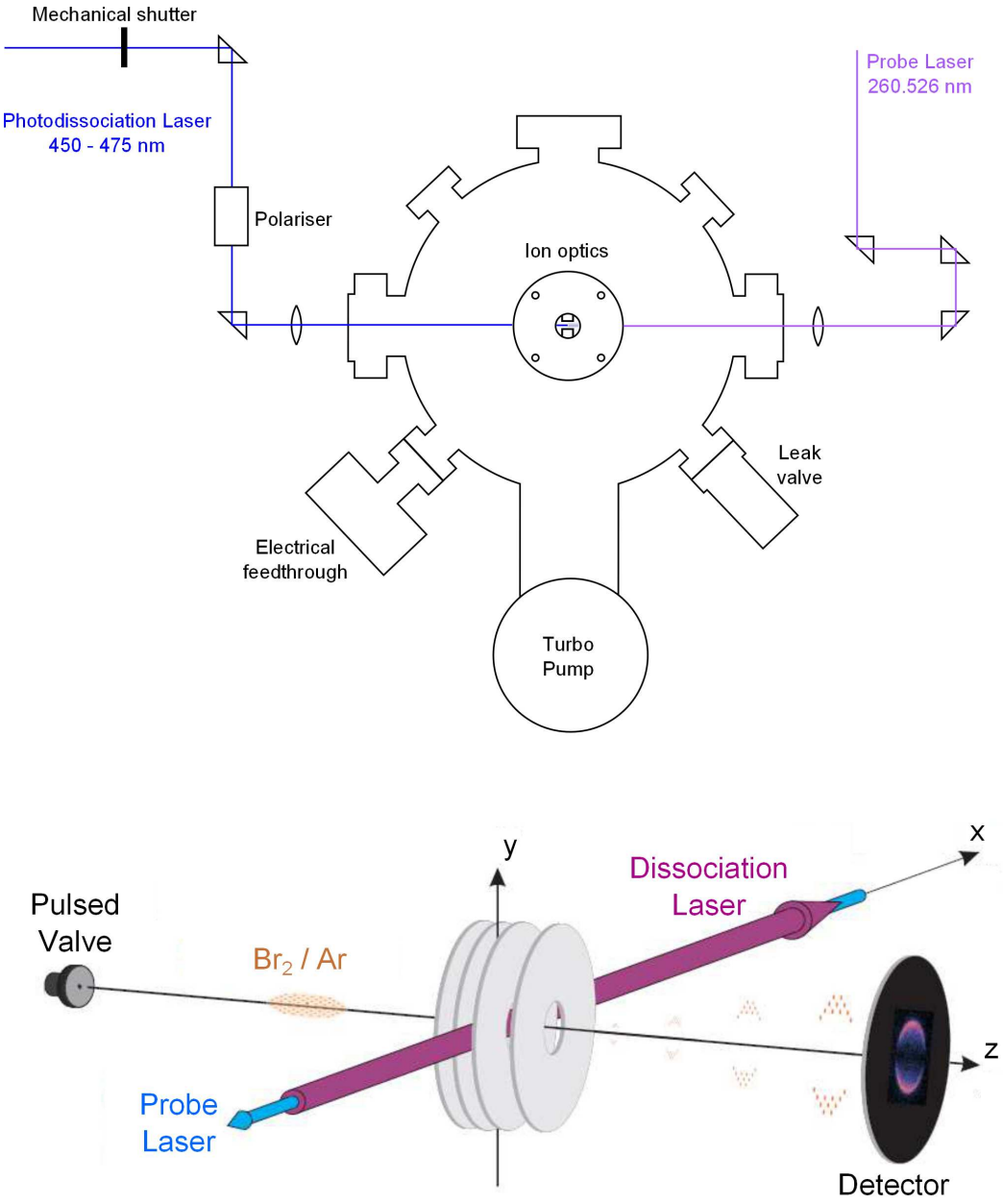

Figure 5.2: A schematic of the experiment including the magnet holder plate. The molecular beam is now co-linear with the detection apparatus, and is perpendicular to the plane of the upper diagram. The top image shows a schematic of the experimental apparatus as a whole, and the lower diagram is a representation of the modified ion optics, which would be pointed towards the reader in the upper image.

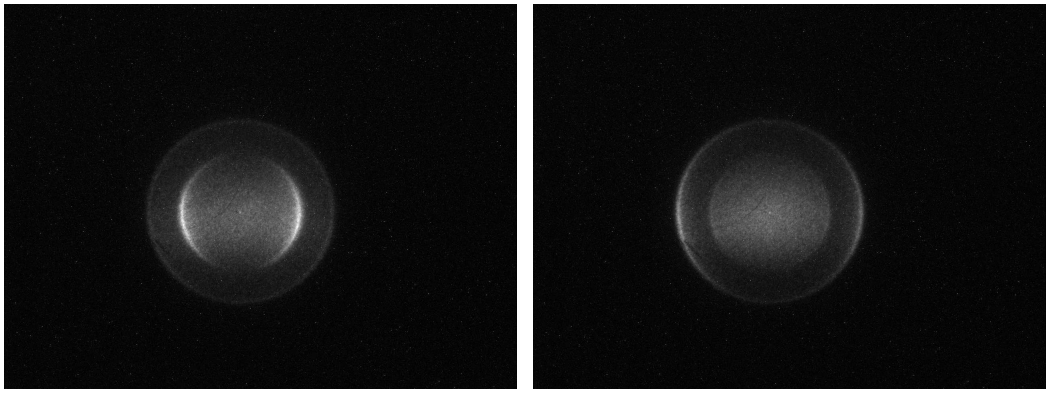

Figure 5.3: Left: the standard velocity-map image. Right: the same image with the half-wave plate installed, rotating the velocity distribution by ninety degrees.

axis, then the major recoil direction of fragments corresponding to the Br + Br* channel will be directed along that axis, i.e. the molecular beam axis, z. Velocity-mapping conditions will merely compress the velocity distribution into a blob. This makes it much more challenging to determine the point of velocity cancellation, since we cannot directly see the critical velocity, v_z. To attempt to bypass this issue, a half-wave plate was inserted into the beam path of the dissociation laser on a flip-mount, as depicted in figure 5.2, with the ion detection axis parallel to the molecular beam direction. This allowed the dissociation photon polarisation to be rotated by ninety degrees to directly image the velocities of the inner ring, albeit without being able to stop the atoms simultaneously (as recoil is perpendicular to the molecular beam). The images in figure 5.3 show this. The left hand image is the standard velocity-map image, and the inner ring edges can clearly be seen. However, in the right-hand image, the central Newton Sphere has essentially been rotated by ninety degrees, and appears as a complete circle. This alteration considerably simplifies the determination of the point of velocity cancellation as we can now see the fragment velocities directly.

A side-effect of bromine usage in the experiment was the increased strain upon the turbopumps; corrosion can be a serious issue for the bearings of the pumps, and can lead to catastrophic failure. Hence the decision was taken to switch the pump on the source chamber to a diffusion pump (Edwards Diffstak 160/700). The effect

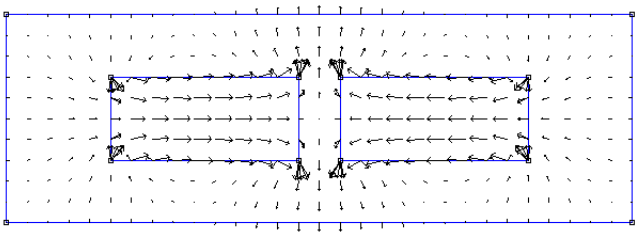

Figure 5.4: The magnetic field lines in the experiment which will be followed by the ions, causing the skew in the images [1].

on the pressure in the main chamber was almost negligible; the running pressure rose slightly to 3x10^{-7} mbar.

5.2 Ion detection

A significant difference between the detection of ions in the original experiment, and detection from within the trap, is the presence of the magnetic field lines (see figure 5.4). Although the trapped atoms only experience a magnetic force based upon the magnitude of the |B| field, the ions will experience the Lorentz Force:

$$\mathbf{F} = q[\mathbf{E} + \mathbf{v} \times \mathbf{B}], \tag{5.1}$$

where q is the charge of the ion, $\mathbf{E}$ is the electric field, $\mathbf{v}$ is the ion velocity and $\mathbf{B}$ is the magnetic field. This will perturb the velocities, and will appear as a skew in the velocity-map image. This can be seen in figure 5.5, where the simulated skew is that which would be expected for a magnetic field of 0.2 T, suggesting that the magnetic field calculations as detailed in section 4.2.1 are indeed correct.

In this regime of magnetic skew, it is important to note that whilst the ions are still being velocity-mapped, the extra force applied only to the ions means that we cannot easily extract the underlying velocity distribution of the atoms. However, the ring structure of the ion images is maintained, albeit in a distorted fashion. This is important as it allows us to optimise the experimental parameters. The zero velocity point remains in the centre of the image. By maintaining the symmetry

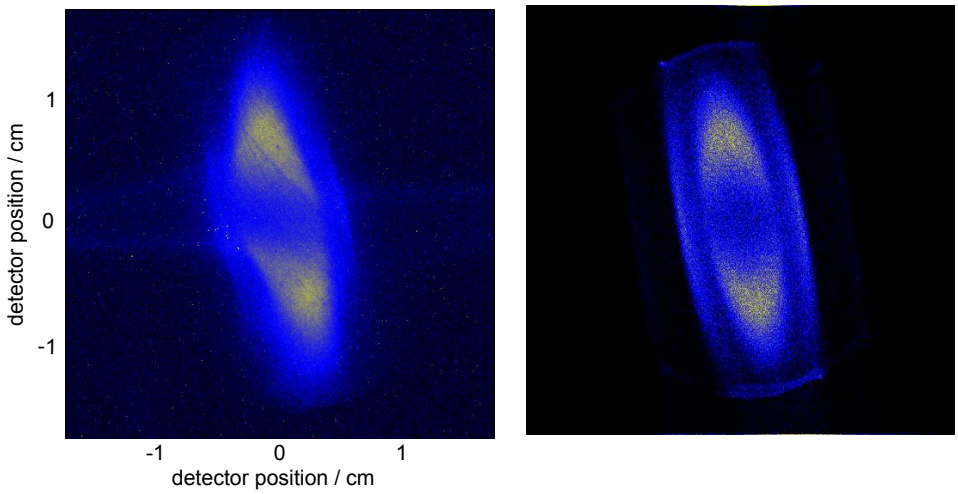

Figure 5.5: The effect of the Lorentz force on the magnets upon the ion velocities. Left: Experimental ion image. Right: simulated ion image using a magnetic field of 0.2 T. The compression the top and bottom of the image are caused by ions approaching too closely to the magnets.

of the skewed image by changing the wavelength of the laser with respect to the incident fundamental beam, the image can be optimised. The particular model of dye laser used in this experiment was not equipped with a temperature-controlled cavity, and hence some manual maintenance of the wavelength was necessary as the temperature of the lab rose.

5.2.1 Time-of-flight detection

The alteration of the experiment to accommodate the magnets meant that the molecular beam axis became co-linear with the detection axis, preventing simultaneous velocity-mapping and velocity cancellation. Since velocity-mapping became unusable, a new method of detection was required, based on time-of-flight analysis. A bootstrap amplifier, constructed by the Electronics Workshop in the Department, was attached to the phosphor screen of the MCP detector, from which the voltage could be measured. This is proportional to the instantaneous ion current, integrated over the whole ion image. This could be directly transmitted to an oscilloscope, yielding a TOF trace.

In the TOF experimental configuration, a shallow voltage gradient can be applied

between the repeller and magnet plates. This achieves the goal of temporal separation of the zero-velocity atoms from fast-moving atoms and the residual molecules in the molecular beam, as opposed to the spatial separation seen in the velocity-map method. Since there will be minimal acceleration provided to the ions, any ions moving with a high v_z will enter the region of greatest electric field gradient (between the magnet plate and the extractor), and will therefore reach the detector much more rapidly than those with near-zero v_z. The voltage settings for the ion optics are considerably different from the velocity-mapping case; the voltages are 2000, 1700 and 600 V for the repeller, magnet and extractor plates respectively. These TOF traces are recorded on a PC, processed in real time by a Labview program to perform the background subtraction. After accumulation, the background subtracted signal can be integrated to give a zero-velocity signal level. The TOF for the bromine atoms is around 9 μs under the current detection scheme, in which the flight tube is 310 mm long.

A typical velocity separation trace can be seen in figure 5.6 shown at a pump-probe delay of 0 s. This shows the separation of the atoms which are accelerated towards the detector (left hand peak) and those which undergo velocity cancellation to some degree (right hand peak). Since there is little acceleration from the electric field gradient in the magnetic region, the faster atoms will reach the detector prior to the slow ones. The red line in figure 5.6 shows the expected TOF distribution from the velocity distribution created in the experiment. We can see that there is a good deal of blurring between the two cases. The majority of this blurring effect can be attributed to the limited speed at which the amplifier (built in the PTCL Electronics Workshop) can read the ion-current signal which is transmitted across the MCPs. Attempts to correct this whilst limiting the 'ringing' effect seen (oscillations in the baseline after a large signal peak) could be further improved. It is also likely that the different amplitudes of the forward and backward peaks is also an experimental artifact, created by the amplifier.

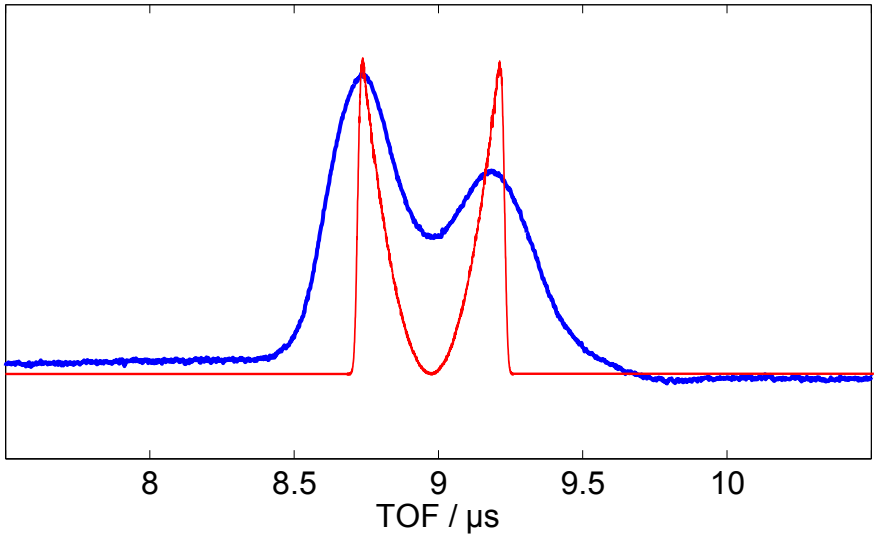

Figure 5.6: A typical TOF trace for dissociation at zero time delay, blue. The red line gives an indication of the TOF distribution expected for the atoms if their flight speed were equivalent to their lab-frame velocity at creation. The lack of resolution is largely due to poor time resolution on the amplifier.

Isotopic separation

The isotopic distribution can be seen for appropriate experimental conditions in the TOF spectra. Since the ^{79}Br and ^{81}Br will be present in almost equal numbers, then their presence will broaden a given peak. Figure 5.7 shows a TOF trace taken for a pump-probe delay of 3 μs. We extract the arrival times by fitting each mass to a Gaussian function. The first of the two peaks, that of ^{79}Br, arrives at 9.19 μs. Using equation 2.23, we predict a TOF for ^{81}Br of 9.30 μs. The centre of the Gaussian fit is 9.29 μs, so we can be sure that the splitting we see is entirely due to the difference between the masses of the two isotopes.

The reason we only see the splitting occasionally is an effect of the isotopic abundance; in the Gaussian fit in figure 5.7, the areas are calculated to be 0.895:1 in favour of the ^{81}Br. The overlap of the two signals in the TOF is such that, at equal peak amplitude, they will coalesce into one broad peak, which will appear as a flat-topped Gaussian. This is one possible explanation. The expected isotopic ratio is 1:1, but it is not necessarily correct to presume that detection probability is isotope independent, so there may be other subtle factors at work.

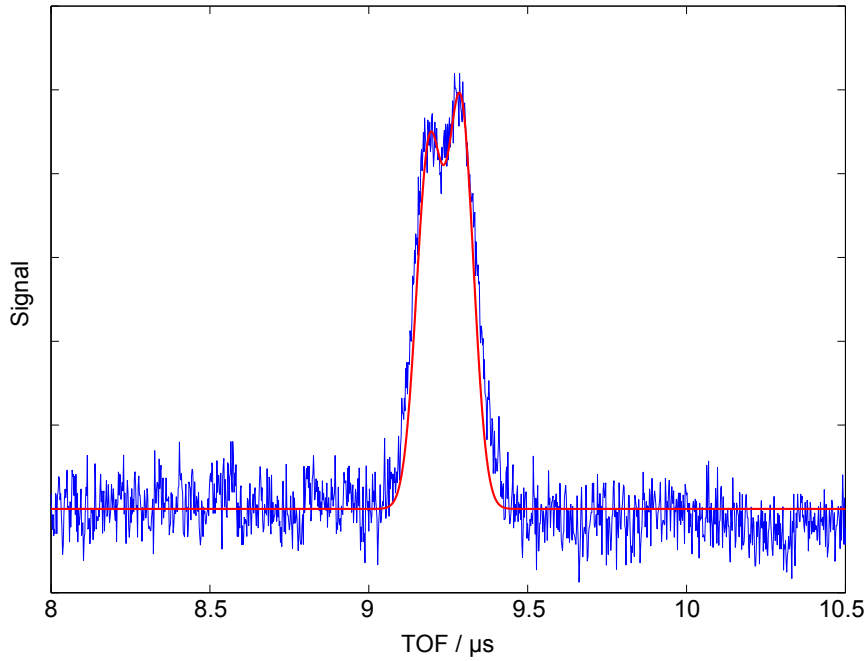

Figure 5.7: A TOF trace, blue, taken at a delay of 3 μs. In this particular example the isotope splitting in the TOF can be seen, a fit has been made using a pair of Gaussians.

5.3 Experimental results for Br atom trapping

The objective of these experiments is to determine whether bromine atoms are being confined within the magnetic minimum of the trap. This is investigated by comparing the decay curves with a magnetic field present, with the aluminium 'magnot' case, as described in section 4.3.1.

To perform the experiments, the apparatus was configured as shown in figure 5.2. The dissociation and probe lasers were aligned co-linearly through the centre of the trap, determined by the position of the apertures of the doghouse irises (see section 4.3). The focal positions were determined whilst the chamber was open; the two spots were overlapped centrally by eye, as closely as possible. The ion optics were then reinstalled, and the alignment through the irises could then be improved. This was achieved by monitoring the laser beam intensity leaving the chamber for each beam, and by how well the lasers overlapped at their respective sources. As an additional check, the CCD camera could be positioned at an angle to the entrance window, so as to safely observe and minimise the scattered light from

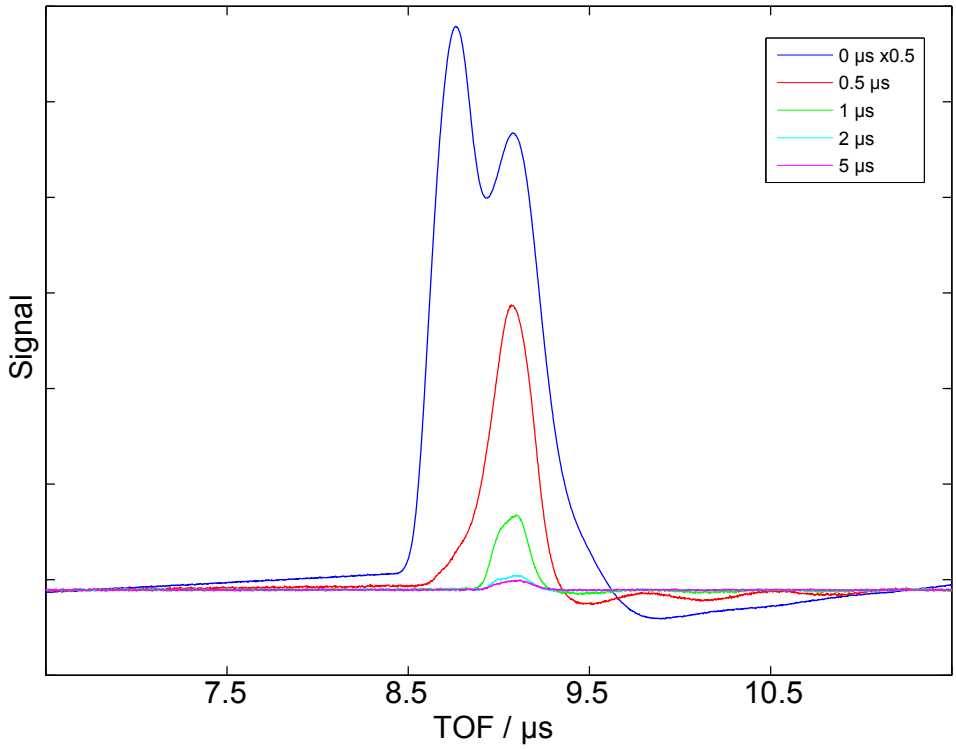

Figure 5.8: TOF traces taken at short pump-probe delay times: 0, 0.5, 1, 2 and 5 μs. The raw signal is shown here, since the background signal is negligible compared to the stopped signal. The zero-time signal has been scaled by 0.5 for comparison.

the iris. Finally, the signal was optimised on the velocity-map image itself.

The results appear in the form of figures 5.8, 5.9 and 5.10. In figure 5.8, we are able to see that the peak at the shortest TOF does in fact correspond to the atoms which are accelerated during the photodissociation process, since they vanish from the TOF trace after 200 ns or so. From these images, we can see the same style of exponential signal decay as seen in the velocity-map imaging experiments. Over the course of the first few microseconds, the majority of the atoms have disappeared. However, a few remain, and they can be seen at the TOF of the right hand peak. For comparison, compare the shapes of the peaks with figure 3.10. This gives us the best indication that our extraction plates are giving us the expected velocity separation.

As we move to longer delay times (as in figure 5.9), we see that the effect of the background gas signal (centered on zero-velocity), becomes more significant relative to the stopped-atom signal (see figure 5.12). As the intensity of this gas signal does

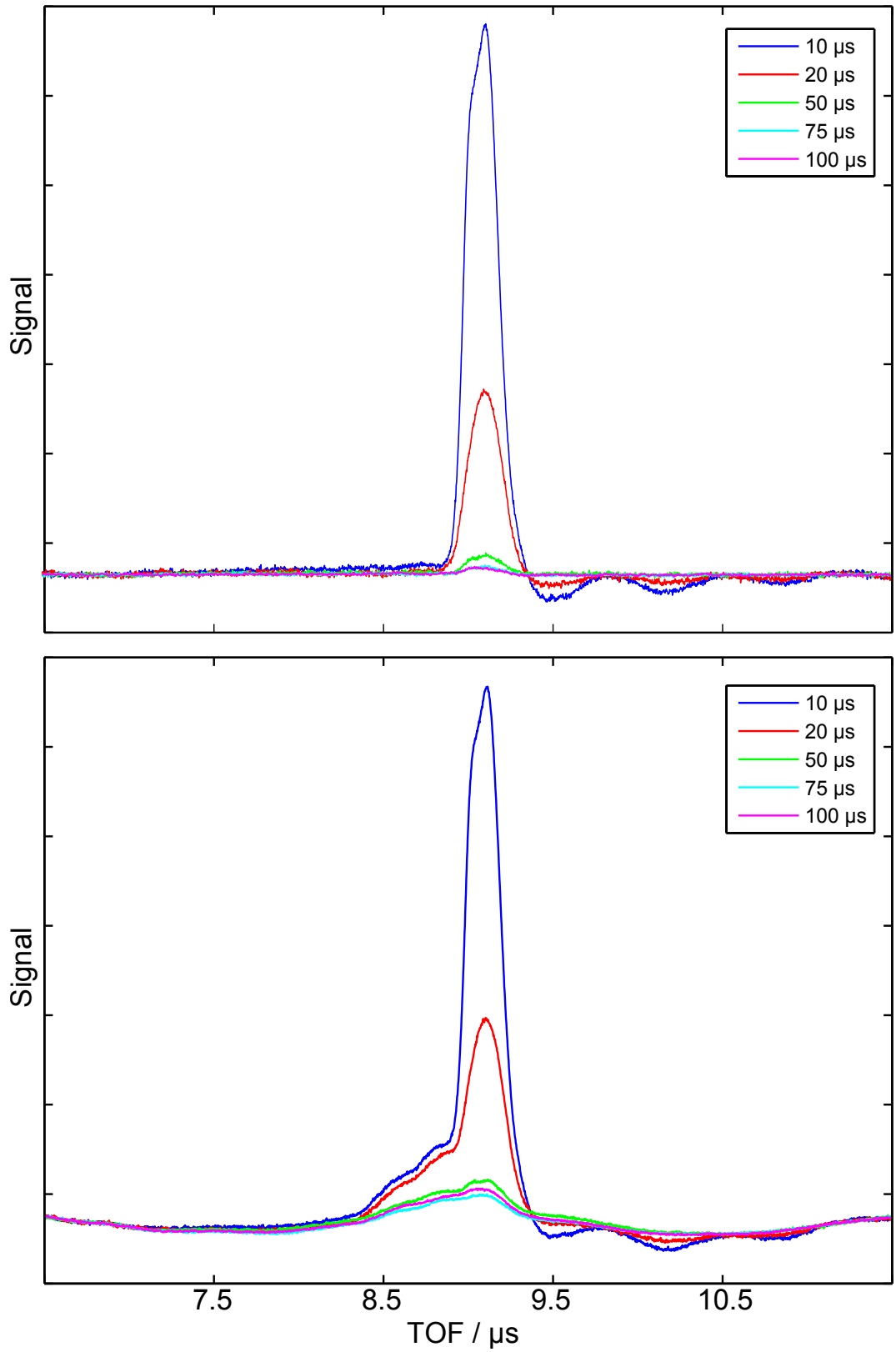

Figure 5.9: TOF traces taken at medium pump-probe delay times: 10, 20, 50, 75 and 100 μs. The top panel shows the background subtracted signal, and the lower panel shows the raw data.

not change with pump-probe delay, whereas the stopped signal drastically reduces, the relative contributions change. As a result, we move to a background-subtraction regime to see the stopped signal more readily. In addition, we see a component from the molecular beam pulse, which decreases with respect to pump-probe delay. This can be seen in the traces at a TOF of around 8.5-9 μs.

At the very longest delay times at which we have managed to see stopped-atom signal (shown in figure 5.10), it is impossible to discern the stopped-atom signal from the background at all, and background subtraction is the only reliable method of proving that there is some residual 2-colour signal. Whilst the raw data is not helpful on its own, the background subtracted signal is quite clearly non-zero, and such a signal can only be attributed to atoms created via velocity vector cancellation. This near tenfold increase in the retention times of the bromine atoms when compared to the previous results [2], prove that the magnets are having the desired effect.

In the long delay images, there is a relatively large signal peak at around 6.5 μs, which is reproducible with and without the molecular beam pulse being present. As such, this is attributed to arising from the 2-colour dissociation of background hydrocarbons.

Analysis

We are seeking to observe a very small signal on top of a relatively large background, so simple background subtraction is unlikely to give a very satisfactory result; the signal will likely be lost in the noise, as can be seen in figure 5.10, lower panel. As such, the best way to analyse the data now is to make a fit to the background data, here calculated as two overlapping Gaussians. This background signal can then be used to fit to the signal trace, with an extra Gaussian added in to represent the signal. The resultant gives us a much more accurate estimate of the actual signal level than trying to fit a Gaussian directly to the background subtracted signal, as seen in figure 5.11. This data processing was performed in Matlab [3], converged using a

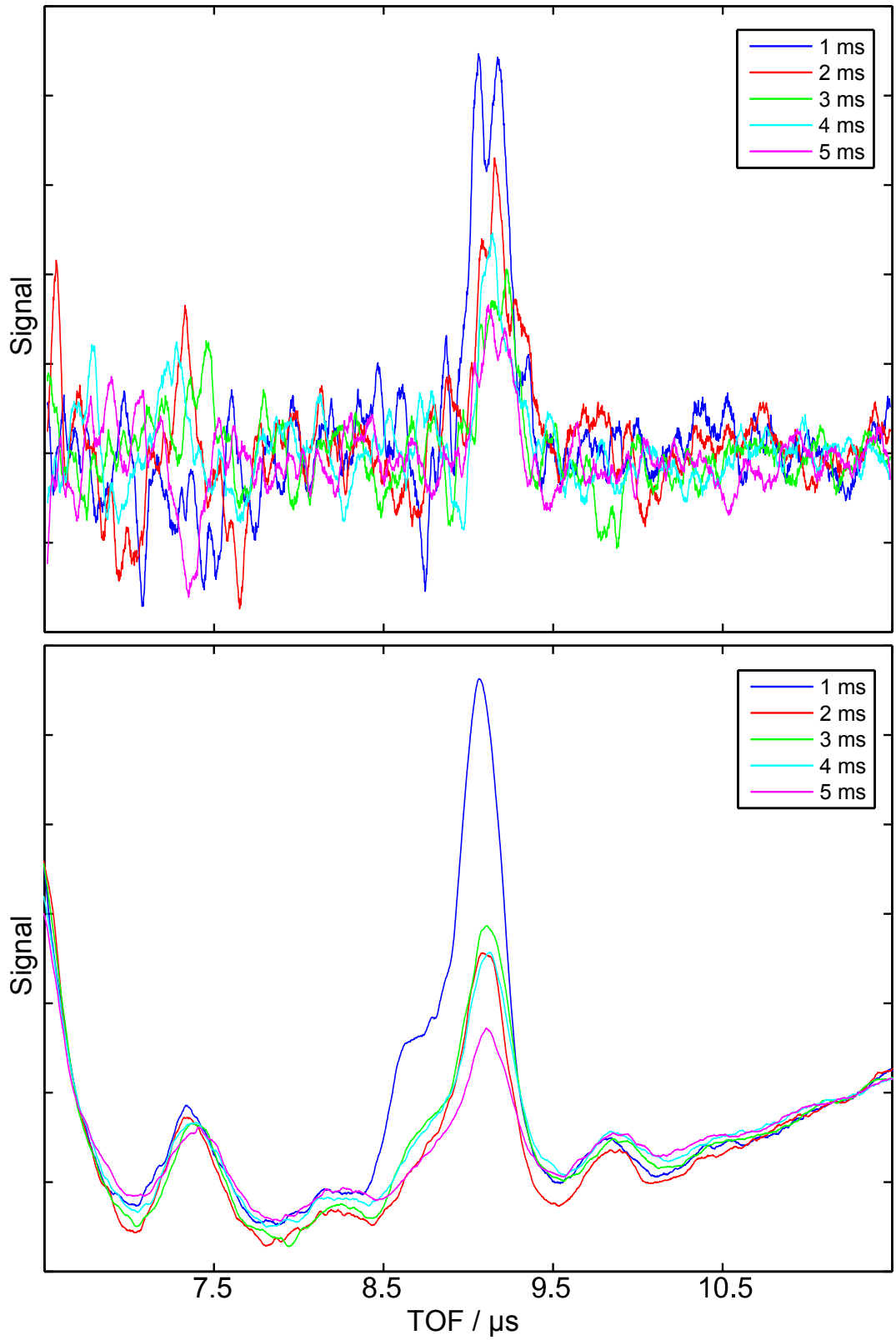

Figure 5.10: TOF traces taken at long pump-probe delay times: 1, 2, 3, 4 and 5 ms. The top panel shows the background subtracted signal, and the lower panel shows the raw data.

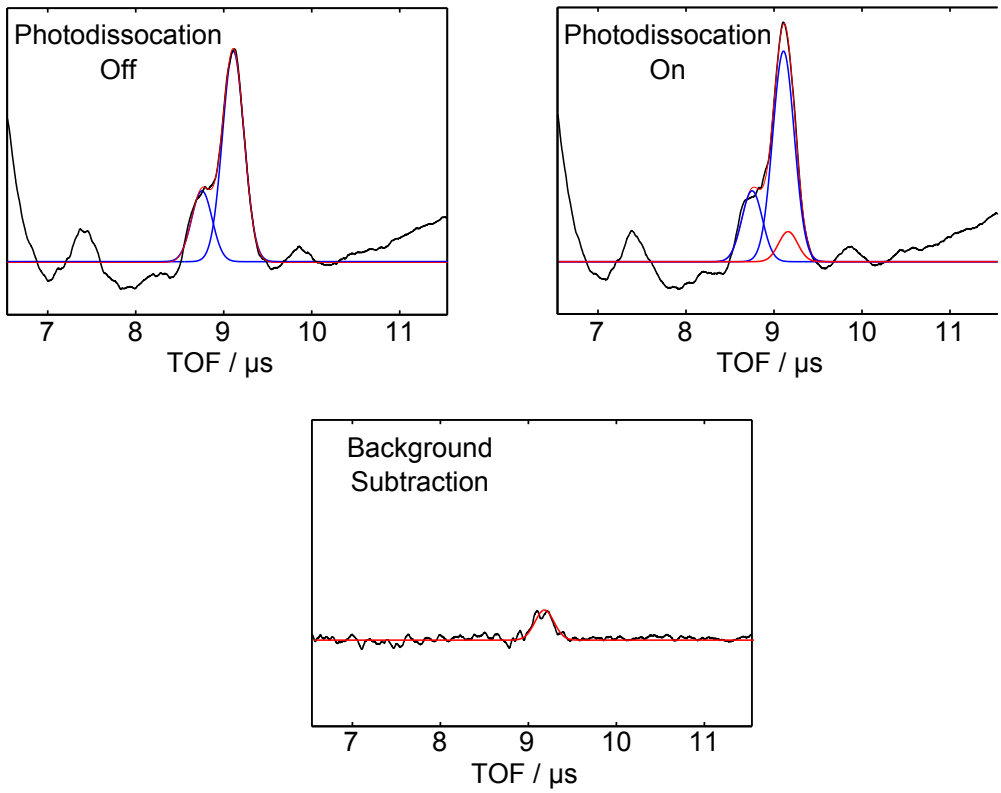

Figure 5.11: An illustration of the fitting of the data, here taken at a delay of 1 ms. The background signal was simulated using two Gaussians, blue (top left), and these Gaussians, plus another to represent stopped signal, red, were used to simulate the dissociation-laser-on signal (top right). The lower graph show the straight background subtracted signal, black, with the simulated Gaussian signal, red, overlaid.

maximum liklihood technique [4] to give the final fitting Gaussians. Confidence intervals on the fit parameters were established using a bootstrap Monte Carlo method [5]. Note, that this treatment was unnecessary for short delay time, and was only performed for the longest (t_{delay} greater than 300 μs) delays.

It may, in future data analysis, be important to consider the nature of the experiment; in performing REMPI, we sum over individual ion arrival peaks, and such data counts are described by Poissonian statistics [6], i.e.

$$P_{\mathrm{Poisson}}(c;\mu) = e^{-\mu}\frac{\mu^c}{c!}, \tag{5.2}$$

where μ is the mean number of counts expected, c is the number of counts, and $\mathrm{P}_{\mathrm{Poisson}}$ is the probability that a measurement will give c counts. Notably, for the

Poisson distribution, the sum of two distributions remains Poissonian (e.g. that of background and signal simultaneously). Subtraction, however, does not yield another Poissonian distribution, hence, we have fitted the background, and the signal cases separately, but not the background minus signal. To fully get a handle on the data, a truly Poissonian analysis ought to be considered. However, for the time being, the standard fitting method is satisfactory.

But what is the background signal? Figure 5.12 shows the different sources from which the signal may come in the experiment. It shows the velocities along the z-axis for the different sources, which should have a linear relationship to the times-of-flight of the respective ions. The relative signal intensities are not to scale, but have been rescaled to show the different components of the overall signal. The simulated signal arising from the 2-colour dissociation is shown in blue on the lower plot. In purple, the signal centered on zero-velocity from the background bromine gas in the chamber is shown. It can be seen that this signal directly overlaps with the stopped atom signal. However, since it is dependent on the background pressure in the chamber, this will be near constant, meaning it can be easily background subtracted. The signal from native Br in the molecular beam is shown in green, and in orange is shown the signal arising from 1-colour dissociation and detection of Br from Br_2 in the molecular beam. This will be spread over a large array of TOFs, due to the high recoil velocity of the fragments.

We fit two Gaussians to model the background, at two different ion flight times, hence, they are presumably due to bromine atoms, moving at two different velocities. One peak is directly overlapped with the trapped signal, which would indicate bromine atoms centered on zero velocity. The logical source of these atoms would be bromine atoms remaining from previous shots in the source chamber. These would thermalise through collisions and lead to a distribution centered on zero velocity. Alternatively, residual Br_2 in the chamber could be dissociated and ionised by the probe, which would also produce a signal centered at zero lab-frame velocity. The

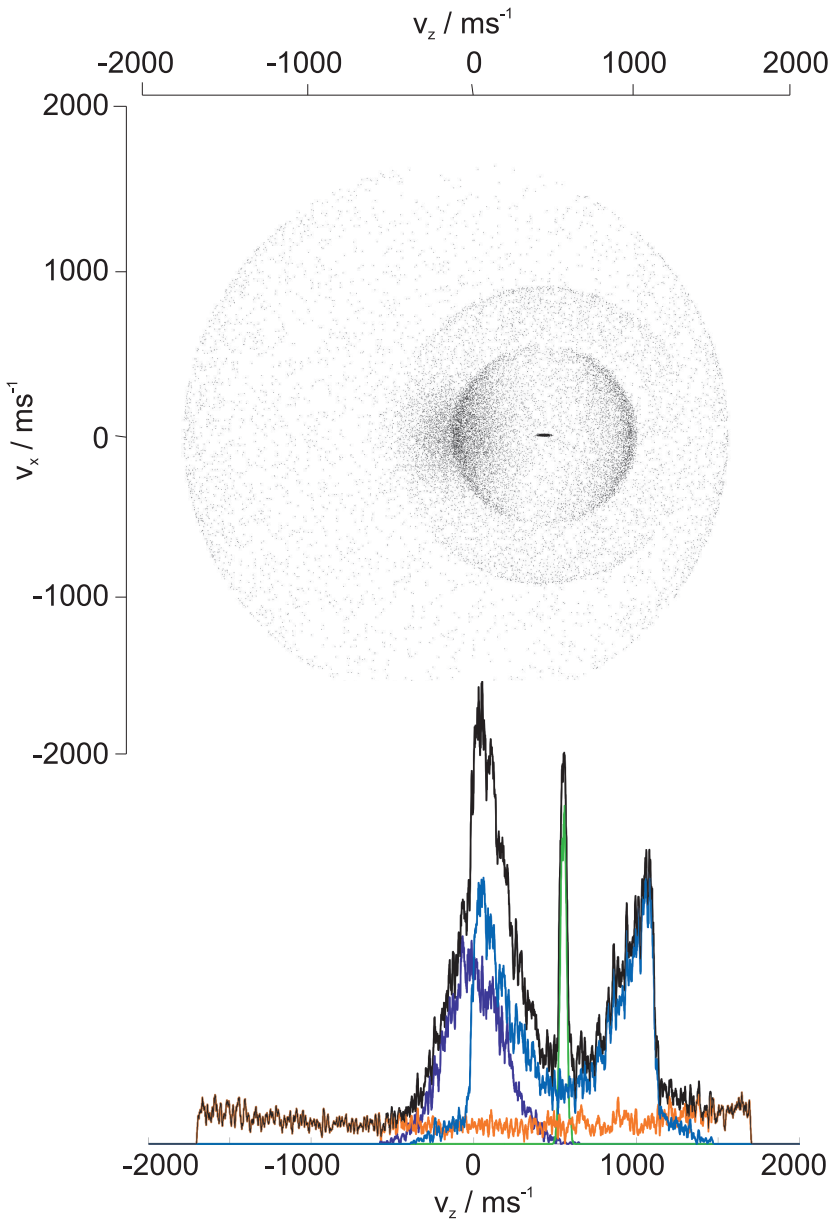

Figure 5.12: Monte Carlo simulation of the various sources of signal, shown as would be seen in a velocity-map, top, and their velocities along the z-axis, v_z, bottom. The black line in the lower plot may give some idea of the TOF signal that we may see. The respective components that make up the black plot are: 1-colour dissociation signal, orange; 2-colour dissociation, blue; background bromine, purple; and molecular beam signal, green.

second peak appears at a shorter TOF, and as a result, must necessarily come from the molecular beam in some form. That could be either the very long tail of the supersonic expansion, or some sort of effusive tail. The latter would appear to make the most sense, given that the delay time here is 1 ms, which would seem to be far too late for a truly supersonic beam to have arrived in the laser focus. The signal itself, presumably appears as Br rather than the expected Br_2 as we are seeing one colour dissociation of the effusive bromine molecules, using the probe laser.

If we indeed take the view that the background peak centered on zero velocity is indeed a result of bromine remaining in the chamber, then we may be able to make some sort of estimate about the density of bromine atoms in the trap. As explained in section 4.3.2, the density of background gas at the pressures used in the experiment is around $10^9 - 10^{10}$ molecules cm^{-3}. If we make the assumption that the gas we put into the source chamber, a mixture of argon and bromine, makes up the background gas for the most part with the same component make-up, then this gives us a background bromine density of $10^8 - 10^9$ molecules cm^{-3}. Comparing the areas under the fitted Gaussians for the 1 ms case (the case pictured in figure 5.11), for instance, shows that the background signal is 7.99 times as large as that for the stopped bromine case, giving us an estimate for the density of the trapped signal as being of the order of $10^7 - 10^8$ atoms cm^{-3}. This takes quite a few liberties; the background gas in the chamber is not going to be purely a mix of bromine and argon, as can be seen in figure 5.10, and it may be the case that the background signal seen is from Br_2 in the source chamber, which, at the Br atom REMPI detection wavelength, will have a considerably smaller detection probability than the fragment atoms. This would artificially inflate the apparent density of the trapped signal by an unknown amount. Still, as a first approximation to the trapped atom density, an upper limit of 10^8 atoms cm^{-3} would appear to correlate well with that previously shown in section 3.3.3, even though this may appear higher than the probable density, as estimated in section 4.2.1.

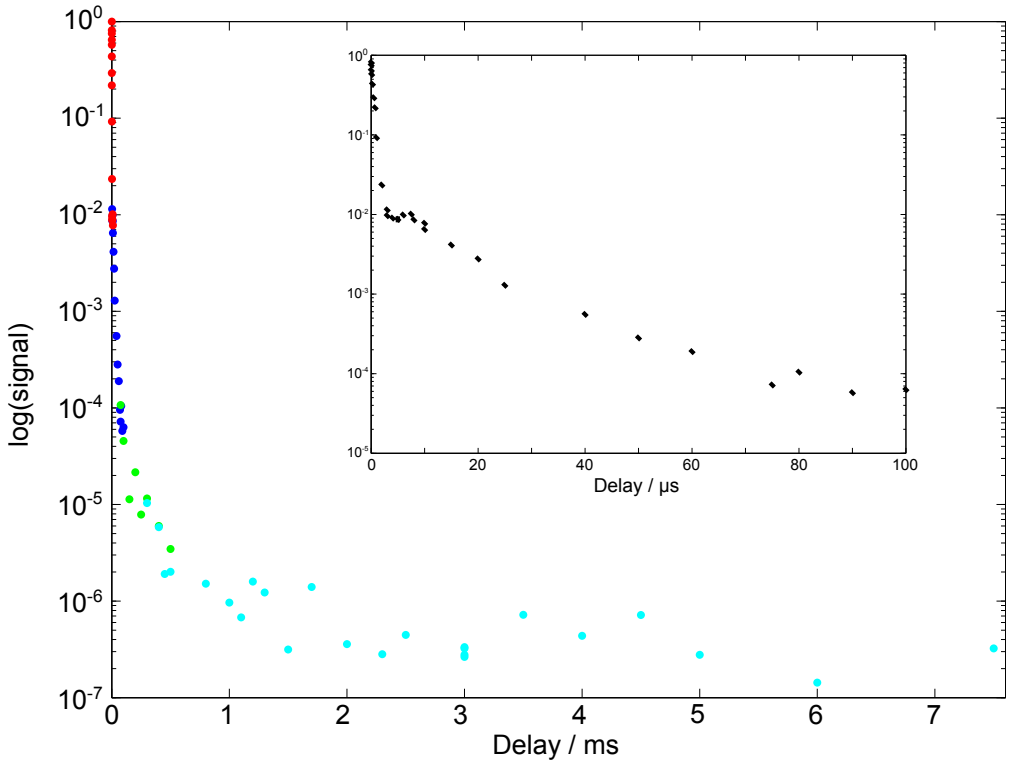

Figure 5.13: A plot of the full decay curve for Br contained in a magnetic trap. It is obvious from the graph that there is a very rapid initial decay, where the fastest atoms fly out of the laser region. After around 100 μs, the drop begins to level off, and it is in this region that the trapping of the atoms becomes evident. The different colours indicate that the points come from a different data set, collected at different MCP voltages. The inset image shows the short-delay decay curve.

5.3.1 Decay profiles

The clear result of the change to the TOF technique is the ease with which we can detect Br atoms at very long pump-probe delays. It is possible to see the signal for delays of up to at least 5 ms when background subtracting the two traces, a fiftyfold increase over the velocity-map imaging set up. When we plot out the integrated signal over the time-of-flight, we see the full decay curve and get some idea of the fraction of atoms that have been lost over the course of the experiment.

Figure 5.13 shows the full decay curve. Each different colour in the diagram represents a different data set, which have all been normalised to one another. The ranegs of delay times measured for each curve overlap, and from these overlap regions a relative signal level can be calculated, which is normalised to zero time. In

order to fully see the signal at longer delay, the voltage applied to the MCPs had to be raised (see section 2.4.2), hence the separation of the data sets. The data taken for the longest delay times were taken at a higher gas pressure in the source chamber – this measurement gives us some indication of the gas flow levels – in addition to being at a higher MCP voltage, for increased detection efficiency. The gas pressure had to be lowered to take the shorter delay data, since there was a very large signal generated from 1-colour dissociation of the molecular beam pulse. The implication of this may be that the first three data sets (blue, red and green) are not fully comparable with the long delay data (cyan), since the atoms will be experiencing many fewer collisions with the carrier gas than the signals recorded at the longer delays. However, since we know that over the early part of the decay curve, the overwhelming major component of signal decay is attributable to the ballistic expansion of the high-speed fragments, then for the purposes of constructing a decay curve with a meaningful y-axis scale (i.e. fraction of the zero time signal remaining), the curves have all been combined. This therefore assumes that the collisional loss for the first three data sets is negligible.

It can be seen that the majority of the loss of signal occurs over the first 100 μs, which can be attributed to the ballistic expansion of the type seen in section 3.3. The implication here is that if the ballistic expansion continued in a similar manner, we would be pushed to the very limit of our detection capability by around 100 μs. This matches well with the previous results. After this point, there is a lesser rate of decay, up until around 1 ms, and after 1 ms, the signal level stabilises somewhat, and the gradient becomes almost horizontal. Under this scheme, we have managed to detect zero velocity atoms out to 5 ms. Beyond 5 ms, the signal level begins to become statistically insignificant when compared to the noise level in the experiment, representing the limit of our detection efficiency currently.

What do these data tell us? In section 4.2.1, it was predicted that the fraction of atoms with kinetic energy less than the trap potential was 2.5×10^{-6}. The

decay curve here appears to bottom out somewhere between 1×10^{-6} and 5×10^{-7}, when compared to the signal at zero time. This is less than an order of magnitude difference, so it would seem that the simulated decay curve is quite reasonable.

It is important to consider what factors may have an effect on the fraction of atoms remaining. Although the simulated and experimental fractions match well, we would still do well to consider all possible sources of loss in the trap. For one thing, the simulated fraction was established purely from a kinetic energy standpoint. Although the dissociation laser is tightly focussed, it does have an estimated radius of around 200 μm, and the focal region extends along the length of the trap on its own axis, x. This means that the atoms formed at the edge of the laser focus could be created at a location with a potential energy of 20% of the value of the trap depth. These atoms will have a much lower critical velocity for trapping, that is, the velocity below which permament trapping would occur, in the absence of any loss processes. Along the x-axis, the atoms could be formed with almost any potential energy, up to the trap depth. As a result the absolute number of atoms seen will not be equivalent to the number calculated from simulations. The critical velocity with respect to the potential energy at formation is shown in figure 5.14.

Something worth noting at this stage is that the trapped atom velocity distribution is wholly controlled by the potential. We may attribute a 'temperature' to the sample, based on the depth of the trap, but the velocity distribution is not Boltzmann-like, and the temperature has no meaning from a traditional thermal perspective, other than as a reference for the so-called critical velocity of the trap. In addition to the effect of the magnetic potential at formation, the lower than expected baseline could also be attributed to the many avenues of trap loss. These have been discussed in section 4.3.2: collisions with the molecular beam; collisions with the background gas; and Majorana losses. Such factors are likely to be lowering the detection probability at delay times greater than 1 ms.

A final possibility is that whilst we are creating these near zero-velocity atoms

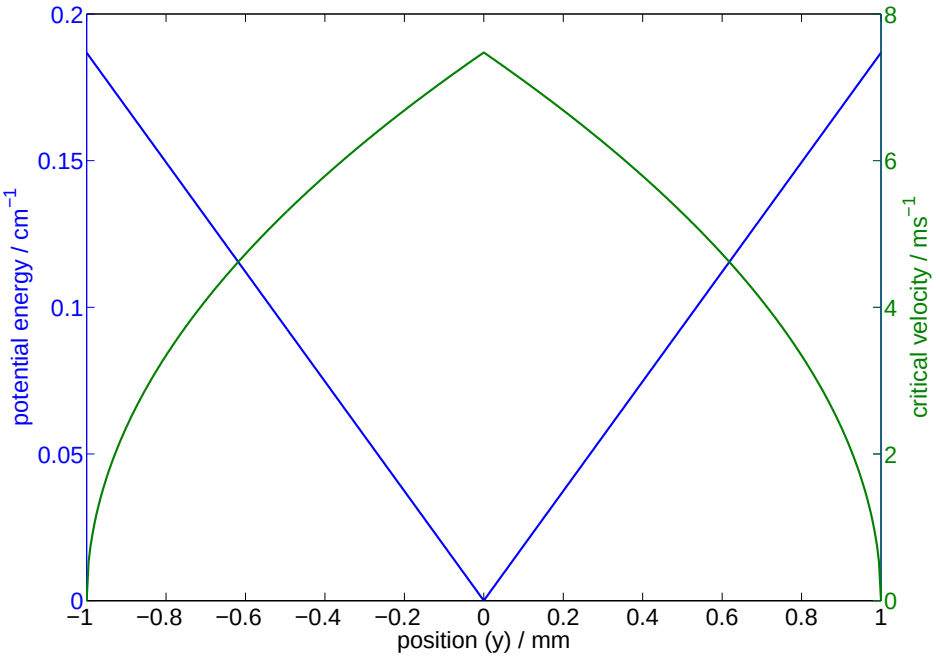

Figure 5.14: A plot of the potential energy along the y-axis, blue, and the associated critical velocity, green. The highest velocity acceptance of the trap corresponds with the trap minimum in the centre.

which will be trapped by the magnetic field, we are not necessarily detecting them with the same efficiency as at zero time. The probe laser only interrogates a small volume of the trap, and it is plausible that as the cloud of atoms diffuses out to fill the trap, the overall density of cold atoms decreases, leading to a reduced detection probability in the ionisation volume. Some atoms may be trapped in orbiting trajectories that never pass through the ionisation region.

'Magnots'

To be sure that we indeed have succeeded in trapping atoms, the same experiment was carried out with the 'magnots' as described in section 4.3.1; the aluminium blocks of identical volume to the magnets. This requires a dismantling of the experiment, so utmost care needs to be taken to try and avoid perturbing any of the optics or the irises attached to the magnet extractor plate. Successful change-over would require no realignment of the lasers, thus ensuring an identical focal overlap

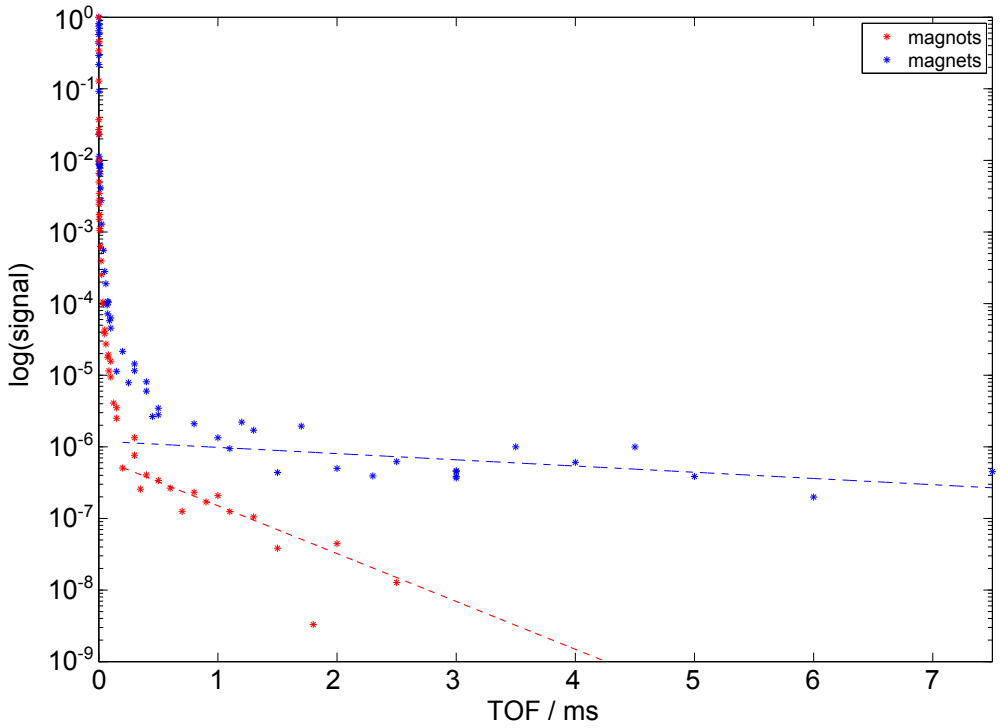

Figure 5.15: Comparison of the decay curves recorded for a confining magnetic field (blue) and the magnetic field free case (red). The curves have been self-normalised to their respective zero-delay signal levels. The coloured dashed lines are guides for the eye at long delay time for their respective cases.

for direct comparison of the two cases.

The comparison between the decay curves for the magnets and magnots can be seen in figure 5.15; the insertion of the magnetic field has had a profound effect upon the decay of signal with respect to time. There is significant enhancement of the signal with the magnetic field present compared to the field-free case. In the figure, there is noticeable deviation between the two curves after around 50 μs, similar to that predicted in section 4.4. More critically, the difference is not only in the relative fraction remaining at a given delay time for each case, but also in the slopes of the decay curves at long delay. As seen in figure 5.13, the gradient of the decay curve at long delay is close to horizontal, suggesting that any signal that remains is due to spatially confined bromine atoms. For the 'magnot' case, the rate of signal loss beyond around 200 μs is constant, and appears steeper than the gradient in the magnetic case. This clearly shows that the zero-velocity atoms created in the magnetic-field-free case are not restricted (other than possibly physical restriction by

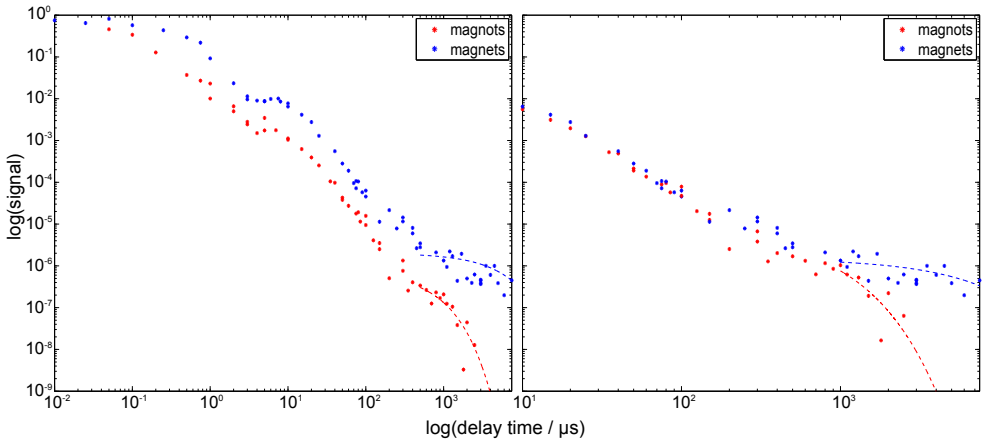

Figure 5.16: Graphs of the magnet versus the 'magnot' decay, plotted on a double log scale. The self-normalised curves are shown in the left hand plot, whereas the right hand plot at long delay has been normalised at a delay of 10 μs. This eliminates much of the offset between the curves.

the magnots, which would ought to be identical to the magnet case), and dissipate out of the ionisation volume.

There is something of a disparity between the two decay curves, in that at very short delays, the decay curves do not match one another as would be expected. Although both curves are self-normalised – that is normalised to their own respective zero delay signals – there is a considerable difference between the decays in the first few microseconds. This is best illustrated with the use of a double log plot (figure 5.16). The figure illustrates that if we were to normalise the respective decay curves to one another, for instance at 10 μs, then much of the difference between the two curves vanishes, and it is only at the very longest delays, i.e. greater than 1 ms, that any difference can be seen. This begs the question of whether there is some slight difference in the laser overlaps, however minute, in the two cases, as differences in the early decay curve will be due to the fastest atoms vacating the probe laser volume.

A side effect of plotting the data on double logarithmic axes is that the various phases of the loss from the trap volume are much more visible. It can be seen for the left hand plot in figure 5.16, that there is a plateau in the decay curve somewhere between 1 and 10 μs. It is unclear what exactly is causing the plateau; it appears

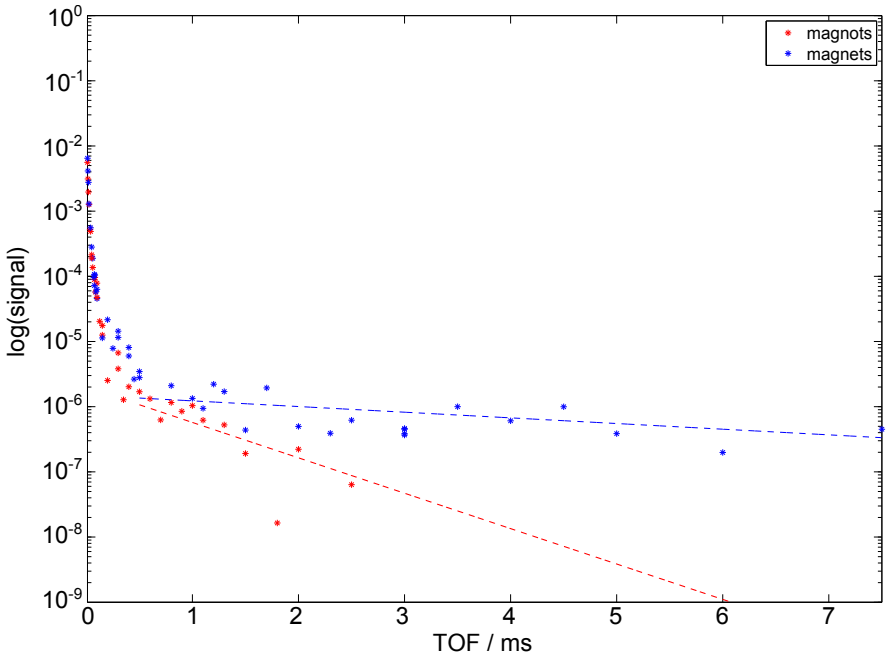

Figure 5.17: Plot of the renormalised decay curve for the 'magnot' case from 10 μs upwards. The gradients of the decay at long delay are unchanged from the previous graph, but the early part of the decay curves match much more closely.

in both curves, but is more pronounced in the magnet case. This can be seen most clearly in the inset to figure 5.13 It could well be an experimental artifact. Nevertheless, the overall shape of the logarithmic decays is expected; at early delay times, there is little discrepancy, whereas at longer delays, the magnetic trap retains bromine atom signal much more significantly.

Figure 5.17 shows the renormalised decay curve for the 'magnot' case with the standard x-axis. It is clear from this that the separation of the two cases from one another in the decay curves may not manifest until we reach the very longest delay times: 1 ms and upwards. There is clearly a difference between the two cases; we cease to be able to detect signal from the 'magnot' case at all, beyond around 2 ms, whereas we only really reach the detection limit for the magnet case past 5 ms. There is no data past 7.5 ms since the random background noise becomes comparable to the signal peak itself, and to average this out, then the experiment would need to be run for longer than it takes the probe laser to drift off resonance.

5.3.2 Molecular beam collisions

An important measurement required to determine the effect of the collisions of the carrier gas in the molecular beam upon the trapped sample, is to take a series of delayed signal measurements photodissociating at various points through the molecular beam pulse width. This can be achieved by changing the triggering time between the firing of the dissociation laser and the molecular beam pulse. Since the intensity of the molecular beam pulse is different at each timing, a normalisation scan is taken at zero pump-probe delay to gauge the signal level from that molecular beam density. Figure 5.18 shows the change of the zero-velocity signal at 1 ms as a function of the gas pulse–photdissociation laser delay; i.e. the delay between sending the voltage pulse to trigger the General Valve, and the firing of the dissociation laser. The upper plot shows, in blue, the intensities of the signal, as calculated by the fitting the background and signal as in the previous section, with the Gaussians fits shown in red in the lower plot. Overlain on the lower plot is the molecular beam intensity distribution (black squares with blue spline fit).

We can see that, as we dissociate later in the molecular beam pulse, that the signal created with zero velocity increases, when normalised to the molecular beam intensity from which it was formed. This suggests that collisions between the trapped atoms and the molecular beam carrier gas are indeed having a significant effect upon the longevity of the trapped sample. This in turn suggests that the temporal duration of the molecular beam pulse is far from optimal. Under such circumstances, it would appear that timing the photodissociation to be later in the molecular beam pulse (in the previous experiments, the gas-laser delay time was 1100 μs, near the peak of the beam intensity) would be preferable.

The collisional removal of trapped density can be quantified, albeit only roughly, given the limited information we possess on the densities involved. If we assume

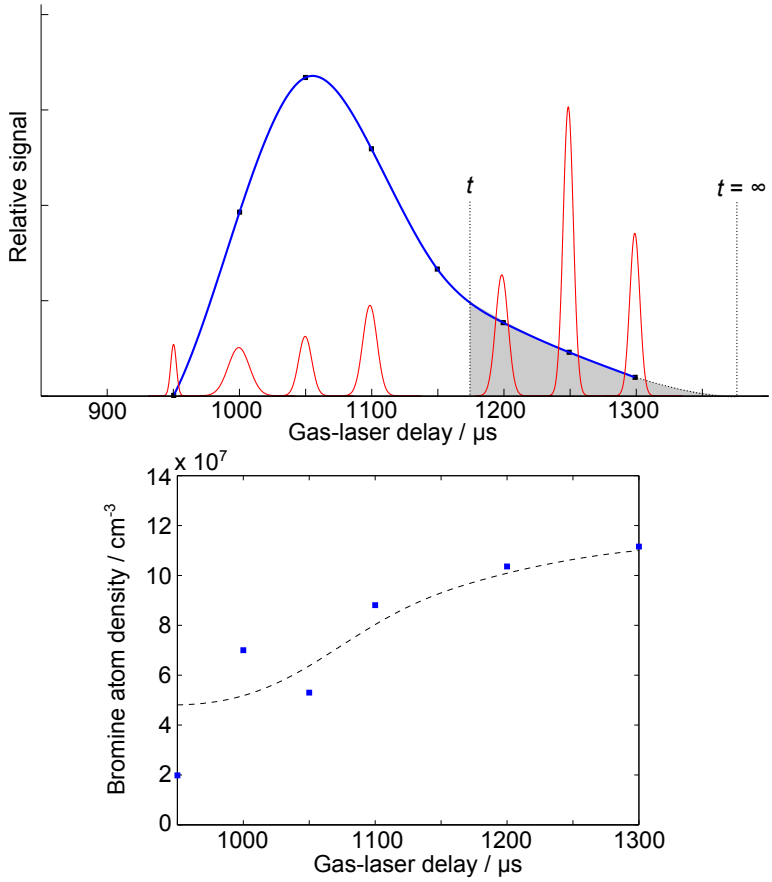

Figure 5.18: Top: a plot of the Gaussian fits to signal taken at 1 ms at different gas-laser delays, red. The overlain curve is the shape of the molecular beam pulse, used for normalisation of the Gaussians. The grey shaded area represents the time bases used in the integral calculation of equation 5.6. Bottom: the integrated Gaussian areas from the top plot are plotted in terms of predicted bromine density, blue. The fit to the signal decay due to collisions with the molecular beam is shown as a black dotted line.

pseudo-first-order kinetics, then:

$$-\frac{d[\mathrm{Br}]}{dt} = k'[\mathrm{Br}], \tag{5.3}$$

where [Br] is the bromine atom concentration, and k', the pseudo first order effective rate constant given by,

$$k' = k[\mathrm{Ar}], \tag{5.4}$$

where [Ar] is the concentration of the argon gas, and k is the bimolecular rate constant. It is expected that k$'$ will have a magnitude comparable with the gas kinetic collision frequency for the density [7]. To account for the molecular beam pulse shape, equation 5.3 can be rewritten as:

$$-\frac{d[\mathrm{Br}]}{dt} = k[\mathrm{Ar}](t)[\mathrm{Br}], \tag{5.5}$$

which can be integrated to give:

$$[\mathrm{Br}](t) = \exp\left(\int_t^\infty k\,[\mathrm{Ar}](t)\,dt\right)[\mathrm{Br}](t=\infty). \tag{5.6}$$

To calculate the rate, we numerically integrate the argon intensity from the molecular beam pulse shape, and assume that the peak intensity is that previously assumed in chapter 3 of 10^{19} atoms m^{-3} for argon. The rate of trap loss from molecular beam collisions is then best fit to the experimental data, as shown by the black dotted curve in the upper plot of figure 5.18. We use our best previous estimate for the trapped bromine atom density of 10^8 cm^{-3} to obtain the expected densities at each point through the molecular beam.

The dotted black curve calculated for the collisional loss in figure 5.18, gives k to be around $5{\times}10^{-16}$ s^{-1} (atoms m^{-3})$^{-1}$, and therefore a k' rate constant of around 5000 s^{-1}. Calculations using the differential cross-section of the bromine-argon potential surface [8, 9], give a rate constant of the same order of magnitude,

when using the same gas density. This good agreement is very satisfactory, given that the experiment is not designed to measure rate constants.

Assuming the bromine atom density of 10^8 cm^{-3}, and taking the trap volume to be of the order of 10 mm^3, this implies that we have approximately 10^6 bromine atoms in the trap. The suggested volume is a reasonable approximation to the actual trapping volume. The volume between the magnets is 16 mm^3, but only about half of this is contained within the 0.2 T magnetic field isosurface. The measurements imply that over the course of the molecular beam pulse, the trapped density drops by about a half; this implies a density of 5×10^7 cm^{-3}. This suggests that 5×10^5 atoms per pulse are being knocked out purely by molecular beam collisions. Future experiments may wish to flesh out these findings, by taking extensive decay curves at multiple points throughout the molecular beam pulse. It therefore follows that the remainder of the loss is due to collisions with the background gas, or Majorana transitions.

5.4 Trapping prospects

What can we conclude from the experiments involving the magnetic trap? Clearly, the introduction of the magnetic field has had a significant effect upon the length of time for which we can detect atomic fragments, indicating that we can indeed confine bromine atoms spatially, and each bromine atom has a kinetic energy less than the trap depth, 3.7×10^{-24} J. This corresponds to a maximum velocity in the trap of 7.5 ms^{-1}, which, using the previous definition for temperature ($\frac{1}{2}mv^2 \leq k_BT$), gives us a maximum temperature of 270 mK. Since we are not operating under the velocity-mapping conditions in this experimental set-up, we do not have a visual way of measuring the temperature of the sample. The signal peak in the TOF spectrum has necessarily been spread out to try and separate the signal from the background as much as possible, thus making the width of the Gaussian fitted peak not the best gauge of temperature.

The main issue it would appear that we have is the collisional removal of bromine atoms from the trapping volume, and thus cannot detect any signal with any consistency beyond 7.5 ms. Further experimental incarnations will have to circumvent this defect, and more precise calculations of the bromine-argon interaction may need to be considered to fully explore the likely trap dynamics.

Bibliography

[1] D. C. Meeker, *Finite Element Method Magnetics*, URL `http://www.femm.info`.

[2] W. G. Doherty, M. T. Bell, T. P. Softley, A. Rowland, E. Wrede, and D. Carty, Phys. Chem. Chem. Phys. **13**, 8441 (2011).

[3] C. J. Rennick, private communication.

[4] I. J. Myung, J. Math. Psych. **47**, 90 (2003).

[5] W. H. Press, S. A. Teukolsky, W. T. Vetterling, and B. P. Flannery, *Numerical Recipes in FORTRAN - The Art of Scientific Computing* (CUP, 1992), 2nd ed.

[6] M. D. Hannam and W. J. Thompson, Nucl. Instr. Meth. in Phys. Research A **431**, 239 (1999).

[7] P. W. Atkins, *Physical Chemistry* (OUP, 2010), ninth ed.

[8] A. A. Buchachenko, T. A. Grinev, T. G. Wright, and L. A. Viehland, J. Chem. Phys. **128**, 064317 (2008).

[9] P. Casavecchia, G. He, R. K. Sparks, and Y. T. Lee, J. Chem. Phys. **75**, 710 (1981).

Chapter 6

Conclusions

This thesis has demonstrated the applicability of the Photostop technique to an atomic system of chemical interest, Br atoms. This has been performed consistently and repeatedly to prove that the method is better suited to use in the atomic case, via dissociation from a diatomic species, than in the molecular fragment case. It has proven that the experiment is capable of creating an atomic sample which could be utilised in chemical reaction studies, should the bromine be spatially confined. In the light of the results of the experiments with the magnets inserted into the apparatus, it would appear that trapping has been a qualified success, and that it should indeed be possible to trap, and accumulate bromine atoms. The main stumbling block to progress appears to be the loss of atoms in the trapping volume over the course of the experiment, indicating that collisions are a significant problem in the experiment as it stands, either with the background gas, or more likely, collisions with the incoming molecular beam pulse. The fitting of the experimental data to determine the loss rate appears to match up with previously calculated values.

6.1 Further work

6.1.1 The extension of the Photostop method

In the introduction to this thesis, it was stated that one of the goals of the project was to try to extend the range of atoms and molecules available to the chemist probing the coldest species, hence the need for novel techniques for the generation of cold species. One of the great attractions of velocity cancellation is that it is a relatively simple process, requiring only two lasers to operate. The simplicity of the ion optics also opens up the possibility for adaptation, as in the installation of the magnetic trap. One could also conceive the possibility of trying this technique on a wide variety of precursors, now that it has proven to be a viable method for generating cold atoms. As has been previously mentioned, the technique has been demonstrated for producing cold NO (and also O) from NO_2 [1], and has been proposed for SO_2 [2] and NO [3] as precursors. Cold chlorine atoms could be generated in a similar manner to bromine, using BrCl [4] or Cl_2 as a precursor [5], since both have highly anisotropic dissociation mechanisms. The approximate beam speed of Cl_2 seeded in Ar would be 560 ms^{-1} requiring a dissociation wavelength of around 460 nm, well within the absorption band of the Cl_2 molecule [6]. Fluorine could only be produced from ClF, since F_2 does not absorb in the correct wavelength region for viable velocity cancellation. D_0 for ClF however is only 21110 cm^{-1} [7], and near-threshold dissociation has been previously observed [8].

6.1.2 Mechanical chopper

As we saw in chapter 5, a major limitation of the experiment is the decrease of the signal over time due to collisions with the molecular beam. This places severe limits on the density of bromine atoms that can be trapped; the trap density will quickly reach a steady state where as many atoms are knocked out of the trap as are loaded in one pulse. It is plausible that with the likely molecular beam densities in the

experiment, that this may even be approached after just one pulse (see section 5.3.2). The clearest solution would be only to allow a very small percentage of the molecular beam to pass into the magnet region. The simplest way in which this could be implemented would be to utilise some sort of mechanical chopper [9, 10], a high speed rotor with a small aperture in it, only allowing bromine molecules with a very specific velocity through, as well as producing a much shorter gas pulse. This would not only reduce collisions with the carrier gas, but also reduce the background pressure in the main chamber. In one swoop, the problem of collisions with the molecular beam as a source of loss for the trap could be removed. A side effect of this ought to be that the clarity of the velocity-map images at long delay times will increase, since there will be fewer background molecules in the main chamber to interfere.

In the time taken to construct a chopper of this sort, it would be of great benefit to upgrade to a UHV system with a base pressure of the order of 10^{-10} mbar. This would almost certainly be a major improvement, greatly enhancing the prospects of observing trapped atoms for long durations.

6.1.3 New trap design

Another possible alteration to the experiment may be that the trap could be exchanged for a new design. As mentioned in chapter 4, other designs of trap, such as a ring based trap, as implemented by Ye and co-workers [11], could be used to increase the trap depth perpendicular to the molecular beam axis, and more easily accumulate bromine atom density. The downfall of a deeper trap would be that the overall ensemble temperature would be greater than that in a shallower trap. However, it may be that the overall density may be greatly increased (higher energy atoms are retained in higher numbers), which may well be preferable for cold reactions.

6.1.4 Prealignment of the molecules

It may be possible to increase the number of fragments that are able to be stopped by prealigning the parent molecules, making them more susceptible to on-axis dissociation [12, 13]. The alignment could be achieved by using the the fundamental beam of one of the Nd:YAG lasers (1064 nm) already in use in the experiment. Such prealignment would increase the fraction available to be trapped for the bromine case, and has been experimentally observed [14]. However, the real benefit of prealignment may lie in being able to stop species with unfavourable β parameters, and thus to extend the number of species available to us experimentally. Since the alignment is dependent upon the polarisability of the precursor molecule, this would clearly work best with highly polarisable molecules.

6.1.5 Magnetic guide

It is plausible that a magnetic guide could be constructed to allow stopped bromine atoms to be transferred from the laser region into a trap, or to collide with another species for reaction, thus eliminating the necessity for very short molecular beam pulses. One could use a guide constructed of permanent magnets either with a bend in it or angled so that the bromine atoms are guided the molecular beam axis. Such guides as envisioned by Halbach [15] have long been used in particle accelerators, but the principles have also been applied to the guiding of metastable neon atoms [16]. Another option may be to use electromagnets which can be switched on and off, which have already been applied to the field of ultracold chemistry, having been used to extract the output of a MOT [17]. However the fields are weaker than those attainable using permanent magnets, unless superconducting coils are used.

Such a guide would be a step towards turning Photostop into a technique for creating a tuneable velocity source of atoms. Whilst the velocity cancellation as currently demonstrated would be directly applicable for use as a target in a cold collision experiment, the prospect of guiding the atoms means that we could alter the

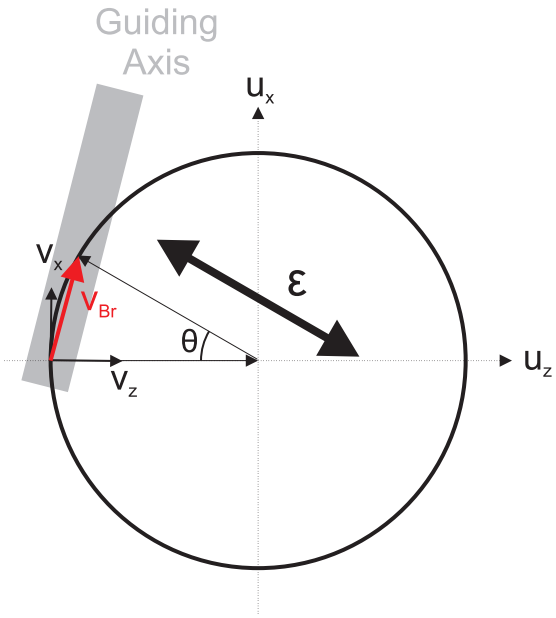

Figure 6.1: Newton diagram showing a possible velocity cancellation to provide a directional velocity boost to the departing fragments.

dissociation wavelength to change the mean velocity of the atom cloud. In addition, one could envisage an experiment whereby the molecular precursor was dissociated either just in front of, or just inside, the guide, and the momentum along the guiding axis would carry the fragments in that direction, with lateral confinement provided by the guide. The momentum kick could be achieved by rotating the polarisation of the dissociation laser by a certain angle so as to give a kick to the fragments along that axis, after which they could be guided away. This is illustrated in figure 6.1. If the electric vector positioned at some angle, θ, to the molecular beam axis, a parallel dissociation would fragment primarily along an axis rotated θ degrees to the molecular beam axis. As in figure 6.1, most of the forward velocity would be cancelled out, but the atoms would gain some transverse momentum, and overall, the mean velocity would be small, and directed along v_{Br}, as shown. A guide could be placed along this axis, in order to move the atoms towards another cold species for study.

Alternatively, the polarisation could be kept constant, with the guide positioned at a very acute angle to the molecular beam axis, and the dissociation wavelength

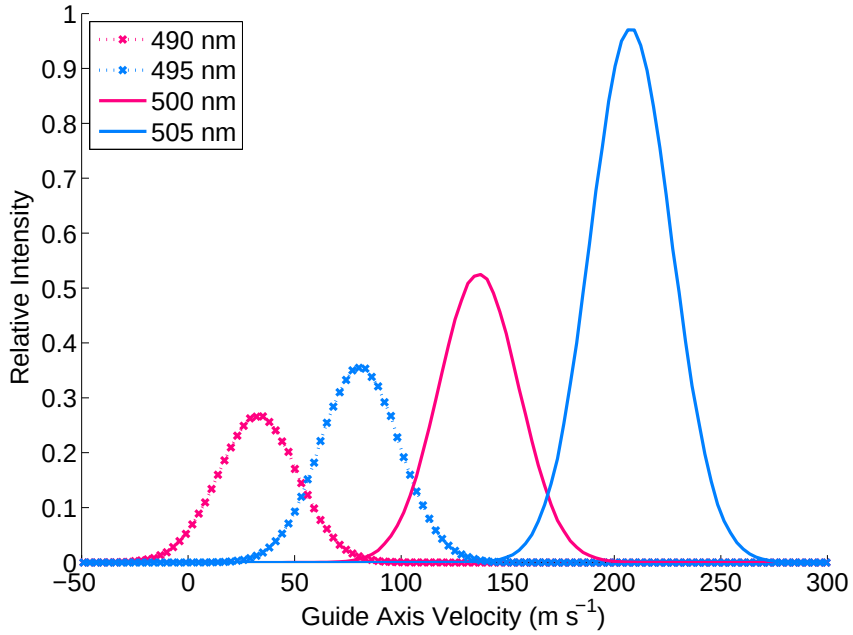

Figure 6.2: Simulation of the output of a magnetic guide positioned at 10° to the molecular beam axis, for dissociation at various photolysis wavelengths, with the electric vector polarised parallel to the molecular beam axis.

could be altered to achieve the same end, giving the fragment atoms impulses of different magnitudes along the guiding axis, leading to an atomic cloud with a tunable velocity. Some short simulations are shown in figure 6.2, where the guide has been positioned at 10° to the molecular beam axis, and the velocity distributions are measured at the exit of the guide, having allowed the atoms to travel through the magnetic region.

Another alternative may be to use some sort of magnetic mirror, possibly made of current carrying wires [18], to reflect the zero-velocity atoms towards the incoming gas pulse which will collide with them. This would be a divergent process, in that once reflected, there would be no more spatial confinement. As a result, such a mirror may only be useful in more analysis of the velocities and densities of the cooled atomic cloud, or pushing the cold atoms into another sample for reaction.

6.1.6 Collision theory

Clearly, since the main sources of loss in the experiment appear to be collisional, it stands to reason that we ought to consider the likely potential energy surfaces for collision to understand how energy transfer is occurring. Since it appears to be the greatest avenue of loss, a theoretical treatment of the collisions of the molecular beam upon the trapped sample would appear necessary. The collisional cross-sections for Ar–Br are known [19, 20], and could be used to investigate the possibility of kinetic energy transfer causing trap losses.

6.2 Outlook

As was described in chapter 1, the area of cold and ultracold chemistry has the possibility to be of great use in a great number of scientific areas. To control chemical reactions with absolute precision would be of fantastic use to a great many disciplines, and the ultracold community has made great strides towards achieving that end. Hopefully, the work in this thesis will make a contribution to the grand scheme. The widening of the scope of atomic species that can be used in cold chemical reactions is the only way in which chemically interesting reactions are going to be studied at low temperatures and controlled accurately. It has been exciting to have been working in an area of science that could develop in a great many directions, and not to know where exactly the field may veer next. In many ways, the most engaging part has been not ever really knowing whether or not any of these experiments were really possible until the data proved otherwise. The fundamental forces of nature are highly mysterious, and hopefully they will forever continue to be explored.

Bibliography

[1] A. Trottier, E. Wrede, and D. Carty, Mol. Phys. **105**, 725 (2010).

[2] S. Jung, E. Tiemann, and C. Lisdat, Phys. Rev. A **74**, 040701 (2006).

[3] B. Clarson, S. R. Procter, A. L. Goodgame, and T. P. Softley, Mol. Phys. **106**, 1317 (2008).

[4] M. Beckert, E. R. Wouters, M. N. R. Ashfold, and E. Wrede, J. Chem. Phys. **119**, 9576 (2003).

[5] P. C. Samartzis, B. L. G. Bakker, T. P. Rakitzis, D. H. Parker, and T. N. Kitsopoulos, J. Chem. Phys. **110**, 5201 (1999).

[6] Y. Matsumi, K. Tonokura, and M. Kawasaki, J. Chem. Phys. **97**, 1065 (1992).

[7] V. A. Alekseev and D. W. Setser, J. Chem. Phys. **107**, 4771 (1997).

[8] I. S. McDermid, J. Chem. Soc., Faraday Trans. 2 **77**, 519 (1981).

[9] H. U. Hostettler and R. B. Bernstein, Rev. Sci. Instru. **31**, 872 (1960).

[10] C. Szewc, J. D. Collier, and H. Ulbricht, Rev. Sci. Instr. **81**, 106107 (2010).

[11] B. C. Sawyer, B. K. Stuhl, D. Wang, M. Yeo, and J. Ye, Phys. Rev. Lett. **101**, 203203 (2008).

[12] B. Friedrich and D. Herschbach, Phys. Rev. Lett. **74**, 4623 (1995).

[13] H. Stapelfeldt and T. Seideman, Rev. Mod. Phys. **75**, 543 (2003).

[14] F. Rosca-Pruna, E. Springate, H. L. Offerhaus, M. Krishnamurthy, N. Farid, C. Nicole, and M. J. J. Vrakking, J. Phys. B **34**, 4919 (2001).

[15] K. Halbach, Nucl. Instr. Methods **169**, 1 (1980).

[16] J. P. Beardmore, A. J. Palmer, K. C. Kuiper, and R. T. Sang, Rev. Sci. Instr. **80**, 073105 (2009).

[17] J. A. Richmond, B. P. Cantwell, S. N. Chormaic, D. C. Lau, A. M. Akulshin, and G. I. Opat, Phys. Rev. A **65**, 033422 (2002).

[18] D. Lau, A. Sidorov, G. Opat, R. McLean, W. Rowlands, and P. Hannaford, Eur. Phys. J. D **5**, 193 (1999).

[19] A. A. Buchachenko, T. A. Grinev, T. G. Wright, and L. A. Viehland, J. Chem. Phys. **128**, 064317 (2008).

[20] P. Casavecchia, G. He, R. K. Sparks, and Y. T. Lee, J. Chem. Phys. **75**, 710 (1981).

Appendix A

Matlab code for Photostop simulations

```
function loadPhotostoppedAtoms(n,runmax,vmiss)

% loads a sample of pre-made photostopped atoms for decay curve
   simulation

if nargin == 0;
    n = 2e6;
    runmax = 1;
    vmiss = 0;
elseif nargin == 1;
    runmax = 1;
    vmiss = 0;
elseif nargin == 2;
    vmiss = 0;% mismatch in beam and recoil velocities
end

% mol beam velocity
v0 = 550; % ms-1
% recoil velocity

amu = 1.66053886e-27;
mBr = 80.*amu;
D0 = 15890;
EBrstar = 3685.24;
Jtocm = 1.9864e-23;
lam = 462e-9;
%lam = 10^7./(D0 + EBrstar + (mBr.*amu.*v0.^2)./Jtocm);
vRecoil = sqrt(((0.01./lam) - D0)*Jtocm/mBr);
vR = sqrt(((0.01./lam) - D0 - EBrstar)*Jtocm/mBr);
%vRecoil = v0 - vmiss; % ms-1

% standard deviations of laser volume
```

```
sdevx = 2*1e-3/2.35; % m
sdevz = 0.2*1e-3/2.35; % m
posn = (randn(n,3)); % m

% randomised position in laser focus

posn(:,1) = posn(:,1).*sdevx;
posn(:,2) = posn(:,2).*sdevz;
posn(:,3) = posn(:,3).*sdevz;

% see program sample_recoil_velocities

[vRecoil] = sample_recoil_velocities(vRecoil,n,vR,0.2); % m

% ie sigmaz = 17.86 = FWHM/2.35
% sigx = 3.4
% from MB pulse

dvr = 3.4;
dvz = 18;

%dvr = 10;
%dvz = 15;

dv = [dvr dvr dvz];
dv = repmat(dv,max(n),1); % ms-1

% randomised inital velocities

vSamp = dv.*randn(n,3); % ms-1
vSamp(:,3) = vSamp(:,3) + v0; % ms-1

% post dissociation velocity

vel = vSamp + vRecoil; % ms-1

if runmax == 1;
    fOutv = sprintf('binaryVel.dat');
    binv = fopen(fOutv,'w');
    fwrite(binv,vel,'float32');
    fclose(binv);

    fOutp = sprintf('binaryPos.dat');
    binp = fopen(fOutp,'w');
    fwrite(binp,posn,'float32');
    fclose(binp);
else
    fOutv = sprintf('binaryVel.dat');
    binv = fopen(fOutv,'a');
    fwrite(binv,vel,'float32');
    fclose(binv);

    fOutp = sprintf('binaryPos.dat');
    binp = fopen(fOutp,'a');
    fwrite(binp,posn,'float32');
    fclose(binp);
```

```
end

%---------------------------------------

function v = samp_recoil_velocities(vRecoil,beta,n)
% Get recoil vectors
%v = vRecoil.*(2*rand(n,3)-1);

if nargin == 0
    beta = 2;
    vRecoil = 380;
    n =1000;
end

% q = branching ratio

q = 1;
beta2 = -1;

% cpdf - cumulative prob distn,
% for calculating accurate theta distn in 3d

z = 2*rand(q*n,1) - 1;
zz = -1:.01:1;
cpdf = (1-beta/2).*zz + beta/2*zz.^3;
zSamp = interp1(cpdf,zz,z);

phi = 2*pi*rand(q*n,1);
r = sqrt(1 - zSamp.^2);
x = r.*cos(phi);
y = r.*sin(phi);

v = vRecoil*[x y zSamp];

z = 2*rand((1-q)*n,1) - 1;
zz = -1:.01:1;
cpdf = (1-beta2/2).*zz + beta2/2*zz.^3;
zSamp = interp1(cpdf,zz,z);

phi = 2*pi*rand((1-q)*n,1);
r = sqrt(1 - zSamp.^2);
x = r.*cos(phi);
y = r.*sin(phi);

v2 = 800*[x y zSamp];

v = [v;v2];
```